

ABSTRACT

Title of Document: SURFACE STUDIES OF GRAPHENE AND
GRAPHENE SUBSTRATES

Kristen Marie Burson, Doctor of Philosophy,
2013

Directed By: Professor Michael S. Fuhrer, Department of
Physics, Center for Nanophysics and Advanced
Materials (Director) and the Materials Research
Science and Engineering Center.

Graphene has attracted a great deal of attention for its exceptional electronic and mechanical properties. As graphene, a two-dimensional lattice of carbon atoms, is an ‘all surface’ material, its interactions with the underlying substrate play a crucial role in determining graphene device behavior. In order to tailor graphene device properties, the interaction between graphene and the underlying substrate must be clearly understood. This thesis addresses the question of the relationship between graphene and graphene substrates by considering both the substrate topography and the impact of charged impurities in the substrate. Utilizing scanning tunneling microscopy and high-resolution atomic force microscopy, we measure the topography of silicon dioxide (SiO_2) supported graphene and the underlying $\text{SiO}_2(300\text{nm})/\text{Si}$ substrates. We conclude that the graphene adheres conformally to the substrate with

99% fidelity and resolve finer substrate features by atomic force microscopy than previously reported. To quantify the density of charged impurities, simultaneous atomic force microscopy (AFM) and Kelvin probe microscopy are used to measure the potential and topographic landscape of graphene substrates, SiO₂ and hexagonal boron nitride (h-BN). We find that the surface potential of SiO₂ is well described by a random two-dimensional surface charge distribution with charge densities of $\sim 10^{11}$ cm⁻², while BN exhibits charge fluctuations that are an order of magnitude lower than this. Charged impurities in the substrate present a scattering source for transport through graphene transistors, and the difference in magnitude in measured substrate charged impurities densities for SiO₂ and BN is consistent with the observed improvement in charged carrier mobility in graphene devices on h-BN over graphene devices on SiO₂. Finally, this thesis presents a theoretical model elucidating the challenges of imaging corrugated substrates by non-contact AFM and an experimental work using Kelvin probe microscopy to characterize the electrostatic potential steps at interfaces of small-molecule organic heterojunctions.

SURFACE STUDIES OF GRAPHENE AND GRAPHENE SUBSTRATES

By

Kristen Marie Burson

Dissertation submitted to the Faculty of the Graduate School of the
University of Maryland, College Park, in partial fulfillment
of the requirements for the degree of
Doctor of Philosophy
2013

Advisory Committee:
Professor Michael S. Fuhrer, Chair
Dr. William G. Cullen
Dr. John Cumings
Dr. Theodore L. Einstein
Dr. Ellen D. Williams

© Copyright by
Kristen Marie Burson
2013

Acknowledgements

First and foremost, I would like to thank my advisors Michael Fuhrer, Bill Cullen, and Ellen Williams. I have had the pleasure of working with Michael twice, first as an REU student and now as a graduate student. My experience as an REU student in his group is undoubtedly an important part of the reason why I am now completing my graduate degree at Maryland. Michael has helped me to become a better speaker and writer, and to dig deeper into scientific understanding. He is always a fount of ideas, whether forging a new experimental direction or navigating barriers in ongoing projects, and this has been critical to my own ability to make scientific progress.

I would like to express my deep gratitude to Bill Cullen, who has not only been a great help in the day-to-day technical aspects of laboratory work, but has also been an incredible advocate for my growth as a scientist and has provided as much advice as either of my “official” advisors. He seems to have an encyclopedic knowledge of how to troubleshoot every experimental difficulty. He has been incredibly patient in training and re-training me how to operate the JEOL and in answering my numerous science-related and otherwise random questions (which seem to be the steady state solution). Bill sets an example with his consistently strong work ethic, attention to detail, and willingness to help, and in doing so he has encouraged me to be a more careful and rigorous scientist and to “think critically”.

Thanks goes to Ellen Williams for hiring me as a graduate student, securing funding for my graduate work, and placing interesting projects in my path. When working on the initial project on graphene corrugation, her excitement was contagious.

Additionally, I have benefitted from her recipe for Christmas cookies (delicious!).

My breadth of knowledge of surface physics is largely the result of many interactions with Ted Einstein and Janice Reutt-Robey through journal club and the surface physics group seminar. My ability to communicate with the broader surface physics community is a direct result of many things I learned in passing, simply by interacting with them. Additionally, Janice always has tips and encouragement to better represent my scientific progress. I thank John Cumings for agreeing to serve on my committee and Santiago Solares, whose humor I have enjoyed through my involvement with the NC-AFM conference.

I have enjoyed working on research projects with Michelle Groce, Mahito Yamamoto, and Jacob Tosado in the surface physics group. Michelle has been a great friend and a source of levity and motivation. Mahito inspires me with his diligence, and I have benefitted from many discussions with him about experimental techniques and direction. Jake always challenges me to really think about my experiments. I have also enjoyed working with Yinying Wei, Jack Hellerstadt, Xinghan (Harold) Cai, and Jinglei Ping and other students and postdocs from Michael's, Janice's, and Ted's groups.

Many moons ago, after spending a summer in Michael's lab as an REU student, I left the summer feeling extremely grateful for the strong mentors that I met in Michael's group. As I leave graduate school, I continue to appreciate the myriad ways that these friends and mentors have helped (and continue to help) me develop as a scientist: Dan Lenski, Alex Curtin, Dave Tobias, Enrique Cobas, Adrian Southard, Andrew Tunnel, Brad Conrad, Shudong Xiao, Jianhao Chen, Chuan Jang, and Masa Ishigami. They taught me about everything from giving a good talk and fabricating graphene devices, to the job application process, CVD growth techniques, and DIY bike repair (mostly from Alex and Dan).

I would like to thank the MRSEC office for helping me to navigate many purchasing forms and conference forms and for giving me the opportunity to be involved in exciting educational outreach. MRSEC education outreach has brought me a lot of joy and is invariably carefully planned and well organized, due in large part to the exceptional work of Donna Hammer and Julie Callis. Jane Hessing, Linda O'Hara, and Sonali Shukla also deserve a note of thanks.

Finally, I thank my family and friends who have borne the brunt of the many frustrations that inevitably arise in the course of completing a PhD. Game nights, conversations, and meals with Brock Russell, Mark Herrera, Caitlin Williams, Cecilia Rorai, Sasha Kueveva, Heather Bradshaw, and Dan Campbell have made graduate school enjoyable. I am especially thankful for Caitlin Williams, who has been a great friend and a great roommate. Karl Schmitt has been a great support as have Will and

Elise Bruner and Mike and Becky Lloyd. My parents and my family have been a great encouragement to me and my father's persistent question "Did you write your thesis yet?" has kept me moving forward.

Table of Contents

Acknowledgements.....	ii
Table of Contents.....	vi
List of Figures.....	viii
Chapter 1: Introduction to Graphene.....	1
1.1 Crystal Structure of Graphene and Graphite.....	1
1.2 Graphene Band Structure.....	2
1.3 Electronic Transport in graphene.....	5
1.4 Charged Impurity scattering in graphene.....	10
1.5 Topographic Considerations for Graphene.....	13
1.6 Resonant Scatterers.....	18
1.7 Conclusion.....	19
Chapter 2: Sample Preparation Techniques.....	21
2.1 Graphene Device Fabrication.....	21
2.2 Small Molecule Organic Deposition.....	24
Chapter 3: Scanned Probe.....	27
3.1 Scanning Tunneling Microscopy.....	27
3.2 Atomic Force Microscopy.....	28
3.3 Kelvin Probe Force Microscopy.....	32
3.4 JEOL UHV AFM/STM/SEM.....	33
Chapter 4: Corrugated Surface Resolution Model.....	36
4.1 Introduction.....	36
4.2 Experimental Motivation.....	38
4.3 Model of the corrugated-surface resolution.....	39
4.3.1 Atom-surface potential.....	41
4.3.2 Tip-surface potential.....	42
4.3.3 Calculation of frequency shifts.....	48
4.4 Corrugated Surface AFM Resolution Model Results and Discussion.....	48
4.4.1 Deviation from the Sphere-Plane Hamaker Force Law.....	49
4.4.2 Attenuation of Surface Features.....	50
4.5 Conclusions.....	54
Chapter 5: Graphene Corrugation.....	55
5.1 Introduction.....	55
5.2 High Fidelity Imaging of Graphene and the SiO ₂ Substrate.....	56
5.3 Energetics of graphene interaction with the substrate.....	68

5.3.1 Simple Analysis of the Energetics of Conformal Adhesion	69
5.3.2 Membrane Physics and Parameterization of the Adhesion Energy	70
5.3.3 Energetics from membrane physics model	74
5.3.4 Energetics from Other Recent Theories.....	78
5.3.5 Summary and Conclusion	79
5.4 Potential from corrugation	80
5.7 Conclusions and Summary	82
Chapter 6: Charged Impurities in Graphene Substrates.....	84
6.1 Introduction to Scanning Probe Experiments on Graphene.....	85
6.2 Kelvin Probe of Graphene Substrates	92
6.3 Conclusions.....	107
Chapter 7: Potential Steps at C ₆₀ -TiOPc-Ag(111) Interfaces: UHV - Noncontact	
Scanning Probe Metrology	109
7.1 Introduction.....	110
7.2 Sample Preparation	113
7.3 Ag(111) Step Characterization	116
7.4 C ₆₀ -Ag(111) Interface	119
7.5 C ₆₀ -TiOPc-Ag(111).....	121
7.6 Summary and Conclusion	127
Chapter 8: Summary and Conclusions.....	129
8.1 Summary	129
8.2 Future Outlook.....	130
Bibliography	133

List of Figures

Figure 1: Graphene (left) and graphite (right) crystal structure.....	2
Figure 2: Graphene band structure (Schonenberger [3])	4
Figure 3: Gate voltage dependent conductivity for a graphene device at 10K (from Reference [8])	7
Figure 4: Graphene magnetoresistance ρ_{xx} and ρ_{yy} for $B = 1T$, from Ref. [23], with an inset of conductivity as a function of carrier concentration. Blue circles are experimental data from Ref. [24] while dashed and solid lines represent theoretical fits. The plots highlight the symmetry of electron and hole carriers and the non-zero minimum conductivity in the limit of vanishing charge carrier concentration.....	8
Figure 5: Transport measurements for distinct graphene devices fabricated on SiO_2 substrates. The mobility varies significantly from device to device, ranging in value from $(1-20) \times 10^3 cm^2/V \cdot s$ for distinct samples within the set studied (figure from Reference [15]).	8
Figure 6: Charged impurity scattering in graphene leads to lower mobility.	12
Figure 7: TEM image of free standing graphene. The free standing graphene exhibits ripples (image from Reference [55]).....	16
Figure 8: (a) STM image of the surface corrugation for graphene on SiO_2 (b) ambient AFM image of the SiO_2 substrate. (from Reference [58]).....	17
Figure 9: (a) AFM of graphene on mica. (b) AFM topography for cleaved Kish graphite. (c) Height histograms for graphene on mica (blue) and cleaved graphite (red). (images from Reference [59])	17
Figure 10: Optical micrograph of large monolayer flake of graphene	23
Figure 11: Raman Spectroscopy from a graphene sample over (a) monolayer and (b) bilayer graphene flake shown in optical micrograph (top). The 2D peak can be fit by a single Lorentzian for the monolayer graphene, while for the bilayer a two peak fitting is required (evidenced here by the asymmetry). The ratio of the 2D to G peak intensity also distinguishes monolayer from thicker layers.....	24
Figure 12: Schematic of graphene device structure	24
Figure 13: Schematic of STM (from Ref [80]).....	28
Figure 14: Schematic diagram of atomic force microscopy (AFM). A quadrant photodiode is used to detect the motion of the cantilever. (image from [94]).....	31
Figure 15: Schematic diagram of atomic force microscope with Kelvin probe	31
Figure 16: JEOL UHV STM/AFM with SEM used for the experiments in this thesis.	34
Figure 17: SEM image of the an AFM tip above a graphene sample. The metal contacts appear light grey/white and form a grid pattern while the graphene in this image is a darker gray color.....	34
Figure 18: AFM Resolution Examples: (a) high resolution UHV NC-AFM image of SiO_2 displaying features with radius of curvature ~ 2.3 nm (R_{tip} nominally 2 nm, $\Delta f = -20$ Hz, $A = 5.0$ nm, image size = 200 nm x 200 nm) (b) under-resolved UHV NC-AFM image of SiO_2 with the same height scale as (a) (R_{tip} nominally 30 nm, $\Delta f = -150$ Hz, $A = 1.0$ nm, image size 200 nm x 200 nm) (c) UHV NC-AFM image of Si(111) with inset showing atomic resolution (R_{tip} nominally 10 nm, $\Delta f = -40$ Hz, $A = 7.1$ nm, image size 50 nm x 50 nm).....	39

Figure 19: Verification of atom-substrate potential: Potential w_{a-s} vs. z for numerical and analytical schemes for a “point atom” interacting with a flat surface. The near-perfect overlap of the curves demonstrates the fidelity of the numerical integration scheme..... 43

Figure 20: Schematic illustrating the model geometry: The surface is sinusoidally corrugated along the x direction only, with wavelength λ and amplitude δ_s . The surface corrugation is independent of y (quasi 1-D geometry). The tip is modeled as a sphere of radius R 45

Figure 21: Hamaker Force for Flat Surfaces: Relationship between tip potential and distance from the surface. Here the distance is taken relative to the surface position (distance from surface = $z(x) - z_s(x)$). The dashed line is a reference for $1/z$ dependence expected from the Hamaker force law for the interaction between a flat surface and a sphere. The numerical results show excellent agreement with the exact potential (eqn (17)) 45

Figure 22: Hamaker Force Law for Corrugated Surfaces: Tip-sample distance dependence of tip potential for high symmetry points (inset, $x = 0$, $x = \lambda/4$, $x = \lambda/2$, and $x = 3\lambda/4$) for the two radii ($R = 5$ nm and $R = 10$ nm). Lines for the exact analytical form (eqn (17)) of the Hamaker relationship between a sphere and a plane are shown (black line) for comparison..... 53

Figure 23: Contours of constant normalized frequency shift, γ , for corrugated surface with a tip of $R = 5$ nm. Attenuation is observed as distance from the surface increases. Here, z_{abs} gives an absolute position in the z -direction, not a relative distance from the surface. 53

Figure 24: (a) SiO_2 -supported graphene topography obtained with STM (195x178 nm, -305 mV, 41 pA) and (b) bare SiO_2 topography obtained with high-resolution NC-AFM (195x178 nm, $A = 5$ nm, $\Delta f = -20$ Hz)..... 58

Figure 25: Fourier amplitude spectra of: SiO_2 NC-AFM (red squares), monolayer graphene/ SiO_2 STM (blue triangles), and under-resolved SiO_2 (black dots). Spectra 1 and 2 were obtained from an averaged data set to establish statistical uncertainty. Wave number is defined as wavelength⁻¹. 59

Figure 26: Extended comparison between SiO_2 and graphene. All spectra are 1-dimensional Fourier amplitude spectra. Panel (a) shows a globally averaged data set consisting of averaged measurements of two graphene/ SiO_2 samples and two SiO_2 substrates, and these two curves are reproduced in panels (b-d) for specific comparisons. Open red squares indicate SiO_2 NC-AFM measurements and open blue triangles represent monolayer graphene STM measurements. Panel (b) shows Fourier spectra from the two images presented in Figure 24 overlaid with the globally averaged data set to show that they are representative. Panel (c) shows the result of annealing SiO_2 sample 1 at 500 C, also overlaid with the globally averaged data set. Panel (d) shows the Fourier spectra for NC-AFM images of monolayer graphene/ SiO_2 for comparison. Green symbols show an average over 8 images (all slightly under-resolved in comparison to STM) which are representative of Figure 27(c). Black dots are from one partial image (shown in Figure 27(b)) which is as highly resolved as our STM data. All quantities here are analyzed from raw data, with no

filtering (only background subtraction). Wavenumber units are defined as wavelength ⁻¹	61
Figure 27: Topographic comparison of monolayer graphene/ SiO ₂ measured with STM and NC-AFM. All three regions are 60 nm x 60 nm. (a) Graphene monolayer on SiO ₂ measured by STM (-1.0 V, 47 pA). (b) Our highest-resolution measurement of graphene/SiO ₂ by NC-AFM ($\Delta f = -10$ Hz, $A = 10$ nm). (b) has two horizontal bands which are dominated by feedback oscillations; these are marked by green lines. (c) Typical resolution obtained for graphene/SiO ₂ by NC-AFM ($\Delta f = -10$ Hz, $A = 3$ nm). (a) is a complete 60 nm image sampled at 512 x 512 pixels; (b) and (c) are cropped from larger images at coarser sampling.	64
Figure 28: UHV STM image of SiO ₂ -supported mono-layer graphene. The honeycomb lattice is resolved, in addition to significant nanometer-scale roughness.	64
Figure 29: Schematic diagram of force-distance relationship for atomic force microscopy. Here the distance is the tip-sample distance. (diagram from Reference [119])	67
Figure 30: Images of SiO ₂ at varying levels of spatial resolution. All images are 200 nm x 200 nm in size (a) ambient tapping-mode AFM image of SiO ₂ , obtained in am mode with conventional Si cantilever. (b) UHV FM-AFM image of SiO ₂ , obtained with metal-coated cantilever ($\Delta f = -150$ Hz, $A = 1.0$ nm). (c) UHV FM-AFM image of SiO ₂ , obtained with super-sharp silicon cantilever ($\Delta f = -150$ Hz, $A = 1.0$ nm). (d) line profile from image (c) with radius of curvature fit indicating curvature radius ~2.3 nm.	68
Figure 31: Schematic diagram of the geometry for membrane adhesion. $z_s(\mathbf{r})$ is the function for the substrate geometry (black solid line) while h_0 represents the distance between the substrate and graphene (black dashed line) which minimizes the adhesion potential. The vector \mathbf{r} is in the x-y reference plane.....	70
Figure 32: Quadratic fits to adhesion energy curve from Ref. [123], in the vicinity of the potential minimum. The blue curve is fit to the repulsive side while the green curve is fit to the attractive side.	73
Figure 33: Curvature histograms, normalized to unit area, for graphene (narrower distribution) and SiO ₂ (broader distribution)	80
Figure 34: STM of graphene topography (left) and the calculated potential resulting from this topography (right) based on equation (33). Note that the large z range is indicative of noi	81
Figure 35: Potential autocorrelation function from calculated potentials from equation (33) due to graphene corrugation (green). Images used were 60nm x 60nm. Potential autocorrelation functions from 1 μ m x 1 μ m Kelvin probe images of BN and SiO ₂ are shown for comparison (orange and blue, respectively).....	82
Figure 36: (a) Color map of surface density fluctuations in a monolayer graphene sheet on SiO ₂ extracted from potential measurements with a scanning single electron transistor. Blue regions correspond to hole-rich regions while red regions correspond to electron-rich regions. (b) Potential fluctuations above the bare SiO ₂ substrate. (from reference [44]).....	86

Figure 37: (a) Inverse compressibility as a function of the density and magnetic field. (b) A line scan from plot a at 11 T (blue) and fit to data with Gaussians of equal variance. (from [44]).....	87
Figure 38: (a) 60x60nm STM image of graphene corrugation on SiO ₂ and (b) dI/dV map obtained simultaneously displaying electron-hole puddles within the graphene sheet with characteristic length ~20nm (from Reference [40])	91
Figure 39: Topography and dI/dV mapping for graphene on SiO ₂ and graphene on BN (adapted from References [41] and [42])	91
Figure 40: (a) Topography and (b) relative potential for the bare SiO ₂ /Si substrate. (c) Model of the expected charge distribution. (d) Potential for a simulated charge distribution (parameters are charge density $n_{\text{imp}} = 2.5 \times 10^{11} \text{ cm}^{-2}$, distance of tip to charges $d = 1 \text{ nm}$, oxide thickness $d_{\text{ox}} = 300 \text{ nm}$). Color scale in (d) is same as (b) with full range of 630mV.....	94
Figure 41: Autocorrelation function from experiment (blue squares, average from 3 images) and best theoretical fit ($n_{\text{imp}} = 2.7 \times 10^{11} \text{ cm}^{-2}$, $d = 1 \text{ nm}$, $d_{\text{ox}} = 300\text{nm}$). For the fit function, the autocorrelation function was convolved with a Gaussian of FWHM = 30nm to account for broadening due to the size of the tip.	97
Figure 42: Autocorrelation function from experimental data presented in Ref. [44] (blue squares) and best theoretical fit ($n_{\text{imp}} = 0.7 \times 10^{11} \text{ cm}^{-2}$, $d = 47 \text{ nm}$, $d_{\text{ox}} = 300\text{nm}$). For the fit function, the autocorrelation function was convolved with a Gaussian of FWHM = 100nm to account for broadening due to the size of the tip.	99
Figure 43: (a) Topographic and (b) potential images from a 40 nm h-BN flake exfoliated onto SiO ₂ . The same scales as used in Figure 40 is used for comparison (full range 630 mV) (c) The magnitude of the autocorrelation function for BN (orange triangles, average from 9 images) is reduced from that for the underlying SiO ₂ (blue squares, same as Figure 41).	100
Figure 44: Cartoon for “cleanest case” scenario for charged inhomogeneity of h-BN. Here BN is treated as a simple dielectric (no active screening).	103
Figure 45: The “cleanest case” scenario model potential autocorrelation function for h-BN (red, 40 nm ‘Fit) is shown along with the experimental data and fit for h-BN and SiO ₂ . Here the “cleanest case” scenario model ACF is developed using $d=40\text{nm}$ (h-BN thickness) and the parameters extracted from fitting the SiO ₂	103
Figure 46: Experimental potential autocorrelation function for 40 nm lifted scan over SiO ₂ (blue, 40 nm lift) shown in comparison to experimental data for substrates h-BN (orange) and SiO ₂ (blue) and theoretical models (red line)	104
Figure 47: Effect of fabrication procedures (electron beam exposure and annealing) on graphene substrate charged impurity density. The surface charge densities before electron beam exposure, as a function of time after the 30s electron beam exposure, and after annealing at 250 °C are shown for SiO ₂ (blue squares) and h-BN (orange triangle) substrates.	104
Figure 48: Interface between honeycomb phase TiOPc and close-packed C ₆₀ viewed by STM ($V = 1.594 \text{ V}$, $I = 27.5 \text{ pA}$).	109
Figure 49: Local measurement of Ag(111) monatomic step-edge dipole: (a) AFM topographic image of surface topography ($A=1\text{nm}$, $\Delta f=-490\text{Hz}$) with two crystallographic steps (b) corresponding Kelvin Probe image (c) schematic of Ag(111) step-edge dipole due to Smoluchowski smoothing (d) surface potential	

measured perpendicular to steps (120 line average) (blue) . See Supplemental Information for related classical simulation. 115

Figure 50: Electrostatic simulation of potential profiles for select interface dipoles: (a) Schematic illustration of the crystallographic step-edge dipole, shown in cross section; (b) Simulated potential profile from a $1.38 \times 10^{-3} \text{ e nm}$ step-edge dipole at a height 1.3nm above the surface. The 10 mV potentiometric decrease above the step reproduces the KPFM observation on Ag(111). (c) Schematic illustration of the interface dipole at the C_{60} - TiOPc domain boundary and corresponding image charge, shown in cross section (d) Potential profile from the molecular interface dipole arrangement of (c). The asymmetric profile is characteristic of this lateral dipole arrangement. A dipole value of 0.012 e nm per molecule was used to generate the 5 mV potential feature at a 1.6 nm height above the surface. The absence of this feature in the KPFM measurement sets an upper bound on the C_{60} – TiOPc interface dipole..... 118

Figure 51: Local measurement of surface potential for submonolayer 0.4 ML C_{60} film on Ag(111): (a) AFM topographic image ($A = 1.85\text{nm}$, $\Delta f = -856\text{Hz}$) with molecularly resolved C_{60} islands (b) Kelvin probe image of region (a); (c) Model of C_{60} arrangement for outlined region in (a) (d) histogram of surface potential values from (b) and referenced to the known Ag(111) work function 120

Figure 52: Local measurement of potential across C_{60} –TiOPc monolayer domain boundary: (a) NC-AFM topography ($A = 2\text{nm}$, $\Delta f = -700\text{Hz}$) shows molecular contours of TiOPc domain (left, honeycomb structure) and C_{60} domain (right,hexagonal structure). An outlined section of the TiOPc domain is raised to better view the periodicity. (b) Kelvin probe image of region (a); Model of TiOPc honeycomb arrangement (from Ref. 10) corresponding to the region in (a) For visual clarity, the pore-occupying TiOPc molecule is removed. (d) Line profiles of surface topography and surface potential measured perpendicular to grain boundary. Domain boundary widths are 1.5nm in topography and 3.6 nm in potential (FWHM). 121

Figure 53: STM images showing several distinct phases of TiOPc on Ag(111): (a) Coexisting honeycomb and flower phase ($V_b = 1.594 \text{ V}$, $I = 27.5 \text{ pA}$), (b) two terraces of honeycomb phase TiOPc ($V_b = 1.526 \text{ V}$, $I = 27.5 \text{ pA}$), and (c) flower phase ($V_b = 1.205$, $I = 26.6 \text{ pA}$)..... 123

Chapter 1: Introduction to Graphene

From scholars old, new

There's vibrant work to review

A tale of graphene

Graphene, a hexagonal array of carbon atoms, is a novel two-dimensional material that has attracted a great deal of interest for its exceptional electronic and mechanical properties. Additionally, graphene is a physical system allowing for the exploration of two-dimensional physics. This chapter provides an introduction to this phenomenal material introducing both physical and electronic structure as well as transport within graphene transistors. Special attention is given to literature pertaining to charged impurity scattering in graphene and to substrate-supported graphene corrugation.

1.1 Crystal Structure of Graphene and Graphite

Graphene is a derivative of and constituent of graphite. The graphite crystal structure consists of many planes of carbon which exhibit strong bonding within the plane (sp^2 bonds as in a benzene ring from the $2s$, $2p_x$, and $2p_y$ orbitals), but weak van der Waals bonds between the planes. Graphene is a single carbon layer of graphite, one atom thick. The hexagonal lattice is non-Bravais, but can be represented as a triangular Bravais lattice with a two-atom basis, as show in Figure 1. The unit vectors for the lattice are:

$$\vec{a}_1 = a_0\sqrt{3} \left(\frac{1}{2}, \frac{\sqrt{3}}{2} \right)$$

$$\vec{a}_2 = a_0\sqrt{3} \left(-\frac{1}{2}, \frac{\sqrt{3}}{2} \right) \quad (1)$$

Here $a_0 = 0.142$ nm, the carbon-carbon bond length. The two atoms in the basis are typically labeled A and B, leading to two sub-lattices with the same nomenclature convention and also to a degenerate band structure, which will now be discussed.

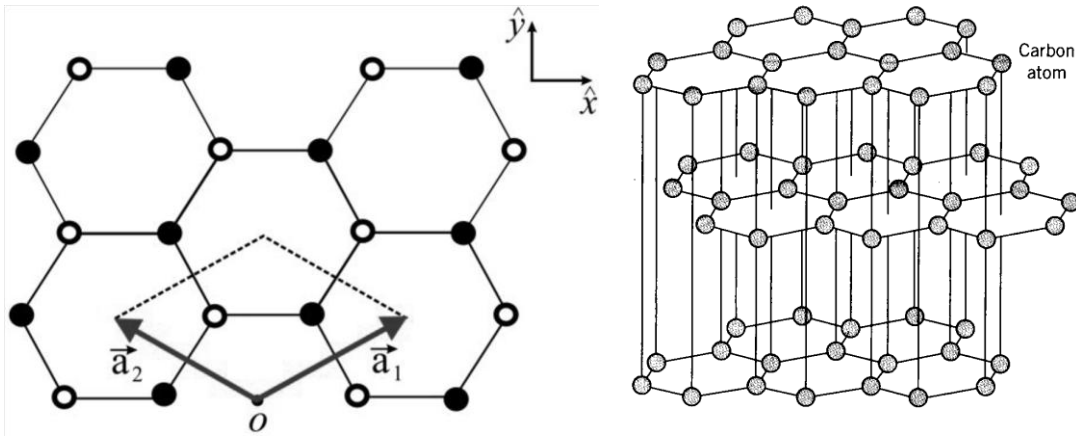


Figure 1: Graphene (left) and graphite (right) crystal structure

1.2 Graphene Band Structure

Graphene is classified as a zero-band gap semi-conductor. It has a unique band structure which is correlated with the novel electronic properties of the material. Although graphene has only been realized experimentally in the last 10 years, theoretical work on the band structure and electronic properties have been pursued since the 1940s [1,2]. The origin of the linear band structure can be understood straightforwardly by employing a tight-binding modeling including nearest neighbor hopping [3].

For the tight binding approach the wavefunction (ψ) is described as a linear combination of the wavefunctions for each sub-lattice (ϕ_1, ϕ_2): $\psi = \phi_1 + \lambda\phi_2$.

Following Wallace [1], the following eigenvalue problem is obtained:

$$\begin{vmatrix} H_{11} - EN & H_{12} \\ H_{21} & H_{22} - EN \end{vmatrix} = 0$$

where N is the number of unit cells in the crystal and $H_{ij} = \int \phi_i^* H \phi_j$. Simplifying the energy expression with symmetry considerations and employing the following change of variables:

$$H'_{11} = H'_{22} = \frac{1}{N} H_{11} = \frac{1}{N} H_{22}$$

$$H'_{12} = \frac{1}{N} H_{12}$$

the energy is obtained

$$E = H'_{11} \pm |H'_{12}|$$

with

$$H'_{11} = E_0 - 2\gamma_{AA}(\cos(2\pi k_y a) + 2 \cos(\pi k_x a \sqrt{3}) \cos(\pi k_y a))$$

$$|H'_{12}|^2 = \gamma_0^2 \left(1 + 4 \cos\left(\frac{3a_0 k_y}{2}\right) \cos\left(\frac{\sqrt{3}a_0 k_x}{2}\right) + 4 \cos^2\left(\frac{\sqrt{3}a_0 k_x}{2}\right) \right)$$

γ_{AA} and γ_0 give the interaction between neighboring sites on the same sub-lattice and the interaction between neighboring sites and the A and B sublattices, respectively.

Neglecting next-nearest neighbor interactions (e.g. only A and B sublattice interactions considered), the energy is given as,

$$E(\mathbf{k}_x, \mathbf{k}_y) = \pm \gamma_0 \sqrt{\left(1 + 4 \cos\left(\frac{3a_0 k_y}{2}\right) \cos\left(\frac{\sqrt{3}a_0 k_x}{2}\right) + 4 \cos^2\left(\frac{\sqrt{3}a_0 k_x}{2}\right) \right)} \quad (2)$$

The band structure (from Equation (2)) is represented graphically in Figure 2. There are several notable features of this dispersion. At low energies, the dispersion is linear (Dirac-like), and there are two Dirac cones per unit cell located at the K and K' points in the Brillouin zone, leading to a valley degeneracy. The conduction band (π) meets the valence band (π^*) at a single point known as the Dirac point, leading to the classification of graphene as either a semi-metal or zero band-gap semiconductor. The electrons and holes exist in symmetric environments.

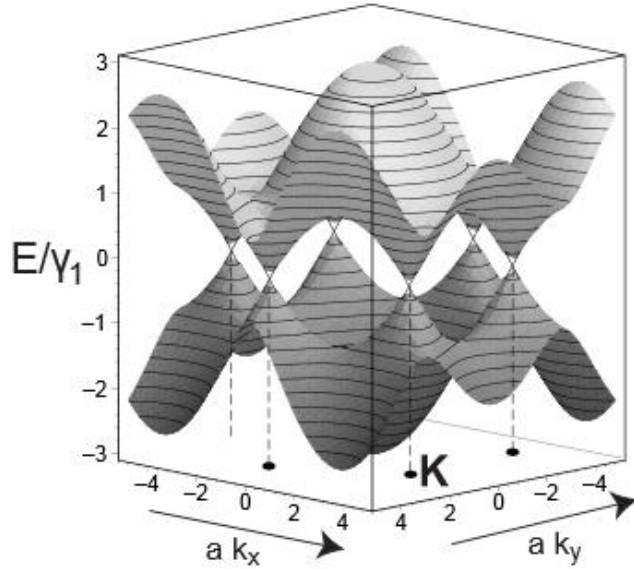


Figure 2: Graphene band structure (Schonenberger [3])

Considering only the low-energy limit, we find:

$$E_{k,\pm} = \pm \hbar v_F |\mathbf{k}|$$

where $v_F = \frac{3\gamma_0 a_0}{2\hbar} \approx 10^6 \frac{m}{s}$, approximately 300 times smaller than the speed of light.

Additionally, back-scattering is prohibited in graphene due to conservation of pseudo spin (see Ref. [3]), meaning that electrons are expected to travel long distances without scattering. The combination of high Fermi velocity, the absence of back-

scattering, and the weak electron-phonon coupling in graphene leads to high electron carrier mobility [4,5]. As such, graphene has captured the scientific imagination both as a new ‘playground’ for two-dimensional physics and as a promising material for new electronic devices and transistor configurations.

1.3 Electronic Transport in graphene

The first studies of graphene field effect transistors were done in the Manchester group by Novoselov et al. [6–8]. In this work, the group used the now standard ‘mechanical exfoliation’ approach (also known as the scotch tape method – see Chapter 2) along with lithographic techniques to fabricate graphene devices. They found that graphene exhibited exceptional conductive properties. Figure 3 shows the conductivity vs. gate voltage relationship from these initial experiments. The conductivity of graphene is carrier density dependent and ambipolar; the conductivity passes through its minimum value as the carrier concentration (tuned by the gate voltage, V_g) transitions between electron carriers and holes. The conductivity exhibits an approximately linear dependence on carrier concentration in the high-density limit. Because the concentration of carriers (n) scales linearly with V_g , the mobility (μ) from the semiclassical Drude model is constant, and proportional to the slope of the conductivity (σ) vs. gate voltage in the linear regime ($\sigma = en\mu$, where e is the elementary charge). In the low-density limit, graphene exhibits a minimum conductivity, which is non-zero despite the limit of vanishing charge carriers and is largely temperature-independent. The relationship of the minimum conductivity to charge inhomogeneity in graphene will be explored further below.

Since these initial studies of graphene transport, numerous investigations have been conducted to understand the mechanisms involved in graphene transport and the limiting factors for graphene mobility [4]. Graphene fabrication techniques have included chemical vapor deposition [9–11] and epitaxial growth [12–14], among others, to produce larger scale flakes reproducibly. While graphene field effect devices made from CVD graphene and epitaxial graphene present the most promising routes towards large-scale production of graphene transistor devices, devices made by mechanical exfoliation have historically exhibited the highest levels of device performance, due in part to the pristine graphene crystals that result from this fabrication technique. In this section, attention will be given primarily to transport studies of mechanically exfoliated graphene.

Following the initial work of Geim and Novoselov, additional measurements of graphene transport on SiO₂ were pursued. Tan et al. reported a set of graphene samples with mobility in the range of $(1-20) \times 10^3 \text{ cm}^2/\text{Vs}$ produced from nominally the same fabrication procedures. The transport measurements (conductivity vs. gate voltage) for representative samples from this study are shown in Figure 5 [15]. While graphene has the highest intrinsic carrier mobility of any known material at room temperature [16], the mobility for graphene on SiO₂ appears limited to $25,000 \text{ cm}^2/\text{Vs}$ [15,17,18]. Suspended graphene, free from interaction with the substrate, exhibits a higher device carrier mobility [19–21]. A low-temperature charge carrier mobility of $1,000,000 \text{ cm}^2/\text{Vs}$ has been reported for suspended graphene cleaned by current annealing [22].

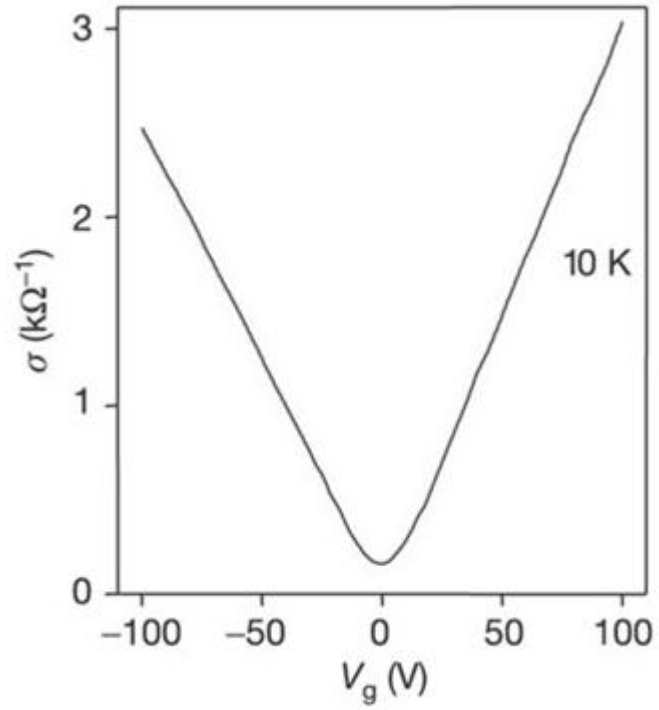


Figure 3: Gate voltage dependent conductivity for a graphene device at 10K (from Reference [8])

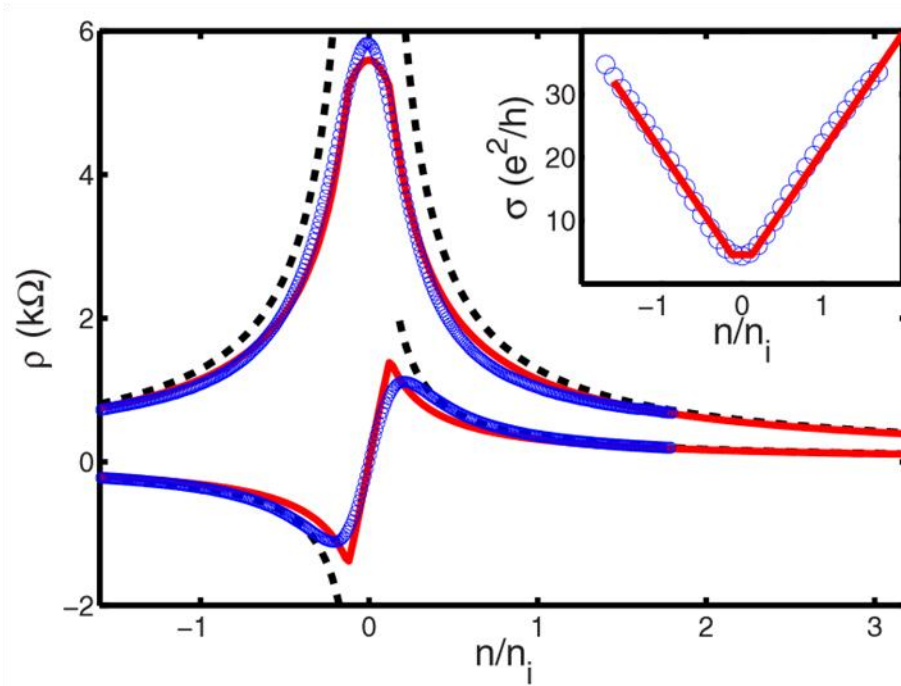


Figure 4: Graphene magnetoresistance ρ_{xx} and ρ_{yy} for $B = 1\text{T}$, from Ref. [23], with an inset of conductivity as a function of carrier concentration. Blue circles are experimental data from Ref. [24] while dashed and solid lines represent theoretical fits. The plots highlight the symmetry of electron and hole carriers and the non-zero minimum conductivity in the limit of vanishing charge carrier concentration.

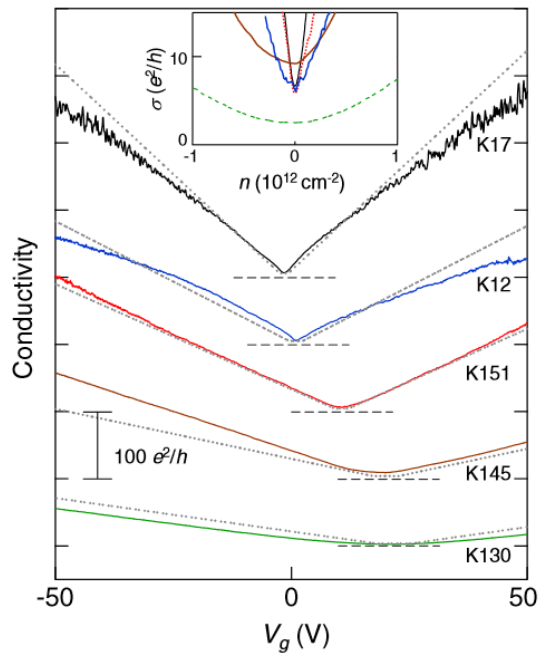


Figure 5: Transport measurements for distinct graphene devices fabricated on SiO_2 substrates. The mobility varies significantly from device to device, ranging in value from $(1-20) \times 10^3 \text{cm}^2/\text{V}\cdot\text{s}$ for distinct samples within the set studied (figure from Reference [15]).

More recently, graphene devices on h-BN have shown significant improvement over graphene devices on SiO₂ for mechanically exfoliated devices. Dean et al. from Columbia University performed the seminal transport measurements on graphene/h-BN devices [25]. In this work, h-BN was mechanically exfoliated using comparable techniques to graphene mechanical exfoliation. Mechanically exfoliated graphene was subsequently transferred to the h-BN using a polymer layer scaffold (PMMA) and a micro-positioning system. Dean et al. found that the devices exhibited nearly an order of magnitude improvement in graphene device mobility over graphene devices on SiO₂ substrates. Additionally, magnetotransport revealed Shubnikov-de Haas oscillations, and the signatures of the zero-energy Landau level quantum Hall state $\nu = \pm 1$ were visible at magnetic fields a factor of two smaller than reported for graphene on SiO₂ [26]. This magnetotransport result offers another metric for the improved device quality on h-BN over SiO₂. Additionally, mobilities of 500,000 cm²/V·s have been reported in graphene encapsulated between h-BN layers [27] and CVD graphene over mechanically exfoliated h-BN showed an order of magnitude improvement over CVD graphene devices on SiO₂ [28], proving h-BN to be a promising substrate for graphene devices.

Other substrates have been considered for graphene FETs, but to date these alternatives have not produced the same level of quality of electronic properties for graphene devices as h-BN nor the corresponding level of excitement and interest from

the scientific community. E.g., graphene on mica and PMMA exhibit, respectively, a mobility of $2,500 \text{ cm}^2/\text{V}\cdot\text{s}$ and $8,000 \text{ cm}^2/\text{V}\cdot\text{s}$ [29].

Understanding the discrepancy in the quality of as-fabricated graphene field effect transistors on different substrates (and even among devices on SiO_2) is a matter of some debate. Questions surrounding the dominant carrier scattering mechanisms in graphene have been (and continue to be) an important narrative in the graphene literature [4,16,29–35]. Three primary mechanisms have been proposed to explain the approximately linear conductivity versus gate voltage relationship from graphene transport measurements: charged impurities, resonant scatterers, and corrugations. These mechanisms may give rise to scattering in graphene, and understanding the environmental factors for graphene devices is critical for improved understanding of the limiting factors for graphene device performance and to new routes for engineering the properties of graphene. This thesis considers two of these factors: corrugation (Chapter 5) and charged impurities (Chapter 6). Each mechanism is introduced in the following sections.

1.4 Charged Impurity scattering in graphene

Charged impurities have been shown to have an important impact on graphene transport. Charged impurities near the graphene sheet can explain the observed linear dependence of conductivity σ on carrier density n [36], and there is consensus [34] that the minimum conductivity at nominally zero carrier density σ_{min} [37,38] is determined by charged impurity disorder. At low carrier density, spatial inhomogeneity of charged impurities near the graphene sheet results in the formation

of electron and hole puddles within the graphene sheet. This allows for conduction channels through the sheet despite nominally zero carrier density (and thus explains the experimental observations of the minimum conductivity) [38,39].

Adam et al. developed a self-consistent analytic theory for graphene transport based on charged impurities using random phase approximation (RPA)-Boltzmann formalism to explain both the linear transport at high-conductivity and width and magnitude of the minimum conductivity [38]. Scattering by charged impurities gives a conductivity linear in carrier density at high carrier density, which saturates to a minimum conductivity at low carrier density:

$$\sigma = \frac{20e^2n}{h n_{imp}} \quad n > n^*$$

$$\sigma_{min} = \frac{20e^2n^*}{h n_{imp}} \quad n < n^*$$

where n is the gate-induced carrier density, n^* is the residual carrier density, e is the elementary charge and h is Planck's constant. The constant of proportionality depends on the dielectric constants of the media surrounding graphene; the factor 20 above is calculated for graphene on SiO₂ with vacuum above. The self-consistent theory additionally predicts that n^* is roughly proportional to, but somewhat smaller than, n_{imp} ; an analytical expression for n^* is given in Ref. [38]. For comparison with experimental data, the rms variation in charge density $n_{rms} = \sqrt{3}n^*$. n^* , the residual carrier density, represents the carrier density at zero gate voltage (related to electron and hole puddles). The general finding is that σ_{min} is a few e^2/h , and depends only weakly on disorder strength and dielectric environment, resulting in a roughly “universal” minimum conductivity.

Chen et al. determined an empirical relationship between charged impurity density and graphene device mobility by exposing devices to potassium ions in ultra-high vacuum [30]. In this experiment, successively greater doses of potassium resulted both in a shift in the doping level (indicated by a shift in the gate voltage at which the minimum conductivity occurs) and in a decrease in the charge carrier mobility, as shown in Figure 6. From this data they derived a relationship between the charged impurity density (n_{imp}) and device mobility (μ): $\mu = 5 \times 10^{15} \text{ V}^{-1}\text{s}^{-1}/n_{\text{imp}}$. Thus the limitations to realized device mobility for substrate-supported graphene MOSFETs may be determined by the density of substrate charged impurities, provided that the mobility limitation due to charged impurities is the maximally limiting scattering source.

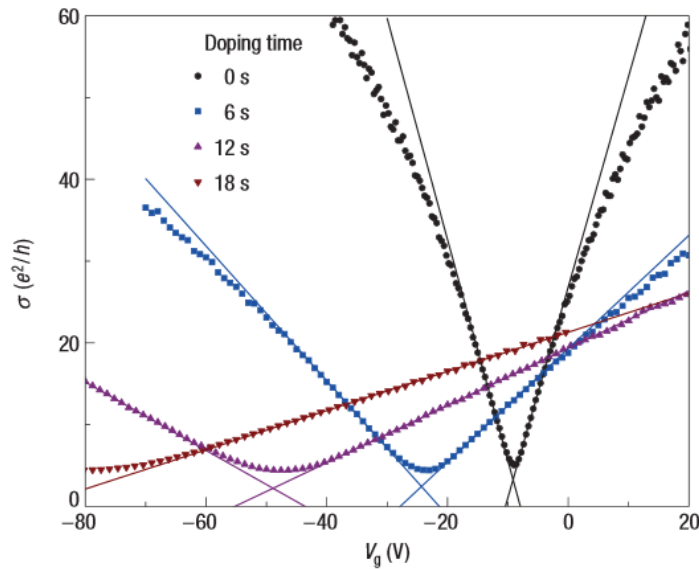


Figure 6: Charged impurity scattering in graphene leads to lower mobility.

In addition to transport measurements the magnitude of carrier density inhomogeneity in graphene has been observed directly by several groups utilizing scanning probe techniques [40–44]. The scanned probe experiments map the electron-hole puddle landscape in graphene, a more thorough discussion of which will be presented in Chapter 6. Charged impurities are credited for producing the observed puddles in graphene sheets on SiO₂ and h-BN substrates, but they are not the only important factor in understanding graphene electronic properties; theoretical and experimental studies have found that graphene corrugation can play an important role.

1.5 Topographic Considerations for Graphene

Corrugation has been predicted to have a significant impact on the electronic properties of graphene. Local curvature effects giving rise to rehybridization of the π - σ orbitals in graphene can lead to electrochemical-potential variation and theoretical work indicates that corrugations of a graphene sheet can create a long-range scattering potential leading to increased resistivity [45–47]. Strain can lead to artificial magnetic fields, with the possibility of a quantum Hall state in a zero external field [48–50]. Indeed, pseudo-magnetic fields in excess of 300 Tesla have been inferred from STM measurements of Landau levels in strained graphene nanobubbles [51].

Engineered strained structures offer an intriguing route towards controlled pseudo-magnetic fields and to band gap engineering in graphene [52]. However, in order for

strain engineering to be experimentally realized, it is necessary to develop a thorough understanding of the determining factors for graphene corrugation. Towards this end, a number of studies characterizing corrugation of graphene have been conducted both for substrate-supported and free-standing graphene [47,53–59].

Studies of free-standing graphene indicate that graphene does not lie flat in 2D, but rather exhibits undulations in 3D [55,56]. One study of free-standing graphene utilized SEM to investigate the development of ripples in graphene with thermal annealing [56]. Graphene devices in this study were suspended over trenches etched from the substrate and Bao et al. concluded that the observed periodic rippling in the suspended graphene resulted from substrate-imposed boundary conditions and from the thermally and/or spontaneously induced strain associated with these boundaries. In another study, Meyer et al. observed corrugations on the order of 2-20 Å high and 20-200 Å wide in free-standing graphene, shown in Figure 7, and came to a different conclusion [55]. Theoretical predictions indicate that graphene will develop intrinsic rippling due to the thermodynamic instability of the 2D sheets [45,60] and Meyer et al. point to this explanation for the observed corrugations in their transmission electron microscopy (TEM) study. It has been suggested that these so-called ‘intrinsic ripples’ develop naturally due to thermal fluctuations when graphene is separated from bulk graphite during the mechanical exfoliation process and that these ripples will persist statically for substrate-supported graphene, perhaps in combination with substrate-induced topographic features [45]. Yet studies of the

relationship between substrate morphology and graphene morphology have generated conflicting conclusions.

One attempt to characterize the relationship between graphene morphology and the underlying substrate found graphene to be significantly more corrugated than the SiO₂ substrate [58]. In this study, scanning tunneling microscopy (STM) was employed to measure graphene surface topography (Figure 8a) while AFM was utilized to measure the topography of the underlying substrate (Figure 8c). They determined a roughness of $\sigma_{\text{rms}} = 0.32$ for graphene on SiO₂ and $\sigma_{\text{rms}} = 0.25$ for bare SiO₂ and conclude that the graphene exhibits short-scale corrugations not induced by the substrate, which they attribute to partly free standing regions of graphene over the SiO₂.

In contrast, Ishigami et al. reported an ambient AFM measurement across the boundary of the graphene and the SiO₂ substrate and concluded a graphene morphology approximately 60% smoother than the underlying substrate [54]. This result is consistent with the morphology of graphene being determined by the underlying substrate. A study of graphene on mica provides further evidence for the substrate-determined graphene morphology [59]. Lui et al. measured the corrugation of graphene on mica, an atomically flat surface, utilizing ambient AFM and found that the graphene on mica exhibits the same r.m.s. roughness as cleaved graphite ($\sigma_{\text{rms}} \sim 23$ pm), within the noise limitations for the AFM measurement (Figure 9); both are atomically flat. This data shows that if intrinsic ripples exist in graphene, they can be

strongly suppressed by the van der Waals interactions between graphene and the substrate for an appropriate choice of substrate. Further studies of the graphene substrate relationship are needed to fully understand the origins of graphene corrugations, motivating the work discussed in Chapters 4 and 5.



Figure 7: TEM image of free standing graphene. The free standing graphene exhibits ripples (image from Reference [55])

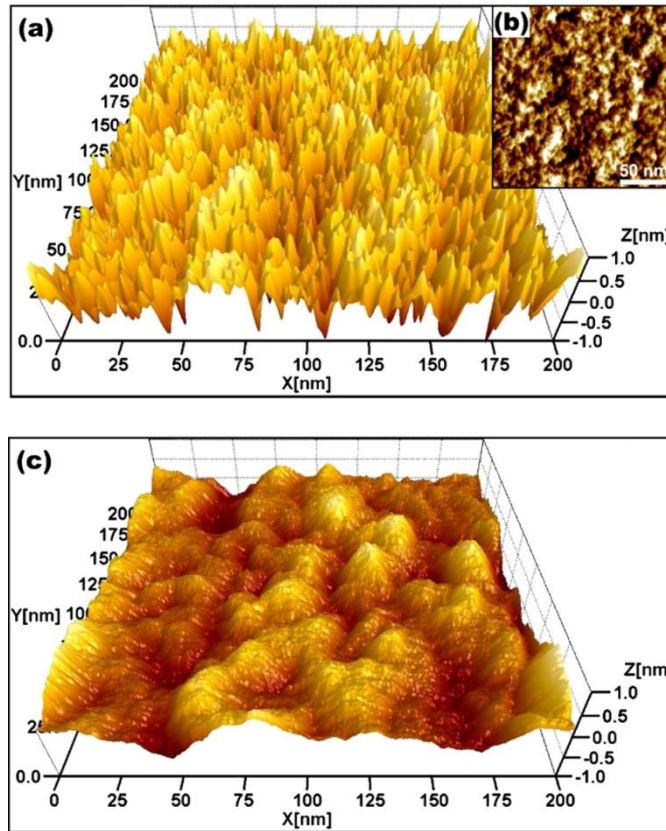


Figure 8: (a) STM image of the surface corrugation for graphene on SiO₂ (b) ambient AFM image of the SiO₂ substrate. (from Reference [58])

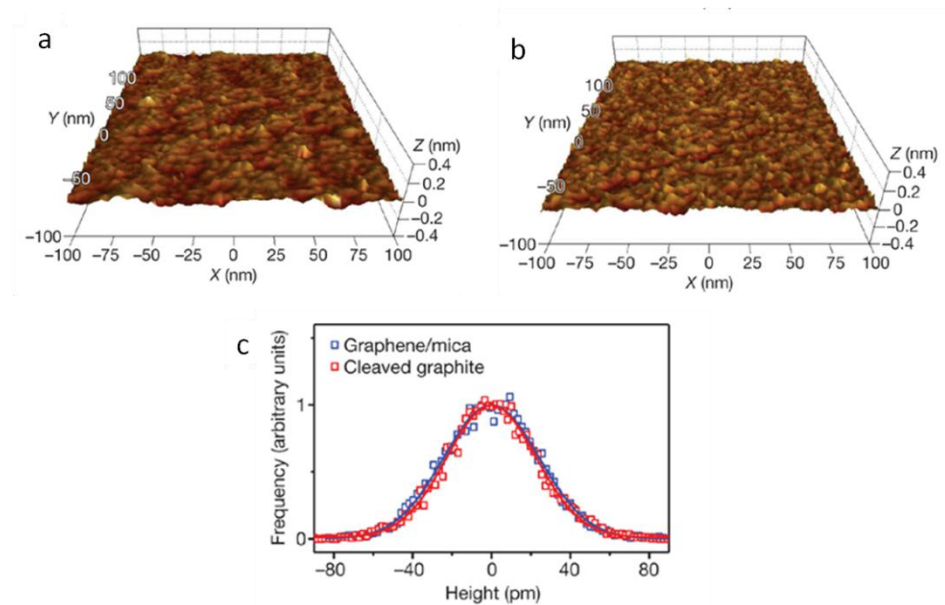


Figure 9: (a) AFM of graphene on mica. (b) AFM topography for cleaved Kish graphite. (c) Height histograms for graphene on mica (blue) and cleaved graphite (red). (images from Reference [59])

1.6 Resonant Scatterers

Resonant scatterers, such as vacancies or adsorbates, are atomic-scale defects that generate bound states, also called “midgap states”, with an energy level very close to the Dirac point. When the Fermi energy is close to the energy of the midgap state there is a large scattering cross section; the cross section decreases as the energy is farther from the Fermi energy [61]. This physical mechanism can give rise to linear conductivity vs. gate voltage, which has been derived quantitatively using the semiclassical Boltzmann transport theory [62–64]. Modeling the strong disorder as a deep potential well of radius R , the relationship between conductivity and impurity concentration is given as:

$$\sigma_d = ne\mu_d = \frac{2e^2}{\pi h} \frac{n}{n_d} \ln^2(k_F R)$$

where n_d is the defect density and k_F is the Fermi wave vector. In an experimental work, Chen et al. [65] intentionally created lattice defects by He and Ne irradiation and found that the electron scattering from vacancies to be consistent with the predictions from the Boltzmann transport theory (e.g. the observed electronic properties were attributed to the midgap states), but that charged impurities were the fundamental limiting factor for pristine SiO₂-supported graphene mobility (rather than resonant scatterers). In particular, the addition of resonant scatterers to graphene was seen to modify the mobility, but not the charge inhomogeneity n^* , suggesting that n^* is determined by charged impurities, while the near-universal minimum conductivity observed by many groups indicates that charged-impurity scattering is dominant in determining the mobility. Jang et al. studied the effect of dielectric environment on graphene’s conductivity and concluded that charged impurities

dominate the scattering [31], though the result has been controversial [29,32]. The resonant scatterers lead to intervalley scattering, which can be evidenced by the observation of a D peak in Raman spectra. Ni et al. observed a universally present Raman D peak for graphene samples, which they attributed to monovalent adsorbates, and concluded that resonant scatters are the limiting factor for carrier mobility in graphene [34]. Identification of the limiting mechanism for graphene mobility continues to be the source of some debate.

1.7 Conclusion

Given the current literature on graphene transport, charged impurity potentials, and graphene corrugation, it is clear that surface studies can provide a wealth of information on this ‘all surface material’. It is also clear that the choice of substrate plays a crucially important role in determining graphene mobility and corrugation. While STM studies have offered valuable insight into the corrugation and charged impurity landscape for graphene on substrates, directly observing the sources leading to electron and hole puddles and developing an understanding of what limits graphene mobility for non-suspended samples require detailed surface studies of the substrates themselves.

In this thesis, graphene substrates are characterized using atomic force microscopy. These measurements are correlated with available transport data. Specifically, high resolution atomic force microscopy (AFM) is used to determine substrate corrugations [66–68](Chapter 5) while simultaneous AFM and Kelvin probe force

microscopy (KPFM) are used to identify the charged impurity landscape of the substrates [69](Chapter 6). Comparing the charged impurity density extracted from the Kelvin Probe images with known transport measurements reveals the extent to which charged impurities limit graphene mobility. Furthermore, correlation of charged impurity density, substrate roughness, and transport measurements for graphene on common substrates (SiO_2 , BN), provides foundational information necessary to predict and tailor graphene device performance based on substrate properties, thus allowing for facile identification of ideal substrates prior to labor intensive device preparation.

While the focus of this research is motivated by graphene, the substrates studied are utilized in other areas of nano-science and electronics, and hence a careful fundamental characterization of the substrate surface properties will be relevant beyond the graphene community.

Chapter 2: Sample Preparation Techniques

Tool box, scotch tape, hope

Sample destruction factory

Maybe tomorrow

2.1 Graphene Device Fabrication

Theoretical work on graphene has existed since the 1940s, yet the experimental realization of graphene – electronically isolated from the substrate and therefore suitable for electronic transport experiments - did not come to fruition until 2004 as it depended upon developing a fabrication approach that would yield a crystalline single atomic layer of carbon on an insulator. Key to Geim and Novoselov’s ground-breaking work on graphene was the discovery that graphene could be identified optically when ‘exfoliated’ onto a 300 nm thick SiO₂ layer [7] due to a weak absorption of light by the graphene enhanced by a $\frac{3}{4}$ -wavelength interference in the SiO₂ film [70]. Conveniently, the combination of Si/SiO₂ makes a functional platform for MOSFET devices and as a result much of the initial transport measurements on graphene used SiO₂ as the substrate. While fabrication of graphene via mechanical exfoliation has been shown to produce the highest quality graphene transistors for the study of fundamental physics questions in graphene [16], in order for graphene and other two-dimensional materials to become a viable option for electronics applications, large-scale processes for the production of high-quality two-dimensional materials with uniformly reproducible results are also being pursued.

Concurrent with the development of mechanical exfoliation of graphene in the Manchester group, Walt de Heer's group developed epitaxial growth of single-layer graphene sheets by thermal decomposition on the (0001) surface of 6H-SiC [13]. Growth of graphene by chemical vapor deposition on metals [71] and subsequent transfer of graphene to insulating substrates [11,72] is also being pursued as a route to large area graphene. In chemical vapor deposition, a metal substrate aids in the decomposition of carbon containing gases at elevated temperatures (within a furnace) to nucleate growth of graphene films. Chemical vapor deposition and epitaxial growth of graphene are rapidly advancing and have great potential to lead to graphene production that is industrially viable [10,12,14,72–74], but mechanically exfoliated flakes continue to most consistently produce devices with the highest electronic mobility.

The graphene devices in this work (Chapters 5 and 6) were created by the mechanical exfoliation method (or the 'Scotch tape' method). Starting with Kish or natural graphite, tape (3M "Scotch" brand pressure sensitive tape) is utilized to deposit graphene on top of 300nm SiO₂ on highly doped Si. The highly doped Si serves as the back-gate for MOSFET devices (metal oxide semi-conductor field effect transistor devices). Thin graphene is identified by optical microscopy (the 300nm SiO₂ layer thickness allows for optical identification of monolayer graphene), as shown in Figure 10 [75,76]. Monolayer regions of graphene are confirmed with Raman spectroscopy, which allows for clear identification of monolayer and bilayer

regions due to the distinctive single Lorentzian shape of the 2D peak (wavenumber $\sim 2700\text{cm}^{-1}$) for monolayer graphene and the differences in intensity between the 2D and G peaks (wavenumber $\sim 1580\text{cm}^{-1}$) [77] (Figure 11). Additionally, the Raman spectroscopy may show a D peak at wavenumber $\sim 1350\text{cm}^{-1}$ indicating the presence of edges or defects. Electrodes are patterned via electron beam lithography or shadow mask, and thermal evaporation is used to deposit 3-5 nm chromium or titanium as a wetting layer followed by ~ 100 nm of gold. Finally, devices are subjected to a forming gas anneal to remove resist residues [54].

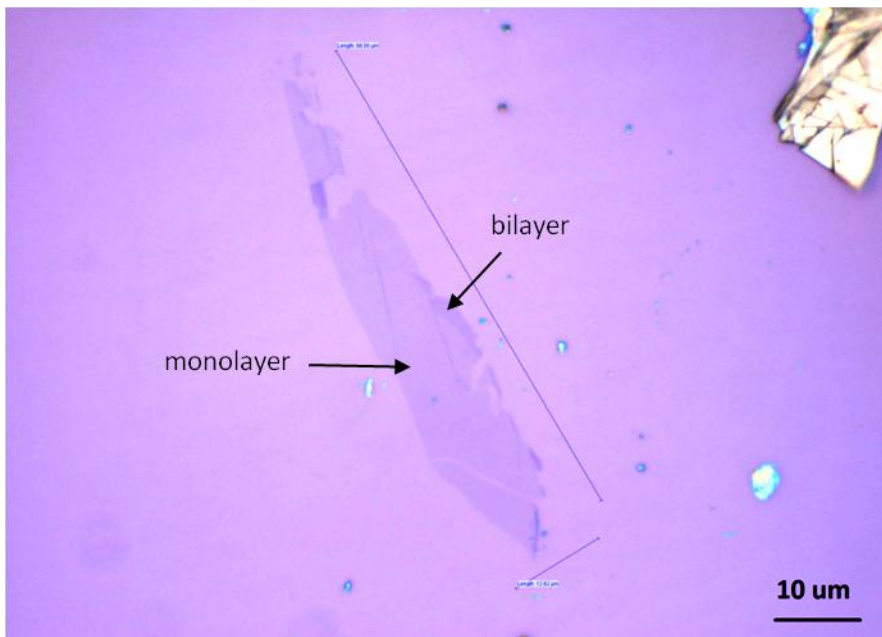


Figure 10: Optical micrograph of large monolayer flake of graphene

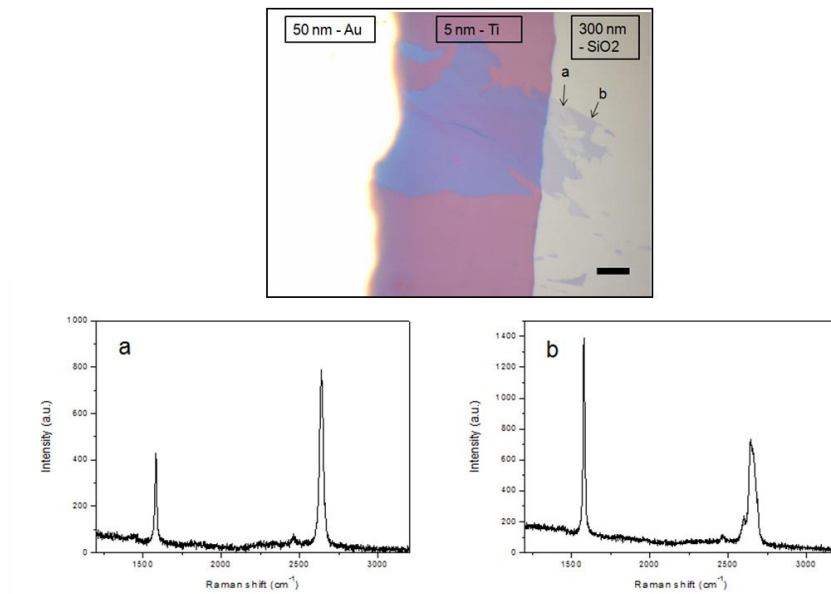


Figure 11: Raman Spectroscopy from a graphene sample over (a) monolayer and (b) bilayer graphene flake shown in optical micrograph (top). The 2D peak can be fit by a single Lorentzian for the monolayer graphene, while for the bilayer a two peak fitting is required (evidenced here by the asymmetry). The ratio of the 2D to G peak intensity also distinguishes monolayer from thicker layers.

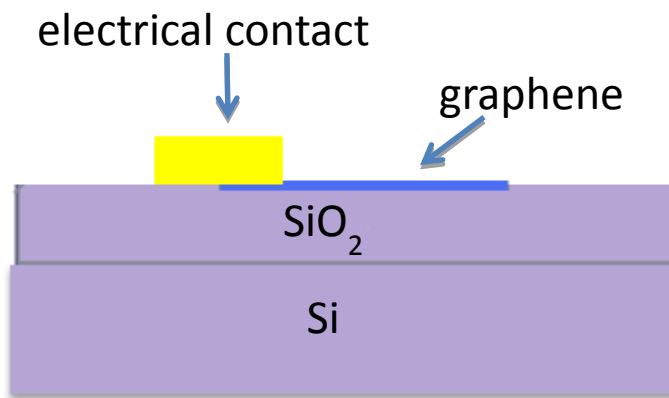


Figure 12: Schematic of graphene device structure

2.2 Small Molecule Organic Deposition

In addition to graphene, this thesis considers small molecule organics for photovoltaic applications (Chapter 7). The preparation of these devices is discussed here. Small molecule organic deposition for this work is performed *in situ* in the JEOL scanning probe microscope (Chapter 3) utilizing a Knudsen cell. For small molecule organics

on metals, it is of particular importance to have a clean metal surface before depositing the small molecule organics for the development of regular film morphologies free from contamination and irregularities. This is achieved by several rounds of annealing and sputtering. In Chapter 7, Ag(111) substrate surfaces were prepared by physical vapor deposition of Ag onto cleaved mica surfaces, followed by several cycles of Ar ion sputtering (1000 V, 30 min) and annealing by resistive heating (683 K, 20 min). After sputtering and annealing, the small molecule organic source may be degassed; the degas temperature depends on the molecule being deposited. For C₆₀, 250°C degas temperature is used; For, TiOPc 150-190 °C is used. The degas time depends on how recently the source has been used; typically 10-15 minutes is sufficient, but monitoring the pressure for stability is a good indicator of a successful degassing. Sometimes the degas procedure may be done twice to ensure success.

Film morphology for small molecule organics can be highly sensitive to a number of deposition factors including the flux rate, sample temperature, substrate preparation, and post deposition annealing [78,79]. For the deposition in Chapter 7, sequential physical vapor deposition of the organic molecules was performed onto the room temperature Ag(111) substrate. To enhance phase separation, the more cohesive species, C₆₀, was first deposited from a Knudsen cell (source temperature 610 K) to produce submonolayer (0.3-0.4 ML) C₆₀ films with close-packed island structures. The TiOPc was then deposited from a separate Knudsen cell (source temperature 490

K) at low flux rate (0.1 ML/min) to complete the monolayer with TiOPc in the thermodynamically favored honeycomb phase.

Chapter 3: Scanned Probe

Fine tip, atom sharp

Glorious images scanned

Scientist's delight!

Scanned probe microscopy is the primary technique used in this work for the determination of topographic and potential features of surfaces. This chapter includes background on scanning tunneling microscopy, atomic force microscopy, and Kelvin probe force microscopy. It also provides information on the JEOL ultrahigh vacuum microscope used for the experiments in this thesis.

3.1 Scanning Tunneling Microscopy

Scanning tunneling microscopy (STM), a surface technique allowing for topographic imaging of individual atoms, was developed by Gerd Binnig and Heinrich Rohrer in 1981 [80,81]. Only five years later, in 1986, they were awarded the Nobel prize [82]. STM employs a sharp metal tip (ideally atomically sharp) to probe a conducting surface. The tip is brought sufficiently close to the sample to produce a tunneling current (J_T) which depends on the bias (V_T), the tip-sample distance (s), and the geometry and materials of the tip and sample. The tunnelling current decays exponentially with increasing tip-sample distance. The STM tip is rastered across the sample to produce an image using x and y piezos (shown as P_x and P_y in Figure 13). It may be operated in constant height mode with the z piezo position (labelled at P_z in Figure 13) fixed or in constant current mode with a feedback loop controlling the z

piezo position to produce a specified tunneling current. In this work constant current mode is utilized and although STM can enable careful characterization of electronic states [83,84], here it is only used as a topographic imaging tool.

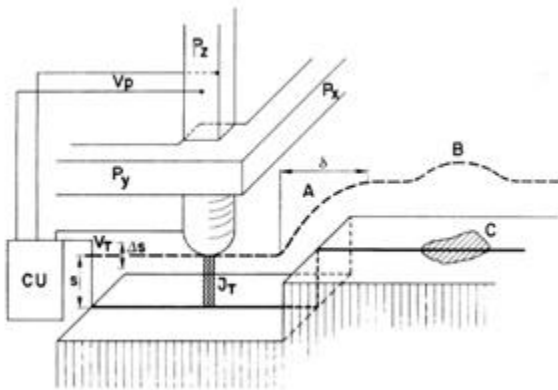


Figure 13: Schematic of STM (from Ref [80])

3.2 Atomic Force Microscopy

Atomic force microscopy (AFM) is a complimentary technique to STM, providing true topographic data for surfaces, decoupled from the electronic states. AFM was introduced by Binnig, Quate, and Gerber in 1986 [85,86], and since its invention the AFM has been modified to include a host of unique imaging capabilities including magnetic measurements, friction measurements, imaging in liquids, local surface potential measurements (Kelvin probe microscopy), and 3D force spectroscopy. The problems investigated with AFM are as diverse and interesting as the microscope itself, ranging from direct imaging of the DNA double helix structure [87] to careful investigations of bonding forces [88–90] to identification of the length of individual bonds within a molecule [91–93].

Like its precursor the STM, the AFM utilizes a sharp tip, a piezo based x, y, z positioning system, and feedback loops to probe surface topography. Unlike the

STM, the AFM can probe both conducting and non-conducting materials since the microscopy is based on the interaction force between the tip and the sample instead of the tunneling current. The AFM may be operated in contact mode, tapping mode, or non-contact mode, but the discussion here is limited to non-contact atomic force microscopy (NC-AFM) as utilized in this work.

Figure 14 displays a schematic of the NC-AFM, diagramming the basic operation of the AFM. The cantilever is oscillated at its resonance frequency(f_0):

$$f_0 = \frac{1}{2\pi} \sqrt{\frac{k}{m^*}} \quad (3)$$

where k is the spring constant and m^* is the effective mass. The cantilever motion is monitored by the laser and photo detector. Any forces between the tip and the sample (magnetic, van der Waals, electrostatic, etc.) will cause a shift in the frequency (dependent on the force gradient, k_{ts}), $f = f_0 + \Delta f$, where Δf is:

$$\Delta f = \frac{f_0}{2k} \int_A^{-A} k_{ts}(z - q') \frac{\sqrt{A^2 - q'^2}}{\pi A^2/2} dq'$$

$$\text{where } k_{ts} = -\frac{\partial F_{ts}}{\partial z} = -\frac{\partial^2 V_{ts}}{\partial z^2} \quad (4)$$

Provided that the surface is electrostatically and magnetically homogeneous, operating the z-piezo feedback to give a constant Δf will result in a fixed tip-sample distance based van der Waals and short range forces, yielding a true topographic

image. It is useful to have a metric for comparing Δf for different drive amplitudes (A); this is the normalized frequency shift (γ):

$$\gamma(z, A) = \frac{kA^{\frac{3}{2}}}{f_0} \Delta f(z, A) \quad (5)$$

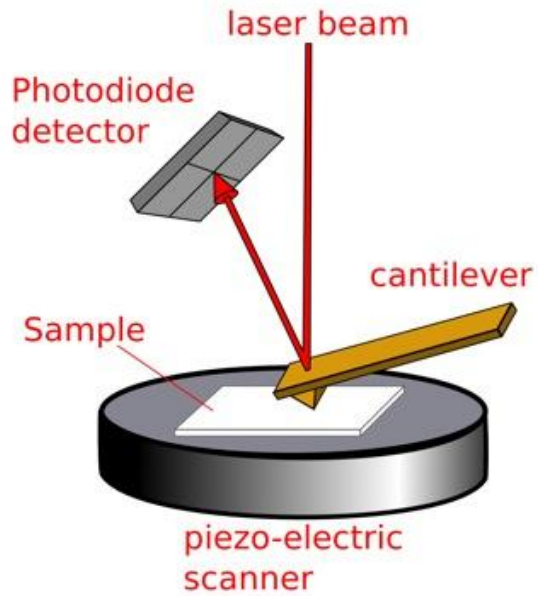


Figure 14: Schematic diagram of atomic force microscopy (AFM). A quadrant photodiode is used to detect the motion of the cantilever. (image from [94])

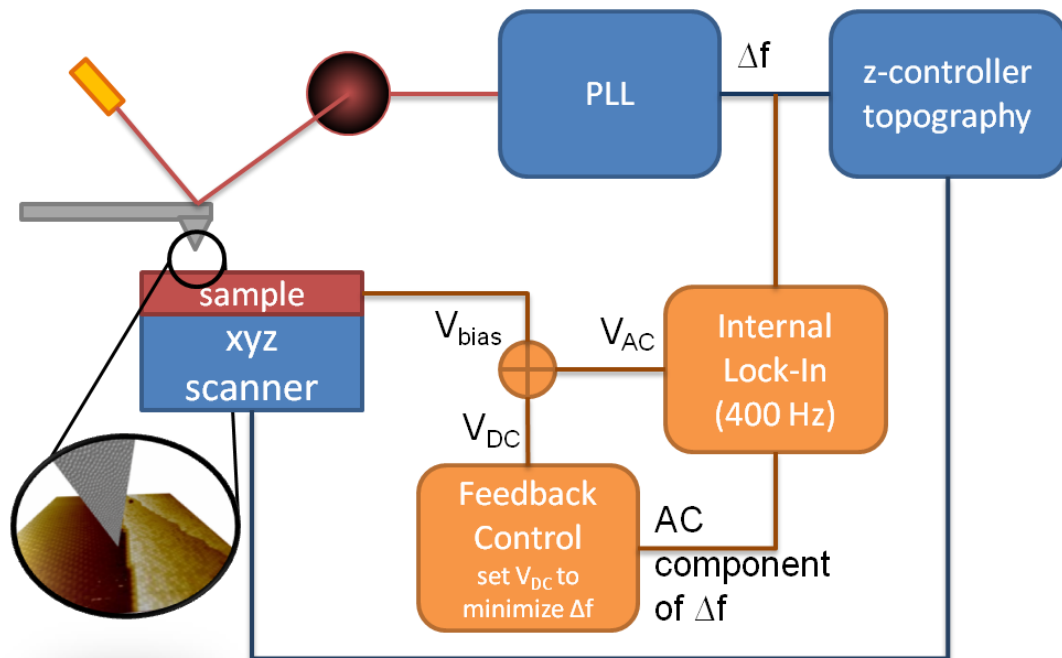


Figure 15: Schematic diagram of atomic force microscope with Kelvin probe

3.3 Kelvin Probe Force Microscopy

Kelvin Probe Force Microscopy (KPFM) [95,96] is an adaptation of AFM which provides images of the local surface potential by exploiting the electrostatic force between the tip and the sample. KPFM is an extension of a commonly used macroscopic technique for measuring material work function by an oscillating capacitor (as originally employed by Lord Kelvin). While the macroscopic technique considers the periodic change in the circuit current due to the capacitor oscillation, the AFM based technique considers the relationship between the electrostatic force (F_{el}) and the work function difference ($\Delta\Phi$) as follows:

$$F_{el} = -\frac{1}{2} \frac{\partial C}{\partial z} \left(\frac{\Delta\Phi}{e} \right)^2 \quad (6)$$

With the addition of an oscillating voltage $V_{tip} = V_{DC} + V_{AC} \sin(\omega t)$, the electrostatic force between the tip and the sample becomes:

$$F_{el} = -\frac{1}{2} \frac{\partial C}{\partial z} \left\{ \left(\frac{\Delta\Phi}{e} - V_{DC} \right)^2 + 2 \left(\frac{\Delta\Phi}{e} - V_{DC} \right) V_{AC} \sin(\omega t) + \frac{V_{AC}^2}{2} (1 - \cos(2\omega t)) \right\} \quad (7)$$

The second term in this force relationship is of special interest for Kelvin probe. If the DC voltage is equal to the contact potential difference ($\frac{\Delta\Phi}{e}$), F_{el} and therefore Δf as given by Equation (4), will be minimized. Kelvin Probe microscopy exploits this property by utilizing a feedback loop locked to the AC voltage (also detectable in the second term above) and tuning V_{DC} to minimize Δf . The approach results in a mapping of the local CPD or local surface potential since $V_{DC} = \frac{\Delta\Phi}{e}$.

KPFM can be implemented in a variety of ways. It can be conducted simultaneously with AFM, running multiple feedback loops or it can be conducted in interleave mode, where a line of topography data is immediately followed by a line of Kelvin data. Additionally, Kelvin operation may employ the natural resonance frequency of the cantilever for the voltage signal or may be operated based on an external voltage distinct from the cantilever resonance. For this work, the Kelvin set-up is operated simultaneously with the AFM measurements and uses an AC voltage of frequency 400-600Hz, as diagrammed in Figure 15. For accurate topography, the Kelvin correction must first be made before the topographic data is collected; in other words, the KPFM feedback loop must ‘run faster’ than the topographic feedback loop. To ensure that this is the case, set $\tau_{KPFM} < \tau_{AFM}$, where τ is the time constant of the feedback loop. Employing this approach with simultaneous KPFM and AFM has the advantage of deconvolving the topography image from electrostatic contributions since F_{el} is minimized [97].

3.4 JEOL UHV AFM/STM/SEM

In the work that follows, an ultra high vacuum combination STM and AFM with an attached scanning electron microscope (SEM) from the Japan Electron Optics Laboratory Co., Ltd. (JEOL) was utilized (Figure 16). (JEOL JSPM-4500A) The microscope was operated with Nanonis electronics and an OC4 Oscillator control. Provided that a metal-coated AFM tip is used, the microscope allows for real-time switching between STM and AFM imaging modes.

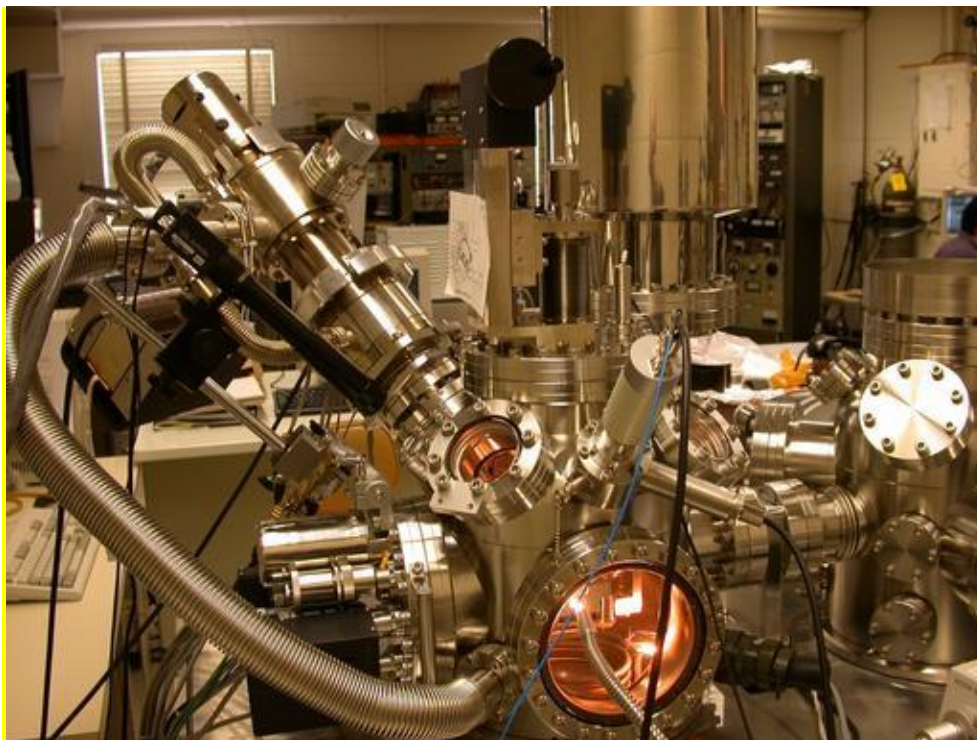


Figure 16: JEOL UHV STM/AFM with SEM used for the experiments in this thesis.

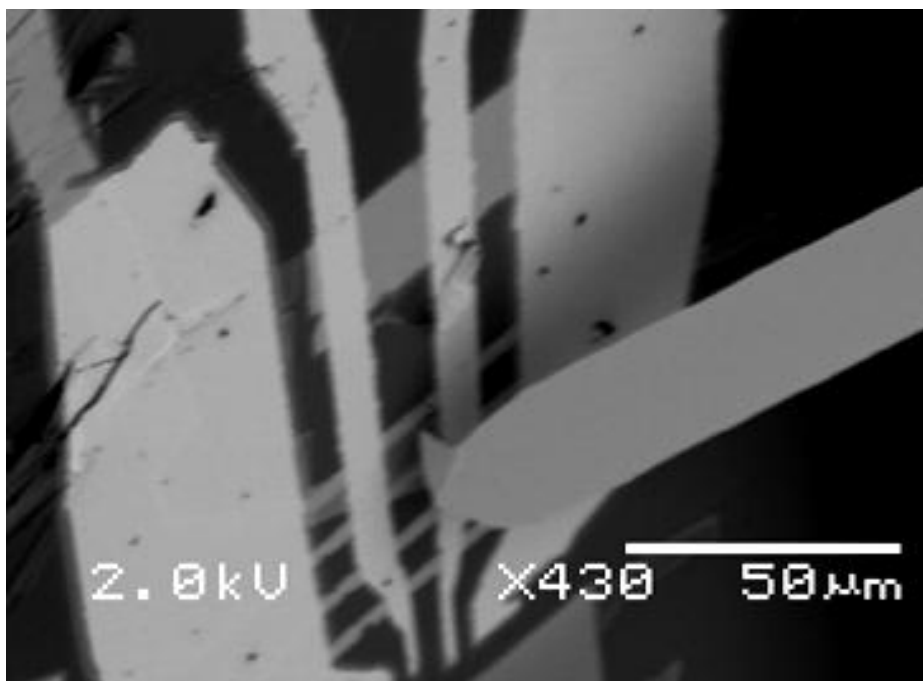


Figure 17: SEM image of the an AFM tip above a graphene sample. The metal contacts appear light grey/white and form a grid pattern while the graphene in this image is a darker gray color.

One challenge facing the scanned probe community in STM studies of mechanically exfoliated graphene is locating graphene samples in the microscope, as the flakes tend to be small and the surrounding substrate is non-conductive. The unique capability of an attached SEM on the JEOL scanned probe microscope system afforded the ability to quickly and easily locate graphene flakes within the microscope. An example SEM image of locating an AFM tip above the sample is shown in Figure 17. Other groups have utilized large flakes, high quality optics, metal substrates, or coating the sample with gold in order to successfully locate samples with the STM.

The instrument includes a separate preparation chamber which has several features that allow for *in situ* sample preparation. These include thermal deposition from a crucible, a sputtering system, and electronic feed-throughs to the sample holder for resistive heating of the sample.

Chapter 4: Corrugated Surface Resolution Model

*Scout maps rolling hills,
Flattens hills with van der Waals:
Needs finer probe tip.*

4.1 Introduction

Non Contact-Atomic Force Microscopy (NC-AFM) has brought considerable advancement to the atomic-scale study of surfaces, by allowing both atomic-resolution imaging and atomically-resolved force spectroscopy. Generally, these advancements have been made on atomically flat crystalline surfaces. Yet, many surfaces of technological interest are neither crystalline nor atomically flat, and this presents a challenge to assessing measurement resolution and ultimately determining the structures of interest. Problems of friction and adhesion serve as examples where roughness is a determining factor, and a full understanding of the microscopic interactions requires adequately resolved measurements [98,99].

SiO₂ grown as a gate dielectric on Si wafers, for example, is amorphous and exhibits stochastic surface roughness. Precise measurement of this roughness by AFM has become controversial and important due to the widespread use of SiO₂ as a support for exfoliated graphene, which may be probed with UHV Scanning Tunneling Microscopy (yielding full atomic resolution by several groups) [3-7]. Controversy arises when STM measurements of graphene/SiO₂ are compared with AFM

measurements of the bare SiO₂ substrate, because AFM measurements of SiO₂ generally show a much smoother topography than STM of graphene/SiO₂. This controversy is discussed more thoroughly in section 1.5 (and is touched upon again in chapters 4 and 5). Motivated by the experimental difficulty in measuring SiO₂ surfaces, my co-worker William G. Cullen and I propose a model to gain insight on this issue.

This chapter presents a model of the tip-surface interactions for the case of a corrugated surface. We discuss the issues which arise when the surface is corrugated at relatively small length scales (the best measurements of SiO₂ from section 5.2 yield a correlation length of 8-10 nm). A continuum model is developed which explicitly accounts for a quasi 1D substrate corrugation (modeled as a sinusoid) and the response of a spherical tip to van der Waals interactions is obtained. To my knowledge, it is the first model to directly incorporate the lateral variation of van der Waals forces due to surface corrugation and attempt to quantify this in terms of contours of constant frequency shift. The first results of this model are discussed, specifically showing attenuation of the substrate corrugation in imaging. A deviation from the generally-assumed Hamaker force law for the interaction of a sphere with a flat surface ($F \sim -A_H R / 6z^2$) is also discussed. First, I expand upon the experimental motivation for developing the model.

4.2 Experimental Motivation

While one may readily obtain atomic resolution on certain flat surfaces, such as the well studied 7×7 reconstruction of Si(111), obtaining this same level of resolution on rough surfaces presents an experimental challenge. Under suitable conditions, atomic resolution of amorphous surfaces has been achieved. For atomically resolved images of barium silicate glass, UHV contact mode AFM with relatively high loading force (25 – 50 nN) was utilized [100]. Quartz glass has also been measured with comparable resolution, leading to real-space images of the amorphous atomic structure [101]. Despite the atomic resolution obtained for quartz in Ref. [101], due to apparent differences in surface structure between the carefully UHV-prepared quartz in that study and the SiO₂ substrates used for graphene, those measurements fail to account for the observed topography of SiO₂-supported graphene. As with the barium silicate measurements, for high-resolution measurements of SiO₂, special conditions were necessary [101]. In order to obtain the high-resolution measurements of the SiO₂ presented in the next chapter (Chapter 5), a super-sharp tip, with a nominal radius of curvature of 2 - 5 nm, was crucial (tips with larger radius of curvature do not sufficiently resolve the nanometer scale features). Yet, under comparable experimental conditions, the 7×7 structure of Si(111) could be discerned with atomic resolution without the aid of a super-sharp tip (Figure 18). Atomic resolution on Si(111) depends on the chemical short-range forces and the bonding configuration of the tip apex atom [102–105], while long-range vdW interactions are a constant background force for AFM imaging of this and other flat surfaces. In contrast, for corrugated surfaces, the vdW interactions will vary laterally and thus play a greater

role in determining the contour followed by the probe tip. These experimental observations highlight the difficulty in obtaining adequately resolved NC-AFM measurements on rough, amorphous surfaces and challenge the assumption that, for a given tip radius, the resolution on a rough surface will be comparable to the resolution on a flat surface. In the following section, I develop a minimal model for NC-AFM of corrugated surfaces and further discuss the NC-AFM resolution challenge for rough surfaces. While it is the controversy over the resolution of the SiO₂ substrate that motivates the modeling of NC-AFM resolution for corrugated surfaces, the vdW interaction model presented in section 4.3 is more generally applicable to other corrugated surfaces.

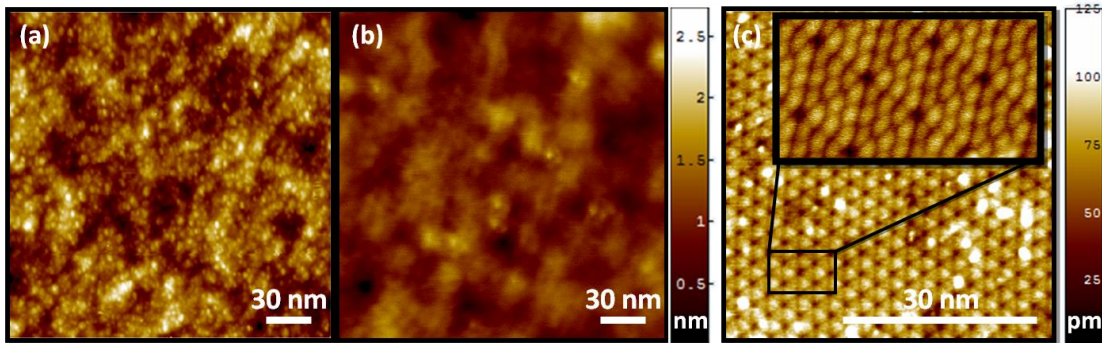


Figure 18: AFM Resolution Examples: (a) high resolution UHV NC-AFM image of SiO₂ displaying features with radius of curvature ~ 2.3 nm (R_{tip} nominally 2 nm, $\Delta f = -20$ Hz, $A = 5.0$ nm, image size = 200 nm x 200 nm) (b) under-resolved UHV NC-AFM image of SiO₂ with the same height scale as (a) (R_{tip} nominally 30 nm, $\Delta f = -150$ Hz, $A = 1.0$ nm, image size 200 nm x 200 nm) (c) UHV NC-AFM image of Si(111) with inset showing atomic resolution (R_{tip} nominally 10 nm, $\Delta f = -40$ Hz, $A = 7.1$ nm, image size 50 nm x 50 nm)

4.3 Model of the corrugated-surface resolution

Here I briefly outline the analytic development of the model. Ultimately I wish to find the dependence of potential, force, frequency shift, etc. for the case of a spherical tip and a quasi one-dimensional corrugated surface. The following sections develop the

calculation assuming that interactions are pairwise additive, beginning with a Lennard-Jones interaction between two atoms [106]. The formalism here closely follows that of Reference [107], where a detailed analytical theory was developed to model the adhesion of graphene to a sinusoidally corrugated substrate.

This section is presented as follows:

1. Develop basic formalism for carrying out numerical integration of a Lennard-Jones potential, for a “point atom” interacting with a semi-infinite substrate. By obtaining this “point atom” potential, one can then integrate over the tip volume to obtain the tip-surface potential. I first obtain results for a flat surface with boundary at $z = 0$, first for the “point atom” and then for a spherical tip body. These allow a check on the numerical integration scheme by comparison with analytical results.
2. The method is applied to a corrugated surface. As an intermediate result, the tip-surface potential and its z -dependence is discussed since the scaling is different than the sphere-plane result generally assumed.
3. Finally, to simulate NC-AFM imaging, frequency shifts for the spherical tip / corrugated surface system are computed.

I begin with the Lennard-Jones potential written as:

$$w_{LJ}(r) = -\frac{C_1}{r^6} + \frac{C_2}{r^{12}} \quad (8)$$

which represents the interaction between a pair of atoms separated by distance r . Following the Hamaker procedure, I assume that the total interaction energy (atom-surface or tip-surface) is obtained pairwise by integration of this potential.

4.3.1 Atom-surface potential

I first consider a “point atom” interacting with a flat, semi-infinite substrate with density ρ_s (number/volume). The integration may be written as

$$w_{a-s}(z) = \int_{-\infty}^{\infty} dx'_s \int_{-\infty}^0 dz'_s \int_{-\infty}^{\infty} dy'_s w_{LJ}(r) \rho_s \quad (9)$$

As shown in Reference [108], this has an analytic solution. For a general potential described by

$$w(r) = -\frac{C}{r^n} \quad (10)$$

the substrate-integrated potential is

$$w_{a-s}(z) = -\frac{2\pi C \rho_s}{(n-2)(n-3)z^{n-3}} \quad (11)$$

and this is valid for $n > 3$. Here z represents the distance from the “point atom” to the substrate surface. I use subscript “a-s” to denote that this is a potential for an “atom” interacting with the semi-infinite substrate.

For $n = 6$ (the usual attractive vdW form) this reduces to

$$w_{a-s}(z) = -\frac{\pi C \rho_s}{6z^3} \quad (12)$$

Combining the attractive r^{-6} term and repulsive r^{-12} term, the result may be expressed as

$$w_{a-s}(z) = w_0 \left[-\frac{3}{2} \left(\frac{h_0}{z} \right)^3 + \frac{1}{2} \left(\frac{h_0}{z} \right)^9 \right] \quad (13)$$

with

$$w_0 = \frac{\pi C_1 \rho_s}{9 h_0^3} \quad (14)$$

By inspection, it is apparent that Equation (13) represents a potential with depth w_0 at distance h_0 from the surface. Additionally, one sees that choosing (w_0, h_0) is equivalent to choosing (C_1, ρ_s) according to Equation (14). Thus, in our numerical implementation I choose values for w_0 and h_0 . As a first check on our substrate numerical integration, I compare the numerical integration of Equation (9) with the analytical result in Equation (13). In this case the interaction is parameterized as $w_0 = 1.0$ aJ and $h_0 = 0.3$ nm. The agreement is excellent, as shown in Figure 19.

4.3.2 Tip-surface potential

Once the atom-surface potential is obtained, the tip-surface potential is obtained in an analogous manner. It is computed as

$$W_{t-s}(z) = \int_{V_t} w_{a-s}(z_t) \rho_t dV_t \quad (15)$$

where the uppercase W designates a potential between two extended objects.

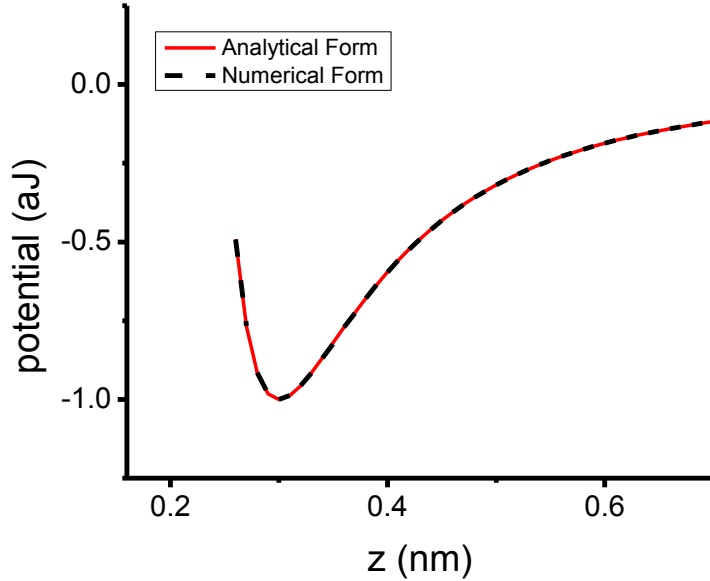


Figure 19: Verification of atom-substrate potential: Potential W_{a-s} vs. z for numerical and analytical schemes for a “point atom” interacting with a flat surface. The near-perfect overlap of the curves demonstrates the fidelity of the numerical integration scheme.

Here, ρ_t is the tip density (number/volume) and the integration is over the (spherical) tip volume. The z -coordinate for $W_{t-s}(z)$ is the distance between the surface and the apex of the spherical tip (the point closest to surface), as depicted in Figure 20. Employing the NIntegrate function in Mathematica 8.0, the numerical integration of Equation (9) generates the atom-surface potential as a tabulated function of z , with scaling determined by (w_0, h_0) . I then numerically integrate this tabulated function over the spherical tip volume, for varying tip-surface distance z , using an approach which incorporates the IDL routines INTERPOLATE and INT_3D. As a check on this numerical integration, I compare against the exact analytical result for a sphere

attracted to a flat surface by van der Waals forces. It is well-known that the sphere-plane Hamaker integration has the approximate solution [108] in the limit $z \ll R$:

$$W_{t-s}(z) \approx -\frac{A_H R}{6z}, \quad (16)$$

where A_H is the Hamaker constant for the tip-surface material system, given by $A_H = C_1 \pi^2 \rho_s \rho_t$. Equation (16) is sometimes used for fitting the vdW background in NC-AFM experiments [109,110]. However, for the tip radii modeled here, the limiting approximation is not accurate enough to serve as a test for the tip integration scheme, and I use the following exact analytical expression:

$$W_{t-s}(z) = -\frac{A_H}{6} \frac{\{2R(z+R) + z(z+2R)[\ln z - \ln(z+2R)]\}}{z(z+2R)}, \quad (17)$$

In Figure 21, I plot $-W_{t-s}$ vs z to show that the numerical integration over the tip volume accurately reproduces the exact formula. Additionally, I plot the function z^{-1} to indicate the small- z limiting behavior. In all numerical calculations the full Lennard-Jones potential of Equation (13), including both the attractive and the repulsive terms, is utilized. While the analytical expression in Equation (17) is limited to the attractive interaction, the agreement in Figure 21 is excellent.

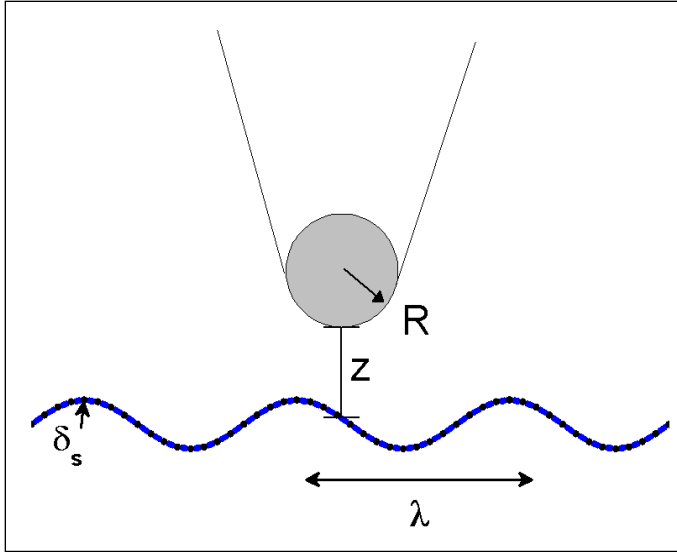


Figure 20: Schematic illustrating the model geometry: The surface is sinusoidally corrugated along the x direction only, with wavelength λ and amplitude δ_s . The surface corrugation is independent of y (quasi 1-D geometry). The tip is modeled as a sphere of radius R .

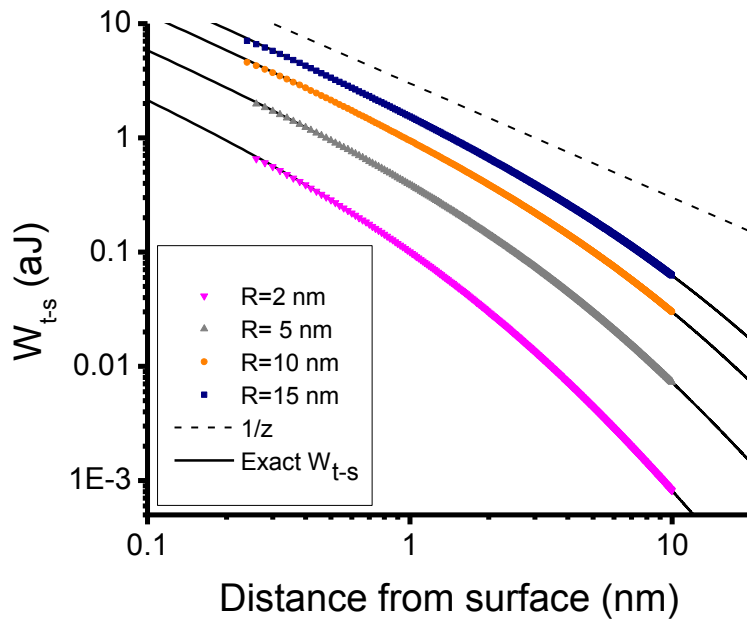


Figure 21: Hamaker Force for Flat Surfaces: Relationship between tip potential and distance from the surface. Here the distance is taken relative to the surface position (distance from surface = $z(x) - z_s(x)$). The dashed line is a reference for $1/z$ dependence expected from the Hamaker force law for the interaction between a flat surface and a sphere. The numerical results show excellent agreement with the exact potential (eqn (17))

Following these consistency checks on the numerical integrations using a flat substrate surface as a reference, I now extend the calculation to a corrugated surface. The treatment follows that of Reference [107]; in analogy with Equation (9) the atom-substrate potential is written as

$$w_{a-s}(x, z) = \int_{-\infty}^{\infty} dx'_s \int_{-\infty}^{z_s(x)} dz'_s \int_{-\infty}^{\infty} dy'_s w_{Ll}(r) \rho_s \quad (18)$$

with the essential difference being the upper integration limit on z . The upper integration limit on z is now the (sinusoidal) surface profile $z_s(x)$, given by $z_s(x) = \delta_s \sin(2\pi x/\lambda)$. Note that w_{a-s} is necessarily a function of x and z . The tip-surface potential is obtained in analogy with the flat surface calculation (Equation (15)), and is also a function of x and z .

All computations are done with $\lambda = 10$ nm, $\delta_s = 0.5$ nm, $w_0 = 0.169$ aJ, and $h_0 = 0.3$ nm. The particular choice of amplitude and wavelength is based on our best measurements of SiO₂, which have rms roughness ~ 0.38 nm and correlation length ~ 10 nm. The 10 nm period is divided in 16 intervals at which the potential is calculated (shown as black dots on the sinusoidal surface in Figure 20). In the z -direction, the grid is much finer — 0 to 40 nm in increments of 0.01 nm. The 40 nm range is necessary to incorporate realistic tip diameters, and to allow proper integration over the oscillation amplitude, as discussed below. Our scheme is motivated by simplicity; however, an adaptive grid scheme would be desirable to deal with the rapidly varying

behavior of w_{a-s} near the surface and very smooth asymptotic behavior several nm from the surface.

The computation of the atom-surface potential $w_{a-s}(x, z)$ for the corrugated surface requires some careful discussion. In Reference [107], analytical formulas are derived for the integration given in Equation (9). However, the formulae developed there ultimately make the approximation that $z \gg \delta_s$, and consequently they do not work well at relatively small z (anomalies begin to appear even ≈ 1 nm from the surface contour). This is why a final numerical integration was adopted in our work to obtain $w_{a-s}(x, z)$. There appear to be inherent numerical difficulties in computing the integral for a sinusoidal surface, and I am currently limited in the distance to the surface where I can compute w_{a-s} . For example, in the case of the flat substrate, our numerical integration routine allows computation of w_{a-s} to within 0.19 nm of the surface. In that case, the potential is in the highly repulsive regime with value $w_{a-s} \approx +24.60w_0$, where w_0 is the depth of the potential well at the minimum. The equivalent calculation for a corrugated surface with $\delta_s = 0.5$ nm and $\lambda = 10$ nm is generally limited to ~ 0.26 nm throughout most of the corrugation period (the potential cannot be computed closer than 0.26 nm to the surface). The limits on w_{a-s} carry over directly into limits on W_{t-s} , as I only integrate the tip potential where the integrand is defined. Thus within our continuum model with a perfectly rigid tip and substrate, I cannot generally take the tip into the regime where the *overall* interaction is repulsive. This is rather unsatisfactory at present, as it would be preferable to have

well-defined numerical values (even if unrealistically large), and then let the limits of the model be decided on physical grounds — peak force or stress on the tip apex, etc.

4.3.3 Calculation of frequency shifts

Once the tip-surface interaction potential W_{t-s} is obtained, the interaction force F_{t-s} is obtained straightforwardly by differentiation with respect to z . I then compute the frequency shift using the following expression [111], which is exact to 1st order in classical perturbation theory:

$$\Delta f(x, z) = \frac{f_0^2}{kA} \int_0^{1/f_0} F_{t-s}[z + A \cos(\omega_0 t)] \cos(\omega_0 t) dt \quad (19)$$

with spring constant $k = 40$ N/m and resonant frequency $f_0 = 300$ kHz. I then convert to the normalized frequency shift γ , which is defined as [102]:

$$\gamma = \frac{kA^{3/2}}{f_0} \Delta f \quad (20)$$

The normalized frequency shift is a parameter-independent (amplitude, frequency shift) representation of the magnitude of the force for NC-AFM experiments.

4.4 Corrugated Surface AFM Resolution Model Results and Discussion

Using the model, I arrive at several key results. First, I find that the generally assumed Hamaker force law for the interaction between a spherical tip and a flat surface does not hold in the case of corrugated surfaces. Second, I find that the

imaged structure is attenuated with respect to the surface geometry, even for small distances between the tip and the sample.

4.4.1 Deviation from the Sphere-Plane Hamaker Force Law

In the previous section, I discussed the Hamaker integration for a sphere interacting with a flat surface via van der Waals forces. The integration can be carried out without approximation to yield the exact formula; this exact formula is cumbersome and given by Equation (17). In the limit $z \ll R$, this formula simplifies greatly to $W_{t-s} \approx -A_H R / 6z$, which is often used in describing tip-sample vdW forces. Applying the formalism developed for a sinusoidally corrugated surface, I find that the basic scaling with distance is fundamentally different when the surface is corrugated.

Figure 22 shows the relationship between W_{t-s} and the local height above the surface [$h = z(x) - z_s(x)$] for tip radii of 5 nm and 10 nm at four high-symmetry points on the corrugated surface ($x = 0$, $x = \lambda/4$, $x = \lambda/2$, and $x = 3\lambda/4$). I compare the curves derived from the corrugation model to the exact curves corresponding to a flat surface, and additionally show the reference curve $1/z$ which represents the small- z limiting behavior for the flat surface. I see that unlike the flat case, the curves do not show a $1/z$ dependence in the limit of small tip-sample distances. Assuming a W_{t-s} versus tip-sample distance relationship of the form $1/z^\beta$, I find $\beta > 1$. This means that the tip potential drops off more quickly with increasing distance than one would expect from application of the Hamaker force law for the relationship between a

sphere and a plane. Additionally, the tip-sample distance dependence of V_{tip} varies with lateral position, showing the strongest distance dependence at the valley position ($x = 3\lambda/4$, blue curve) and the weakest distance dependence for the peak position ($x = \lambda/4$, red curve). For $x = 0$ and $x = \lambda/2$, the distance dependencies are equivalent which is consistent with the observation that these two locations are mirror symmetric in geometry. For all lateral positions studied, a departure from the sphere-plane Hamaker force law results. The departure is most pronounced when the tip is in close proximity to the surface; as the distance from the surface increases the potential converges to the exact result for a flat surface. While the deviation from the sphere-plane Hamaker force law is not mapped throughout the corrugation (λ, δ) parameter space here, I expect that for a given tip radius the deviation will decrease with longer λ and smaller δ due to decreased interaction between the tip and the substrate side walls. This prediction is consistent with the flat surface case, which will be restored in the limits $\lambda \rightarrow \infty$ and $\delta \rightarrow 0$.

4.4.2 Attenuation of Surface Features

To determine the degree of attenuation of surface features for NC-AFM, contours of constant frequency shift were calculated (Figure 23), using the method described in the previous section. Here, I present results for a tip with radius 5 nm. With increasing distance from the surface these contours show attenuation of the corrugation. As discussed in the previous section, the proximity to the surface is limited by our first numerical integration to obtain w_{a-s} . At our computational limit,

the nearest contour which I can calculate corresponds to a normalized frequency shift of $-0.72 \text{ nN nm}^{1/2}$ ($-22.8 \text{ fN m}^{1/2}$), which is well into the range at which atomic-resolution images are normally obtained [20]. Most significantly, at this interaction level the contours are attenuated by $\sim 30\%$ (lower-most contour, purple curve in Figure 23). At $-0.1 \text{ nN nm}^{1/2}$ (upper-most contour, red curve in Figure 22) the model predicts over 50% attenuation compared to the surface corrugation.

The attenuation of surface features can be understood intuitively by considering the vdW interaction of the tip and the corrugated sample surface. For flat surfaces, the vdW interaction provides a constant background and is most strongly concentrated at the tip apex, but for corrugated surfaces the vdW interactions over peak positions and valley positions are different and interactions with the side of the tip become more important. For the valley positions, the attractive force between the tip and the sides of the valley will lead to a stronger attraction than for the flat surface case and thus result in a higher z position for the same frequency shift. A similar physical argument can be made for the peak positions. In this case the downward slope means neighbouring atoms are farther away, the vdW interactions with these atoms is smaller compared with the flat case due to the increased distance, and as a result the same frequency shift will occur at a lower z position. The vdW interactions with neighbouring atoms become more dominant at larger z distances (smaller frequency shifts), and therefore one can intuitively expect greater attenuation (lowering of peak positions and heightening of valley positions) based on these simple, physical vdW arguments. A similar argument was presented by Sun et al. in describing the

attenuation in graphene moiré structure on Ir(111) due to the vdW interaction between the tip and the underlying Ir(111) structure [112]. While attenuation is to be expected for increased distance between the tip and the sample, I emphasize that the degree of the attenuation for a 5 nm-radius tip is significant even at small distances, with a normalized frequency shift that is relatively large. To obtain accurate experimental results with NC-AFM it is of critical importance to choose a frequency shift set point such that the distance between the tip and the surface is minimized, *especially* when seeking accurate topography of corrugated surfaces. The model used does not account for local bonding, electrostatic forces, or atomistic interactions beyond the inclusion of a pair-wise vdW interaction, all of which affect the AFM resolution; nonetheless, even if these interactions were included, the varying vdW and resultant attenuation of features still presents a problem to resolution.

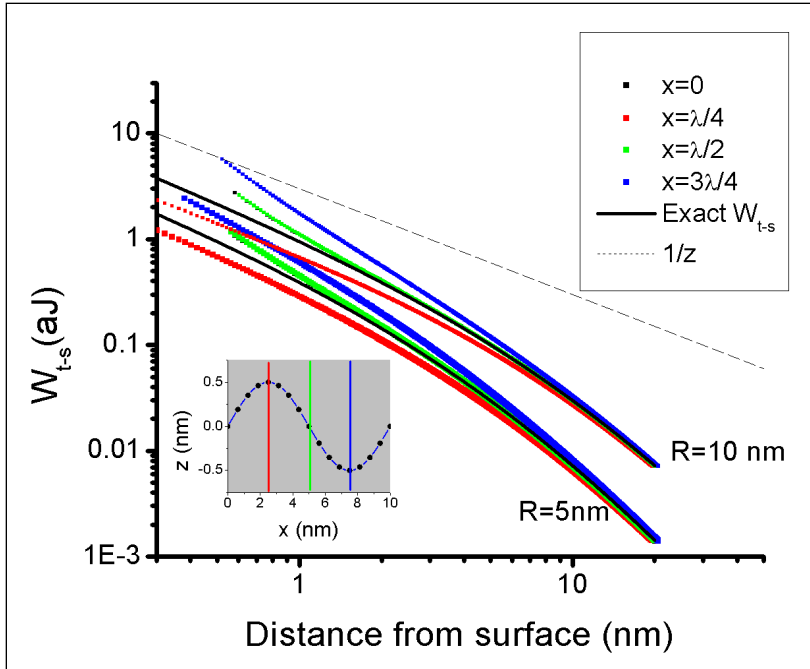


Figure 22: Hamaker Force Law for Corrugated Surfaces: Tip-sample distance dependence of tip potential for high symmetry points (inset, $x = 0$, $x = \lambda/4$, $x = \lambda/2$, and $x = 3\lambda/4$) for the two radii ($R = 5$ nm and $R = 10$ nm). Lines for the exact analytical form (eqn (17)) of the Hamaker relationship between a sphere and a plane are shown (black line) for comparison.

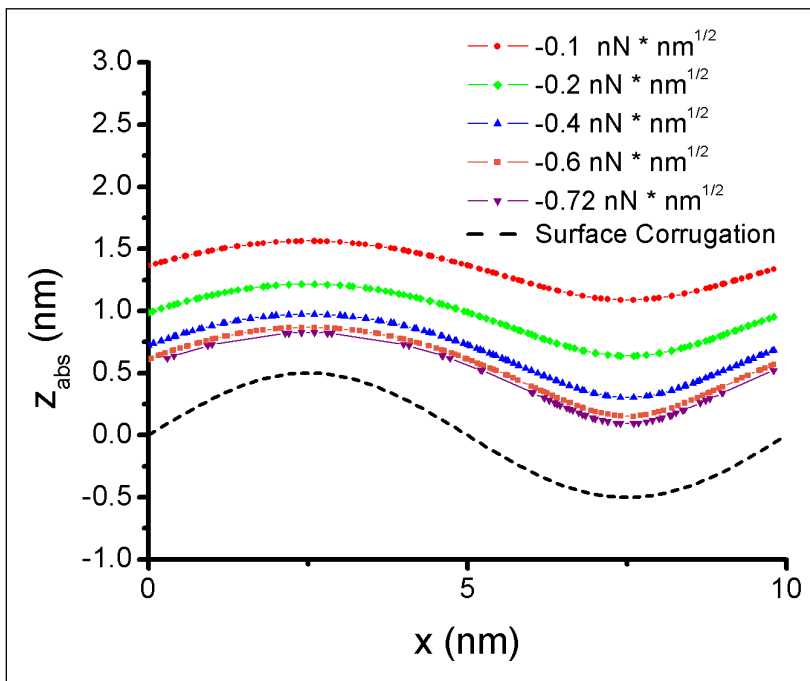


Figure 23: Contours of constant normalized frequency shift, γ , for corrugated surface with a tip of $R = 5$ nm. Attenuation is observed as distance from the surface increases. Here, z_{abs} gives an absolute position in the z -direction, not a relative distance from the surface.

4.5 Conclusions

As is already well known in the field of atomic force microscopy, a sharp tip and close proximity to the surface are key to obtaining accurate topographic images with high resolution. Here I have shown that, even more so than for flat surfaces, these factors are especially important for high resolution imaging of rough surfaces, based only on the differences between vdW interactions. While the model results support the experimental difficulty of obtaining accurate images of rough surfaces, the model itself oversimplifies the multi-faceted complexities of experimental AFM setups. More complex models, which include short-range bonding and electrostatic forces, more realistic tip geometries, and calculations for closer proximities between tip and sample, are needed for a more complete and quantitatively accurate understanding of the factors limiting resolution of corrugated surfaces.

Chapter 5: Graphene Corrugation

Craggy peaks tower

A sheet finds every crevice

Clings tight to surface

5.1 Introduction

This chapter presents a study of graphene corrugation, addressing the nanometer-scale roughness of SiO₂-supported graphene, its origin, and the unique measurement difficulties it presents for AFM. The chapter follows from publications by Cullen et al. (2010) [66], Burson et al. (2011) [68], and Burson et al. (2012) [67]. First, I revisit key previous work on graphene corrugation, presented in greater detail in Section 1.5, as motivation and context for the work in this chapter. The first investigations of SiO₂-supported graphene using scanned-probe methods appeared in 2007 [53,54]. These early investigations attributed the roughness of graphene to the roughness of the underlying SiO₂. Previously, measurements of suspended graphene by TEM in diffraction mode suggested an “intrinsic” rippling in the graphene structure [55], which has been theorized to originate from the same physics which describes the crumpling of soft membranes [113]. More recently, a study comparing scanned probe measurements of the corrugation of single-layer graphene (using UHV STM) with that of SiO₂ (using ambient AFM) reported a significantly greater corrugation of the graphene than observed for the SiO₂ [58]. These measurements were interpreted by the authors to reflect an “intrinsic” rippling of partially suspended graphene, presumed to have the same origin as that observed for fully suspended graphene using

TEM [55]. However, any significant “suspension” and intrinsic rippling of the graphene over SiO₂ is hard to reconcile with the energetics of substrate adhesion [107,114,115], as discussed in more detail below.

This chapter addresses the corrugation controversy for graphene on SiO₂. Section 5.2 presents high-resolution scanning probe topographic images of graphene and graphene substrates, showing graphene is slightly smoother than SiO₂ for all relevant lengths scales, down to a few nanometers, in contrast to the results of Reference [58]. This section also discusses the unique measurement challenges for accurate NC-AFM measurement of the topography of corrugated surfaces. In section 5.3, we consider the energetics of graphene bending and substrate adhesion and show that the observed graphene corrugation on SiO₂ is reasonable. Finally, a calculation of the predicted potential landscape that would be produced by the experimentally observed graphene corrugations from this study is presented.

5.2 High Fidelity Imaging of Graphene and the SiO₂ Substrate

In order to evaluate the relationship between graphene corrugation and substrate corrugation, high-resolution UHV scanned probe measurement of the topography of both bare SiO₂ and SiO₂-supported graphene is necessary. Graphene samples were prepared as described in Chapter 2 and scanned probe measurement details are provided in Chapter 3. Electrical contacts for the graphene samples were established by shadow mask evaporation to prevent resist contamination. Additionally, graphene and SiO₂ samples were cleaned by sonication in acetone followed by sonication in

isopropyl alcohol. Samples were heated in the scanning probe preparation chamber (*in situ*) at 130 C before imaging. STM tips were made with etched Pt-Ir wire, while high-resolution AFM was performed using an AFM cantilever with a super-sharp silicon tip of nominal radius 2-5nm (Veeco) [116]. The cantilevers have nominal force constant and resonant frequency 40 N/m and 300 kHz.

The data from the scanned probe measurements of graphene and SiO₂ are presented in this section. They show that in fact the SiO₂ surface is rougher than previously known at the smaller lengths scales not accessed in previous lower-resolution measurements [54,58]. When both the graphene and the supporting substrate are measured with high resolution, the structure of the supported graphene closely matches that of the SiO₂ at all length scales, indicating that the observed graphene roughness is an extrinsic effect due to the SiO₂ substrate; any intrinsic tendency toward corrugation of the graphene is overwhelmed by substrate adhesion, as further discussed in section 5.3.

Figure 24 compares scanned probe images of the topography of monolayer graphene on SiO₂ (image taken by STM) with bare SiO₂ (image taken by high-resolution NC-AFM). The measured rms roughnesses are 0.35 and 0.37 nm, respectively. As discussed in Chapter 4, we expect greater lateral resolution for STM images over AFM due to the difference in the measurement techniques. Hence, the greater roughness of the AFM image of bare SiO₂ conclusively indicates that graphene is

slightly smoother than the underlying SiO₂. Resolution considerations will be discussed further below.

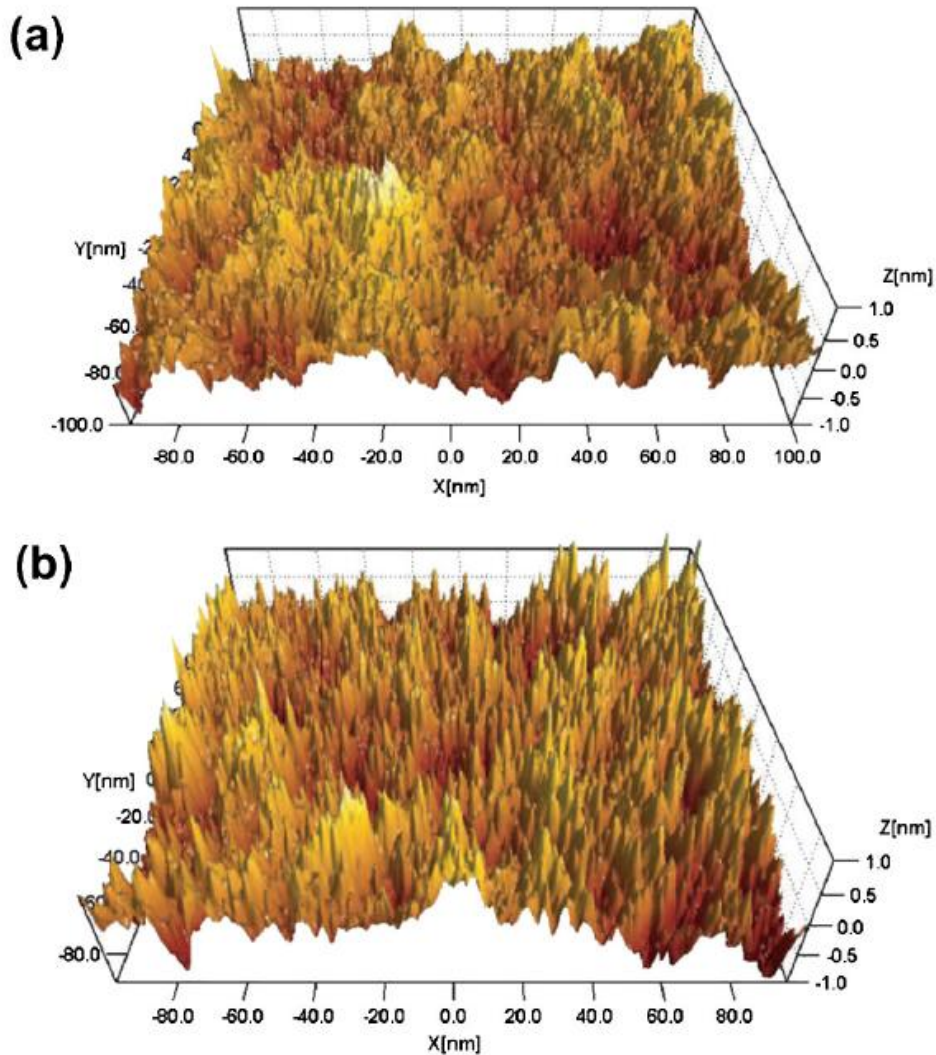


Figure 24: (a) SiO₂-supported graphene topography obtained with STM (195x178 nm, -305 mV, 41 pA) and (b) bare SiO₂ topography obtained with high-resolution NC-AFM (195x178 nm, A = 5nm, $\Delta f = -20$ Hz).

Further insight into the structure of graphene on SiO₂ may be gained by examining the Fourier spectra of the height data. The Fourier spectra are obtained as follows: SPM images were analyzed in raw form with only background subtraction. The Fourier spectra were analyzed in a one-dimensional fashion by taking the fast Fourier transforms (FFTs) along the fast-scan direction. The FFTs are averaged along the

slow-scan direction and where possible, data was additionally averaged over multiple images to increase the statistical certainty of the results.

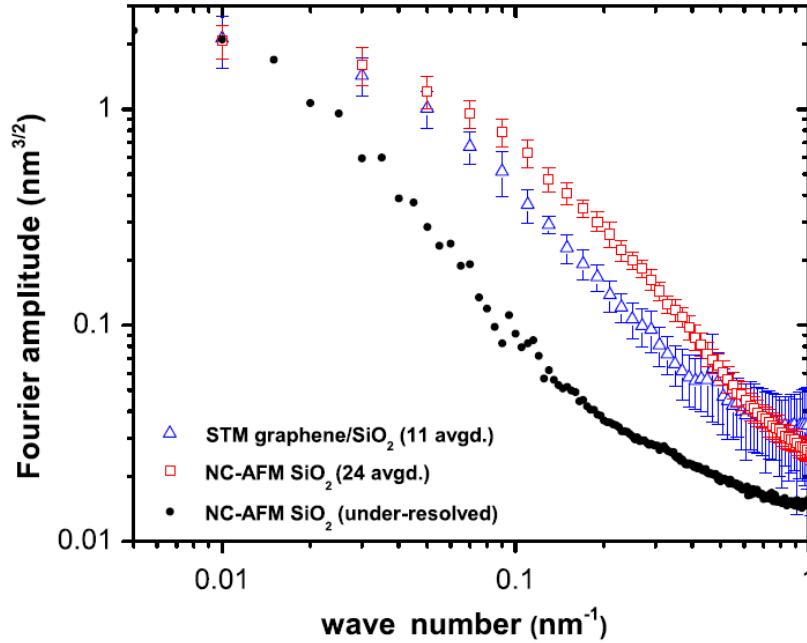


Figure 25: Fourier amplitude spectra of: SiO₂ NC-AFM (red squares), monolayer graphene/SiO₂ STM (blue triangles), and under-resolved SiO₂ (black dots). Spectra 1 and 2 were obtained from an averaged data set to establish statistical uncertainty. Wave number is defined as wavelength⁻¹.

Figure 25 shows the Fourier spectra averaged over 11 images of graphene (STM) and 24 images of SiO₂ (NC-AFM). The error bars designate 1 standard deviation based on the averaged Fourier spectra from the images. The increased corrugation of the high-resolution measurement of the oxide surface (Figure 24b) is evident in the slightly increased amplitude of the Fourier spectrum (squares in Figure 25) as compared to the graphene surface (Figure 24a and triangles in Figure 25) over the relevant length scales ~2-50 nm. The amplitude difference between the graphene/SiO₂ and the bare SiO₂ Fourier spectra is most pronounced around 0.2 nm⁻¹ (5 nm wavelength) and it should be noted that this difference is statistically significant. For wavenumbers above 0.5 nm⁻¹ instrumental noise dominates the error,

making comparison difficult. However for wavelengths of 10 nm, where intrinsic rippling was purported in Ref. [58] to dominate the graphene morphology, no graphene samples have been observed which are more corrugated than the SiO₂. Also shown for comparison in Figure 25 is the Fourier spectrum of a low-resolution measurement of the oxide surface (similar to that reported in Ref. [54]) which preserves the very-long-wavelength structure (wave number $<0.01 \text{ nm}^{-1}$) but clearly misses the structure which is seen by high-resolution NC-AFM. The slightly decreased corrugation of graphene relative to the oxide surface below is expected due to the competition between adhesion energy and elastic curvature of the graphene sheet; this competition is discussed quantitatively in section 5.3.

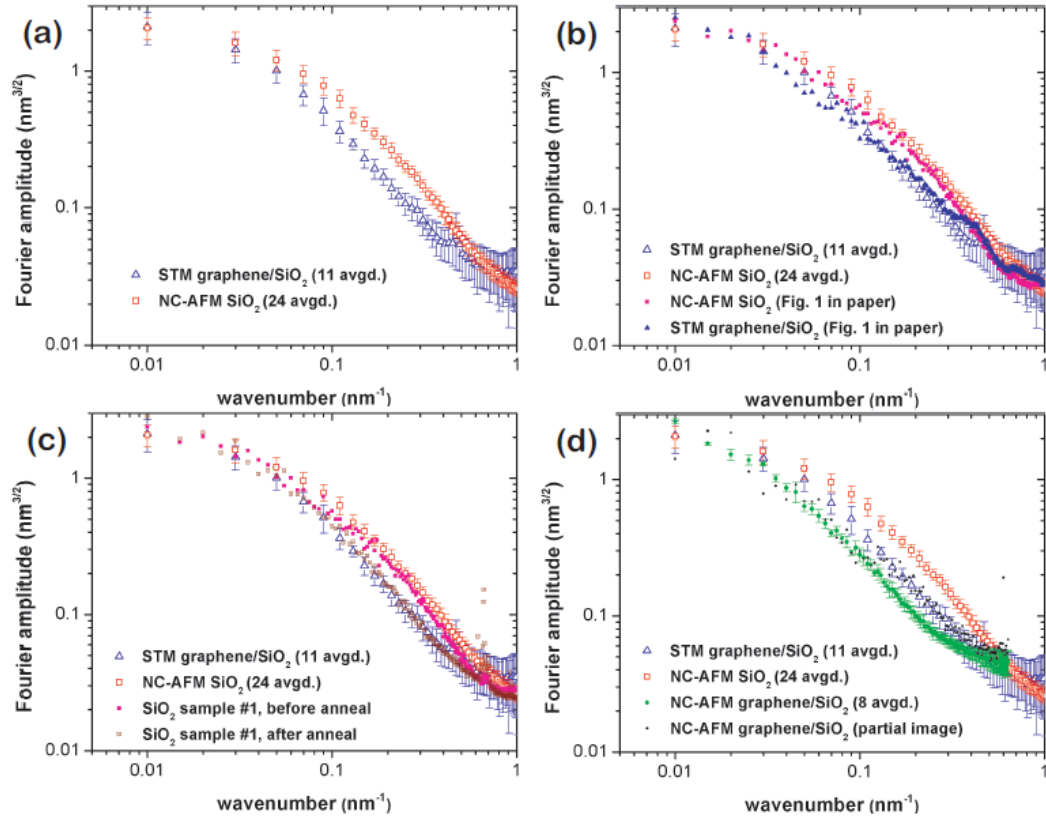


Figure 26: Extended comparison between SiO₂ and graphene. All spectra are 1-dimensional Fourier amplitude spectra. Panel (a) shows a globally averaged data set consisting of averaged measurements of two graphene/SiO₂ samples and two SiO₂ substrates, and these two curves are reproduced in panels (b-d) for specific comparisons. Open red squares indicate SiO₂ NC-AFM measurements and open blue triangles represent monolayer graphene STM measurements. Panel (b) shows Fourier spectra from the two images presented in Figure 24 overlaid with the globally averaged data set to show that they are representative. Panel (c) shows the result of annealing SiO₂ sample 1 at 500 C, also overlaid with the globally averaged data set. Panel (d) shows the Fourier spectra for NC-AFM images of monolayer graphene/ SiO₂ for comparison. Green symbols show an average over 8 images (all slightly under-resolved in comparison to STM) which are representative of Figure 27(c). Black dots are from one partial image (shown in Figure 27(b)) which is as highly resolved as our STM data. All quantities here are analyzed from raw data, with no filtering (only background subtraction). Wavenumber units are defined as wavelength⁻¹.

The images in Figure 24 are representative of the data sets for graphene/SiO₂ and bare SiO₂ substrates compared in Figure 25. This is verified by comparing the Fourier spectra of these two images to the globally averaged data set, as shown in Figure 26b.

I also explored the possible contribution to the surface roughness of adsorbed species on SiO₂. Figure 26c displays the effect of annealing in UHV for SiO₂ substrates.

Sample 1, as designated in the figure, was first heated at 130 °C in UHV prior to

imaging, as is standard preparation for all samples measured by UHV scanned probe in this section. This sample was subsequently annealed at 500 °C and imaged again. Fourier spectra from the images before and after annealing at 500 °C are shown in Figure 26c with the ensemble-averaged Fourier spectra from graphene/SiO₂ and SiO₂ shown for ready comparison. The dependence of topographic amplitude on annealing treatment for SiO₂ suggests that adsorbates may contribute to the measured SiO₂ roughness. Given that many samples are prepared in ambient, this measurement of surface topography for SiO₂ in UHV represents a lower bound for the topographic roughness that can be anticipated for as-fabricated graphene devices. Notably, the UHV measurements after removal of adsorbates which will desorb for $T \leq 500$ °C indicate a roughness comparable to that of graphene, supporting the conclusion that graphene does not exhibit corrugation greater than that of the substrate.

The level of resolution in Figure 24 is exceedingly difficult to obtain with NC-AFM, and the measurements from this study indicate that, for a comparable set of imaging parameters, the topography of graphene on SiO₂ is more difficult to resolve in NC-AFM than that of SiO₂. Figure 27a shows an STM image of the graphene/SiO₂ topography, while Figure 27b shows the highest resolution AFM image of graphene/SiO₂ obtained in this study. These two images appear to exhibit comparable spatial resolution, and this is further confirmed by considering the Fourier spectra, shown in Figure 26d. However, Figure 27c displays a more typical NC-AFM image for graphene/SiO₂; the Fourier spectra (Figure 26d) for an average of 8 images of graphene/SiO₂, reveal lower resolution of corrugation from the NC-AFM

measurement (obtained using Veeco super sharp tips [116]) than the nominally equivalent STM images. The difference in Fourier amplitudes depicted in Figure 26d results in a reduction in rms roughness of 0.03-0.04 nm. This indicates that while NC-AFM is capable of resolving the finest features for these rough surfaces, in a room-temperature cantilever-based system such as the one used in this study (Chapter 3), achieving the highest-resolution measurement is non-trivial. In contrast, STM more readily resolves both the honeycomb lattice atomic structure of graphene and the nanometer-scale roughness (Figure 28).

We now consider the factors which contribute to the difficulty in obtaining high-resolution AFM measurements of the substrate as compared to STM. One physical explanation comes from consideration of the relevant length scales for AFM and STM based measurements. For STM measurements, topographic measurements are produced by establishing the tip position in sufficient proximity to the sample to produce a measurable tunneling current. This tunneling distance is typically within 1 Ångström of the surface. In contrast, the AFM measurement distance depends on the interaction force between the tip apex and the sample. For non-contact measurements the tip-sample distance for imaging occurs in the regime where van der Waals (vdW) forces dominate, assuming there are no additional magnetic or electrostatic forces influencing the measurement. A diagram of the key features of the force-distance relationship for AFM-based measurements, indicating both contact and non-contact regimes of operation, is shown in Figure 29. The non-contact regime typically extends over several nanometers, an order of magnitude greater range than

the STM tunneling range. Thus, it is possible to obtain AFM images while the tip is further from the sample relative to the ‘equivalent’ STM measurement, leading to reduced resolution for the AFM-based topography measurement.

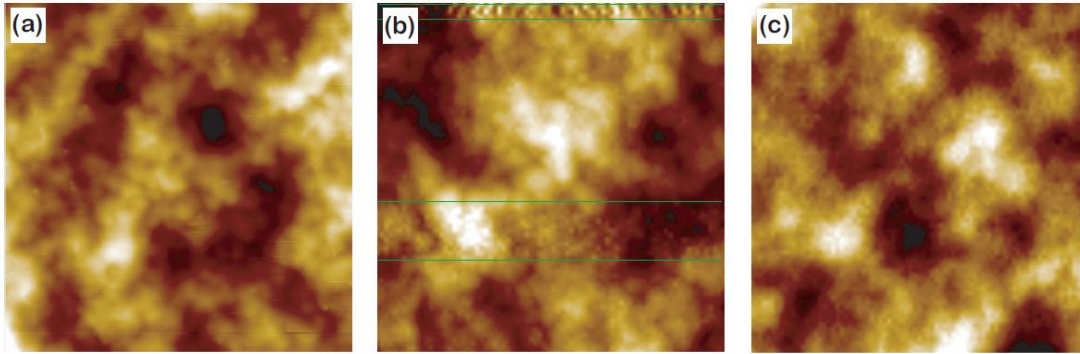


Figure 27: Topographic comparison of monolayer graphene/ SiO₂ measured with STM and NC-AFM. All three regions are 60 nm x 60 nm. (a) Graphene monolayer on SiO₂ measured by STM (-1.0 V, 47 pA). (b) Our highest-resolution measurement of graphene/SiO₂ by NC-AFM ($\Delta f = -10$ Hz, $A = 10$ nm). (b) has two horizontal bands which are dominated by feedback oscillations; these are marked by green lines. (c) Typical resolution obtained for graphene/SiO₂ by NC-AFM ($\Delta f = -10$ Hz, $A = 3$ nm). (a) is a complete 60 nm image sampled at 512 x 512 pixels; (b) and (c) are cropped from larger images at coarser sampling.

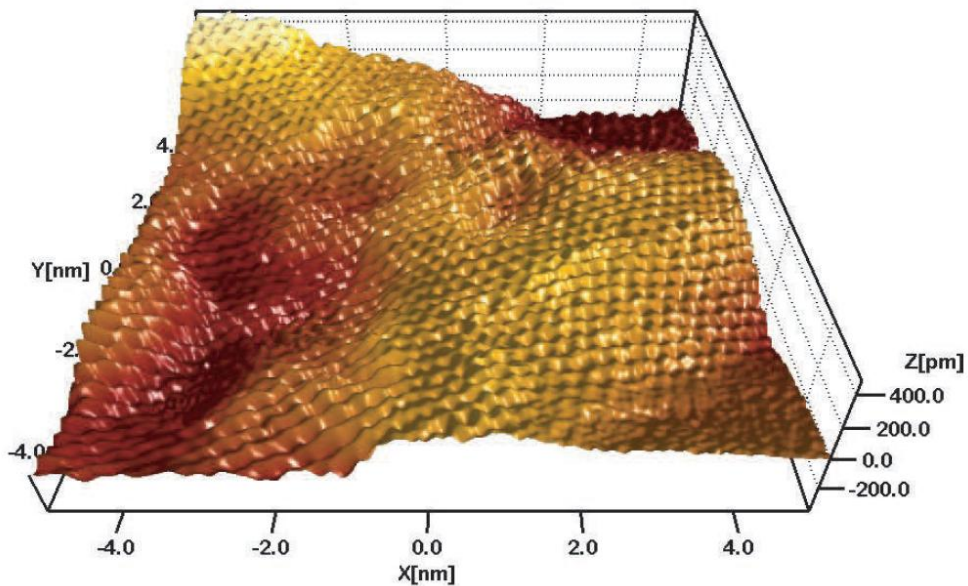


Figure 28: UHV STM image of SiO₂-supported mono-layer graphene. The honeycomb lattice is resolved, in addition to significant nanometer-scale roughness.

This simple argument about the relevant length scales for imaging in STM and AFM serves as a 0th order caution against comparing STM and AFM topographic images without additional experimental verification that the STM and AFM images are obtained with comparable resolution. Here, for example, AFM of both graphene and SiO₂ were obtained and resolution considerations discussed and quantitatively analyzed (Figure 26).

While the argument considering imaging distance for STM and AFM imaging techniques points to the unique challenge of obtaining high-resolution AFM images, it is incomplete. Comparing the imaging conditions required to obtain high-resolution of the SiO₂ substrate with those used previously for the under-resolved measurements, it is evident that both a small tip-apex radius and a UHV environment play a critical role in obtaining high-resolution, as discussed above. This is illustrated by the series of AFM measurements shown in Figure 30. Figure 30a shows a representative image of SiO₂ imaged in ambient with tapping-mode AFM. This image is representative of the best resolution I have been able to obtain using ambient AFM on this surface, and was taken using a standard silicon cantilever of nominal curvature radius < 10 nm, as specified by the manufacturer [117]. The rms roughness is ~ 0.23 nm, smooth compared to the rms roughness of 0.37 nm determined for the SiO₂ substrate with high-resolution UHV measurements. Similarly ‘smooth’ topography was obtained in [58], also in ambient tapping mode AFM, even though special tips with a tungsten spike of radius 1 nm at the apex [118] were used. Figure 30b shows an image obtained in UHV in NC-AFM mode, using a metal-coated cantilever of

nominal radius 20 - 30 nm. Figure 30c shows an image obtained in UHV NC-AFM, using a Veeco “super sharp” uncoated silicon cantilever of nominal radius 2 - 5 nm [116]. Note the significantly improved resolution of spatial features in this image. Comparing the images obtained with these super-sharp tips with those obtained with a metal-coated tip of nominal radius 30 nm demonstrates the distinct resolution improvement (Figure 30b,c). Features with radius of curvature as small as 2.3 nm were observed in images with the super-sharp tip (Figure 30d) [67]. Longer wavelength structure is seen in both high and low-resolution images. Based on the empirical evidence one may conclude that tip radius plays a crucial role in obtaining high-resolution NC-AFM measurements (this is well known in the scanned probe community and is consistent with the conclusions from the AFM resolution model presented in Chapter 4). Furthermore, given the previous under-resolved measurement [58] utilizing a sharp tip in ambient, one might also conclude that the cleanliness of UHV aids in high-resolution NC-AFM of surfaces (the value of UHV measurement is also well known in the scanned probe community).

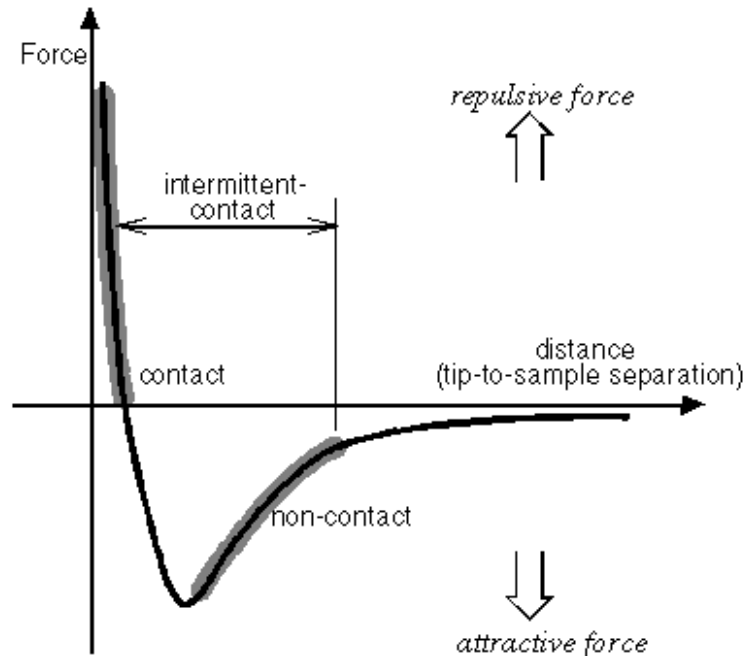


Figure 29: Schematic diagram of force-distance relationship for atomic force microscopy. Here the distance is the tip-sample distance. (diagram from Reference [119])

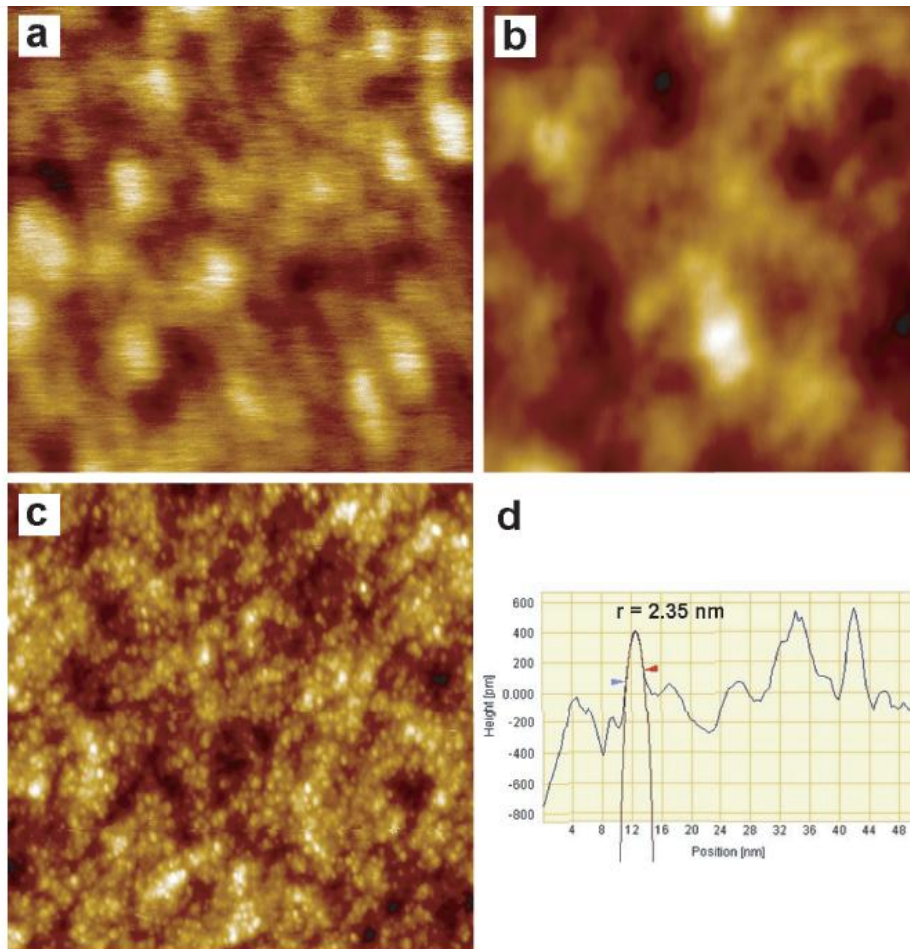


Figure 30: Images of SiO₂ at varying levels of spatial resolution. All images are 200 nm x 200 nm in size (a) ambient tapping-mode AFM image of SiO₂, obtained in am mode with conventional Si cantilever. (b) UHV FM-AFM image of SiO₂, obtained with metal-coated cantilever ($\Delta f = -150 \text{ Hz}$, $A = 1.0 \text{ nm}$). (c) UHV FM-AFM image of SiO₂, obtained with super-sharp silicon cantilever ($\Delta f = -150 \text{ Hz}$, $A = 1.0 \text{ nm}$). (d) line profile from image (c) with radius of curvature fit indicating curvature radius $\sim 2.3 \text{ nm}$.

5.3 Energetics of graphene interaction with the substrate

We now turn to a discussion of the energetics of bending and adhesion as a consideration of the physical origin of the apparently conformal adhesion between graphene and the underlying SiO₂ discussed in section 5.2. We first consider a simple analysis to provide an intuitive understanding of conformal adhesion. We then turn to a more sophisticated analysis adapted from membrane physics and compare the results of the measurements in section 5.2 with predictions of three different

theoretical models which use different parameterizations of the adhesion potential. The physical basis for these analyses is this: When the energy cost to bend graphene is *less* than the energy benefit from adhesion, one expects that graphene will follow the surface corrugation. Conversely, when the energy cost for bending is *greater* than the energy benefit from adhesion it is no longer energetically favorable for graphene to adhere conformally to the substrate. In order for graphene to adopt a structure more corrugated than the underlying substrate, it must pay energy costs against both curvature and adhesion.

5.3.1 Simple Analysis of the Energetics of Conformal Adhesion

By setting the adhesion energy γ equal to the bending energy, one can straightforwardly estimate the maximum curvature before the graphene “pops free” from the oxide substrate. The adhesion energy for graphene/SiO₂ may be deduced empirically from carbon nanotube experiments [120,121] and self-tensioning of suspended graphene resonators [122] to be ~ 0.625 eV/nm². The adhesion energy for graphite/SiO₂ has been calculated to be 0.5 eV/nm² [123].

The cost to bend graphene sheets [124–126] may be determined by considering the uniaxial bending energy/area: $E = C\kappa^2/2$ where κ is the curvature and $C = 0.85$ eV is the bending rigidity. Physically, this energy cost is determined by the distortion of C-C bonds with the bending-induced loss of planarity and the related strain. For this simple analysis to gain physical insight, we consider κ as the inverse of the radius of curvature in one dimension. Setting the bending and adhesion energy equal yields

$\frac{1}{\kappa} = R = 0.9$ nm, which represents the maximum curvature before graphene “pops

free” from the underlying SiO₂ substrate. For symmetric biaxial strain with $\kappa_x = \kappa_y$, $R = 1.3$ nm.

This simple analysis, which suggests that graphene will adhere to the rough morphology of the SiO₂ down to the limit of structural features with a radius of curvature on the order of $R_{\min} \sim 1$ nm, will be expanded more quantitatively below (and the basic insight will be shown to hold). Furthermore, even if the adhesion energy were an order of magnitude weaker, graphene would adhere to the rough substrate morphology down to features of 3 nm radius.

5.3.2 Membrane Physics and Parameterization of the Adhesion Energy

We now employ a more sophisticated quantitative analysis of the energetics of graphene adhesion adapted from membrane physics to gain additional insight into the relationship between graphene and substrate topography. Figure 31 shows a schematic of the graphene membrane and substrate geometry. We define $z_s(r)$ as the substrate height and $h(r)$ as the membrane height, both referenced to a flat reference plane. In this case, r is the spatial position in the x-y plane.

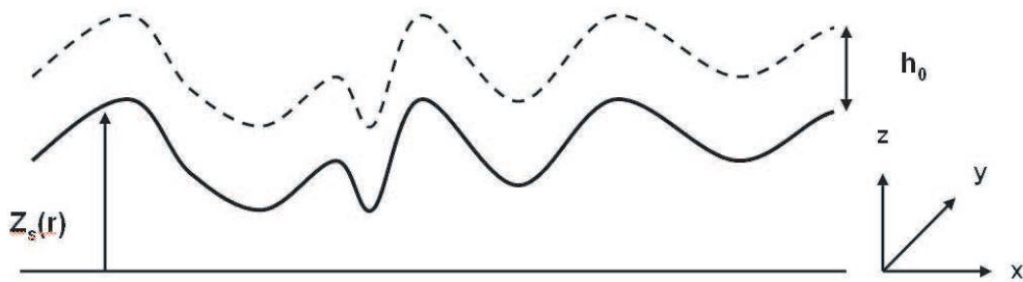


Figure 31: Schematic diagram of the geometry for membrane adhesion. $z_s(r)$ is the function for the substrate geometry (black solid line) while h_0 represents the distance between the substrate and graphene (black dashed line) which minimizes the adhesion potential. The vector r is in the x-y reference plane.

The general Hamiltonian describing membrane energetics is [127]:

$$H = \int \frac{C}{2} (\nabla^2 h(\mathbf{r}))^2 + \frac{\tau}{2} (\nabla h(\mathbf{r}))^2 + V[h(\mathbf{r}) - z_s(\mathbf{r})] d^2r \quad (21)$$

The three terms represent the energies of bending, tension, and adhesion, respectively. Here C is the elastic modulus, or bending rigidity, τ is the tension, and $V(z)$ is the substrate adhesion potential. $V(z)$ describes the adhesion energy as a function of distance normal to the substrate. Qualitatively, a curve with a well-defined minimum is expected, as shown in Figure 2 of Ref. [123]. The adhesion energy, $\gamma \sim 0.625 \text{ eV/nm}^2$ for graphene/SiO₂ [120–122], corresponds to the depth of the potential minimum. Without externally applied tension (as is the case for the membranes in this study), the Hamiltonian reduces to:

$$H = \int \frac{C}{2} (\nabla^2 h(\mathbf{r}))^2 + V[h(\mathbf{r}) - z_s(\mathbf{r})] d^2r \quad (22)$$

The membrane adhesion term requires some further discussion as several key assumptions are employed to simplify the analytical calculations. A useful approximation, known as the Deryagin approximation, is to assume the potential is a simple function of the local relative height between the substrate surface $z_s(r)$ and the membrane $h(r)$. It is also convenient to approximate the adhesion potential as a harmonic potential (the harmonic approximation), which is parameterized by the harmonic coefficient v (eV/nm⁴). Employing these approximations, the Hamiltonian becomes:

$$H = \int \frac{C}{2} (\nabla^2 h(\mathbf{r}))^2 + \frac{v}{2} [h(\mathbf{r}) - z_s(\mathbf{r})]^2 d^2r \quad (23)$$

We use the adhesion potential $V(z)$ to compute the harmonic coefficient, v :

$$v = \frac{\partial^2 V}{\partial z^2} \Big|_{z=h_0} \quad (24)$$

Since V is expressed as energy/area, the harmonic coefficient ν has units Energy/(length)⁴. It describes the cost of deviating from the minimum in the potential curve. One needs the potential curve in order to extract this coefficient, and Ref. [123] provides a computational result for graphite on silica (see Figure 2 in Ref. [123]). The potential is highly asymmetric in z , but can be approximated by a parabola for small excursions from the minimum. In Figure 32 we fit the points from Ref. [123] separately on both sides of the minimum. From these fits, the harmonic coefficient can be bounded between the values 76 eV/nm⁴ and 30 eV/nm⁴, depending on whether one takes the steep (repulsive) side of the potential (toward the substrate) or the shallower (attractive) side. The “depth” of the potential well is 0.5 eV/nm² (this corresponds to 80 mJ/m², the units expressed in Ref. [123]). Averaging these two estimates of ν yields the value 53 eV/nm⁴.

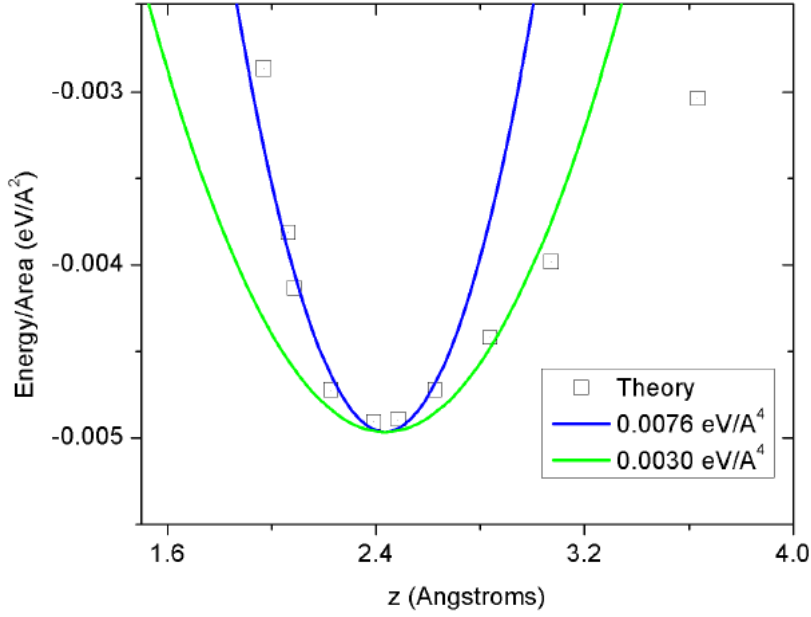


Figure 32: Quadratic fits to adhesion energy curve from Ref. [123], in the vicinity of the potential minimum. The blue curve is fit to the repulsive side while the green curve is fit to the attractive side.

Alternatively, one can arrive at this number by a more direct procedure, which emphasizes a useful scaling relation between these quantities. Following Aitken and Huang [107], one can begin with a Lennard-Jones potential written as:

$$W_{LJ}(r) = \frac{C_1}{r^6} + \frac{C_2}{r^{12}} \quad (25)$$

where it is assumed that the total energy is obtained pairwise over atoms in the substrate and graphene layer. For a flat monolayer and a flat substrate, the van der Waals potential becomes

$$U_{vdw}(z) = -\gamma \left[\frac{3}{2} \left(\frac{h_0}{z} \right)^3 - \frac{1}{2} \left(\frac{h_0}{z} \right)^9 \right] \quad (26)$$

by integration over the 3-dimensional semi-infinite substrate. For the substrate plus overlayer geometry, h_0 is the equilibrium separation distance and γ is the adhesion energy per unit area. By taking the second derivative with respect to z , one obtains the harmonic coefficient as:

$$\frac{d^2 U_{vdW}}{dz^2} = \frac{27\gamma}{h_0^2} \left[-\frac{2}{3} \left(\frac{h_0}{z} \right)^5 + \frac{5}{3} \left(\frac{h_0}{z} \right)^{11} \right] \quad (27)$$

We see that $\frac{d^2 U_{vdW}}{dz^2} \Big|_{z=h_0} = \frac{27\gamma}{h_0^2}$. In Ref. [123] they obtain $\gamma = 0.5 \text{ eV/nm}^2$ at equilibrium separation $h_0 = 0.492 \text{ nm}$, which yields $v \sim 56 \text{ eV/nm}^4$.

One should note that the harmonic approximation overestimates the energy cost of large excursions away from the substrate. Thus, it should be viewed as an approximation which is accurate for small fluctuations from the minimum in adhesion potential.

5.3.3 Energetics from membrane physics model

Having parameterized the adhesion, we may now utilize the theory from membrane physics to analyze and draw conclusions about the energetics of bending and adhesion for the images presented in section 5.2. First, we compute the elastic energy (or curvature energy E_C) per unit area as

$$E_C = \frac{C}{2} \left\{ \frac{1}{A} \int [\nabla^2 h(\mathbf{r})]^2 d^2 r \right\} \quad (28)$$

Here A is the area of the integration domain (statistical distributions of curvature are show in Figure 33). There are two cases of interest in this experimental study: (1) the curvature energy for graphene topography and (2) the curvature energy for the case of *perfectly* conformal adhesion (based on the substrate topography). These values can be obtained independently of any assumption about the adhesion energy, but their *difference* provides a value for the cost of curvature against adhesion. For these calculations, we assume C is bounded within 0.8-1.4eV. For the graphene topography corresponding to Figure 24a in section 5.2, the quantity in brackets for Equation (28) evaluates to 0.078 nm^{-2} and we obtain $E_{C,\text{graphene}} = 0.031\text{-}0.055 \text{ eV/nm}^2$. For the SiO₂ topography shown in Figure 24b the quantity in brackets evaluates to 0.23 nm^{-2} and we obtain $E_{C,\text{conformal}} = 0.092\text{-}0.161 \text{ eV/nm}^2$. The average difference between these two values is 0.084 eV/nm^2 and represents the energy cost of curvature against the adhesion potential for the experimentally measured graphene/SiO₂.

Employing the parameterizations and approximations developed for the adhesion potential in section 5.3.3, we find that the energy cost (per unit area) of deviating from the minimum in the adhesion potential (occurring at h_0) is given by:

$$\delta E_A = \frac{v}{2} \left\{ \frac{1}{A} \int [h(\mathbf{r}) - z_s(\mathbf{r})]^2 \right\} d^2 r \quad (29)$$

Defining $\Delta(\mathbf{r}) = h(\mathbf{r}) - z_s(\mathbf{r})$, note that the quantity in brackets is equivalent to the variance of $\Delta(\mathbf{r})$:

$$\delta E_A = \frac{v}{2} \left\{ \frac{1}{A} \int [h(\mathbf{r}) - z_s(\mathbf{r})]^2 \right\} d^2 r = \frac{1}{2} v \sigma_\Delta^2 \quad (30)$$

where σ_{Δ}^2 is given in terms of $h(\mathbf{r})$ and $z_s(\mathbf{r})$ as:

$$\sigma_{\Delta}^2 = \sigma_h^2 + \sigma_{z_s}^2 - 2[\langle h z_s \rangle - \langle h \rangle \langle z_s \rangle] \quad (31)$$

The final term may be removed by setting either $\langle h \rangle$ or $\langle z_s \rangle = 0$:

$$\sigma_{\Delta}^2 = \sigma_h^2 + \sigma_{z_s}^2 - 2\langle h z_s \rangle \quad (32)$$

Since the experiments do not allow for imaging of the substrate corrugation directly beneath the graphene, the formulation in terms of the variance is key to drawing physically meaningful insight from this particular approach to the energetics analysis. This expression make clear that the variance in $\Delta(\mathbf{r})$ depends crucially on the degree of correlation between h and z_s . While the correlation is not directly measured in the scanned-probe experiment, in order to gain intuition we consider two limits.

Firstly, in the limit of perfect adhesion, the variances for the graphene σ_h^2 and the substrate $\sigma_{z_s}^2$ cancel with $2\langle h z_s \rangle$, resulting in $\sigma_{\Delta}^2 = 0$. Thus there is no deviation from the minimum in the adhesion potential. This result should be expected as perfect conformation should occur with graphene at the adhesion potential minimum distance ($\Delta(\mathbf{r})$ becomes a constant, h_0). One obtains the full adhesion energy (the complete depth of the potential well) in this case. By contrast in the uncorrelated limit, $\langle h z_s \rangle = 0$, the variance (σ_{Δ}^2) will be large because there is no cancellation.

While the harmonic approximation is only valid for small excursion from the potential minimum, the approximation can nonetheless be instructive for understanding the magnitude of the variance in the cases of adhesion and de-adhesion, as in the argument presented above. Setting the energy cost of deviating

from the minimum the minimum in the adhesion energy for graphene/SiO₂ (estimated from References [120–122]) gives an extreme limit for de-adhesion. $\frac{1}{2} \nu \sigma_{\Delta}^2 = 0.6 \text{ eV/nm}^2$ occurs for $\sigma_{\Delta} = 0.146 \text{ nm}$ (throughout this analysis $\nu = 56 \text{ eV/nm}^4$, as described above). This corresponds to an amplitude of $\sim 0.21 \text{ nm}$ (converting rms to peak amplitude) and indicates that graphene with a mean amplitude of 0.21 nm , which is uncorrelated with the substrate, would be essentially de-adhered from the substrate. This demonstrates the high energy cost for graphene to adopt significant structure independent of the substrate structure. For graphene to exhibit any significant “intrinsic rippling”, the energetic calculation here suggests that the graphene would adhere extremely weakly (with 0.21 nm as an amplitude limit for adhesion). This is hard to reconcile with the known adhesion properties of graphene and carbon nanotubes on SiO₂.

In contrast, turning to the data in section 5.2, we find that the energy balance is satisfied by high conformal adhesion. The calculated cost of bending against adhesion (0.084 eV/nm^2) gives $\sigma_{\Delta}^2 = 0.003 \text{ nm}^2$, again using Equation(32). A small positive value of σ_{Δ}^2 is consistent with high (positive) correlation between h and z_s . The ratio $\frac{\langle h z_s \rangle}{\sigma_h \sigma_{z_s}} = 0.99$, indicating an extremely high degree of correlation between the graphene and the underlying substrate. Although the harmonic approximation overestimates the adhesion, the analysis suggests that graphene topographic features are the result of topographic features in the underlying substrate. In the next section, several analyses of the energetics problem are presented which do not rely on the

harmonic approximation. These theories similarly lead to the conclusion that graphene topography is determined by substrate topography.

5.3.4 Energetics from Other Recent Theories

This section discusses the experimental results from section 5.2 in the context of recent theories. For an adhesion energy near 0.5–0.6 eV/nm² and bending rigidity 1.4–1.5 eV, these unambiguously predict highly conformal adhesion [107,114,115]. In Ref. [107], the graphene-SiO₂ adhesion potential is described analytically by a Lennard-Jones pair potential, while in Ref. [114] a similar pair potential is used but with Monte Carlo integration over substrate atoms. Both are parametrized in terms of the ratio A_s/λ , with the substrate modeled as a single-frequency sinusoidal corrugation with amplitude A_s and wavelength λ . The SiO₂ topography exhibits power-law scaling with a correlation length ~ 10 nm; associating the full $\sigma_{rms} = 0.37$ nm with $\lambda \sim 10$ nm, we obtain $A_s/\lambda \sim 1/20$. The adhesion transitions predicted in Refs. [107,114] occur only in the limit of much larger A_s/λ or much weaker adhesion, and both predict high conformation, with ratio $A_g/A_s > 0.9$ [A_g is the sinusoidal amplitude of graphene (g)]. From our σ_{rms} values, $A_g/A_s = 0.95$.

Conformal graphene adhesion is further predicted by Ref. [115]; it is shown that for a periodic sinusoidal substrate profile, de-adhesion will occur in a series of transitions where first the membrane breaks loose from every other trough, then every two out of three troughs, and so on. In the zero-tension limit, these transitions are governed solely by the dimensionless parameter α where $\alpha = (\kappa_{eq}/\kappa_s)^{1/2}$. Here, $\kappa_{eq} =$

$(2\gamma/C)^{1/2}$ with adhesion energy γ and bending rigidity C as above. κ_s is the geometrical curvature of the substrate. A perfectly conforming ground state is predicted for $\alpha \geq 0.86$. Making conservative estimates $\gamma = 0.5 \text{ eV/nm}^2$ and $C = 1.4 \text{ eV}$, the transition from perfect conformation occurs at substrate curvature $\kappa_s = 1.14 \text{ nm}^{-1}$. Figure 33 shows a histogram of surface curvature obtained from high-resolution NC-AFM measurement of SiO_2 , where it is apparent less than 0.1% of the surface has curvature exceeding 1.0 nm^{-1} .

5.3.5 Summary and Conclusion

The preceding arguments have demonstrated that highly conformal adhesion to the SiO_2 substrate accounts for the observed graphene topography. This is primarily because the curvature energy scale set by the corrugation of SiO_2 is modest compared to that of the adhesion potential. “Intrinsic” rippling of graphene on SiO_2 is physically unrealistic due to the overwhelming energy cost of deviating from the local minimum in $V(z)$. Rather, previous measurements which concluded “intrinsic” rippling for graphene on SiO_2 did not resolve to finest structural details of the surface using AFM [58].

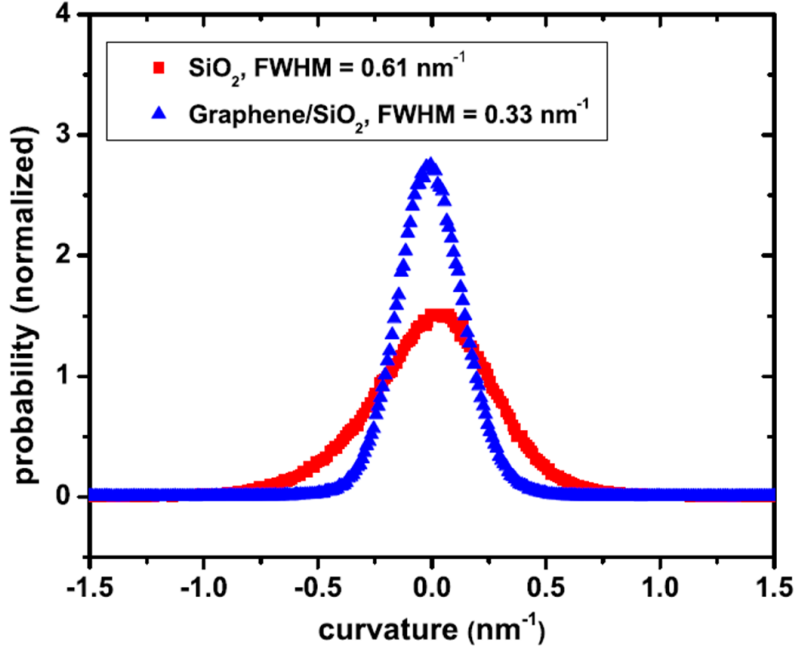


Figure 33: Curvature histograms, normalized to unit area, for graphene (narrower distribution) and SiO₂ (broader distribution)

5.4 Potential from corrugation

Corrugations in the graphene sheet are expected to serve as a scattering mechanism for graphene transport, as discussed in Chapter 1. These corrugations may generate an inhomogeneous electrochemical potential on the graphene membrane. E. A. Kim and A. Castro Neto developed a relationship between the graphene potential and the local mean curvature [46]:

$$\Phi(r) = -\alpha \frac{3a^2}{4} (\nabla^2 h)^2 \quad (33)$$

Here $\alpha = 9.23$ eV and $a = 0.142$, the graphene lattice constant, and $\nabla^2 h$ gives the local mean curvature. It should be noted that this formulation does not account for the screening in graphene and therefore overestimates the potential in graphene due to corrugations. Rather, it is best compared to an unscreened substrate potential. Figure

34 shows the potential calculated from an STM image of graphene corrugation using equation (33). Due to the drift consideration, the Laplacian of the height distribution is considered one-dimensionally as $\partial^2 h / \partial x^2$ (eg along the fast scan direction). The resulting potential variation is on the order of meV. The magnitude of the potential autocorrelation function $C(r)$ resulting from the corrugation induced potential is comparable to the $C(r)$ for bare SiO₂ at very small r , but drops off much more rapidly with r , i.e. the correlations of the corrugation-induced potential are short ranged (Figure 35). Short-ranged correlated potentials give rise to a resistivity in graphene independent of carrier density, hence the low-carrier density resistivity in graphene will always be dominated by long-range correlated potentials such as the $C(r)$ due to SiO₂ charges. Therefore corrugation cannot account for the observed scattering (and corresponding mobility limits) in graphene devices on SiO₂.

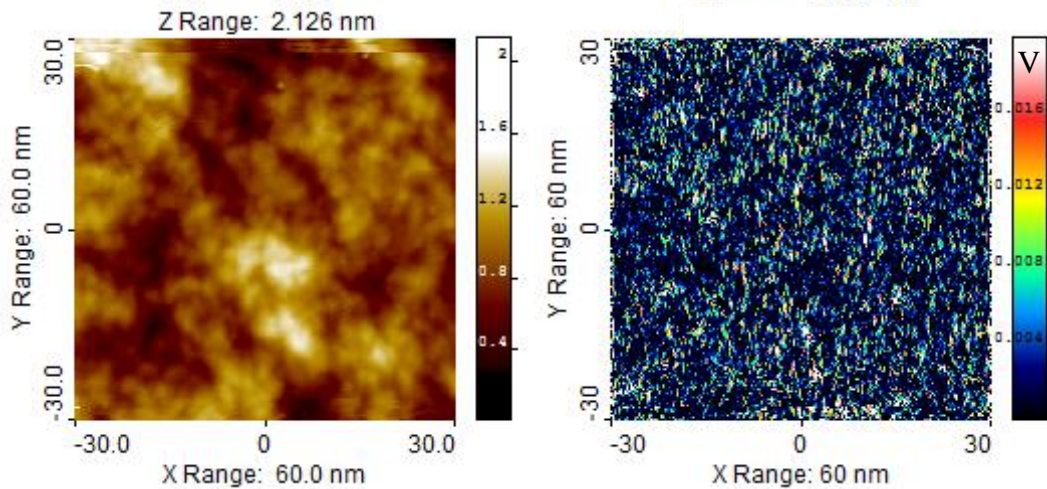


Figure 34: STM of graphene topography (left) and the calculated potential resulting from this topography (right) based on equation (33). Note that the large z range is indicative of noi

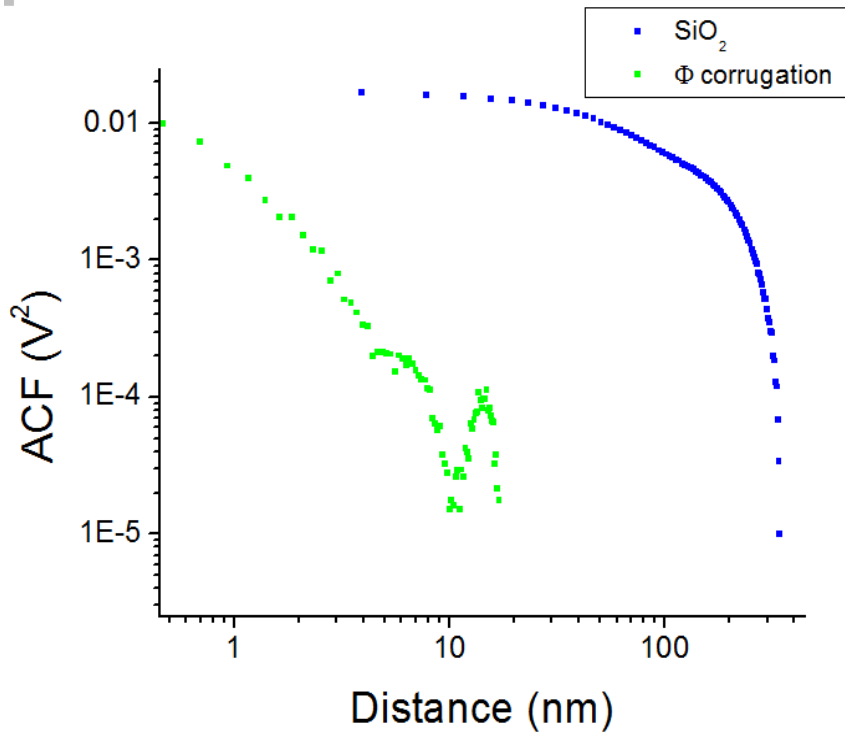


Figure 35: Potential autocorrelation function from calculated potentials from equation (33) due to graphene corrugation (green). Images used were 60 nm x 60 nm. Potential autocorrelation functions from 1 μm x 1 μm Kelvin probe images of BN and SiO₂ are shown for comparison (orange and blue, respectively)

5.7 Conclusions and Summary

This chapter covered the relationship between graphene corrugation and substrate corrugation. The chapter shows that (1) graphene follows the substrate corrugation with high fidelity and that (2) this is because the adhesion energy between graphene and SiO₂ dominates the energetics of the problem. The chapter also discusses the experimental observation that high resolution images in AFM of corrugated surfaces can be more difficult to obtain, in part because the vdW interaction between the tip and side walls of the corrugation can lead to attenuation of surface features (as discussed in graphene detail in Chapter 4). In conclusion, *the substrate corrugation determines the graphene corrugation* (not “intrinsic” rippling) as revealed by high-

resolution measurements. This is a promising result for applications in strain engineering.

Chapter 6: Charged Impurities in Graphene Substrates

Scattering charges:

Electronic transport foe

Makes rainbow puddles

This chapter addresses the question of charged impurities in graphene substrates. I begin with a review of previous scanned probe experiments on graphene and follow with a study of charged impurities in graphene substrates. In this study, Kelvin probe microscopy in ultra-high vacuum is used to image the local electrostatic potential fluctuations above hexagonal boron nitride (h-BN) and SiO₂, common substrates for graphene. Results are compared to a model of randomly distributed charges in a two-dimensional (2D) plane. For SiO₂, the results are well modeled by 2D charge densities ranging from 0.24 to $2.7 \times 10^{11} \text{ cm}^{-2}$, while h-BN displays potential fluctuations 1-2 orders of magnitude lower than SiO₂, consistent with the improvement in charge carrier mobility for graphene on h-BN compared to SiO₂. Additionally, the effects of common fabrication procedures are considered. Electron beam exposure of SiO₂ increases the charge density fluctuations, creating long-lived metastable charge populations of $\sim 2 \times 10^{11} \text{ cm}^{-2}$ at room temperature, which can be reversed by heating. The chapter is largely based on Reference [69].

6.1 Introduction to Scanning Probe Experiments on Graphene

Scanning probe measurement have played a key role in understanding the nature of charge puddles in graphene. The earliest efforts to measure the charge fluctuations in graphene and the underlying SiO₂ substrate were performed by the Yacoby group [44]. They used a scanning single electron transistor (SET) to measure the inverse compressibility (inverse of the density of states) above the graphene. The scanning SET technique [128,129] has high charge sensitivity, down to a fraction of an electron, but the spatial resolution is significantly limited by the size of the probe (~100 nm) and the distance between the probe and the sample. Figure 36 shows the spatial density variations in the graphene flake extracted from measurements of inverse compressibility; a histogram of this data is used to quantify the average density fluctuations. From the standard deviation of a fit with a Gaussian distribution they determine average density fluctuations of order $n_{rms} = \pm 3.9 \times 10^{10} \text{ cm}^{-2}$. The intrinsic density fluctuations, $n_{rms} = \pm 2.3 \times 10^{11} \text{ cm}^{-2}$, are obtained independently from transport measurements at 11 T magnetic field by determining the width of the incompressible band with a Gaussian fit (shown in Figure 37). Additionally, the work determines a puddle size of 30 nm by considering the ratio of the average density fluctuations and the intrinsic density fluctuations.

For the measurements above the bare SiO₂ (Figure 36b), they report a potential variance of 50 mV. Based an analysis of the variance and the assumption that the induced charge fluctuations on the SET are similar what would be induced in

graphene if present, they propose $2 \times 10^9 \text{ cm}^{-2}$ as an upper limit for the density fluctuations in graphene due to surface or trapped charges in the oxide and conclude that the charge fluctuations in the underlying SiO_2 substrate cannot account for the charge fluctuations in graphene. However, it should be noted that variance of the substrate potential, on which the analysis is based, does not adequately account for the charge impurity density in the substrate as will be addressed later in the chapter..

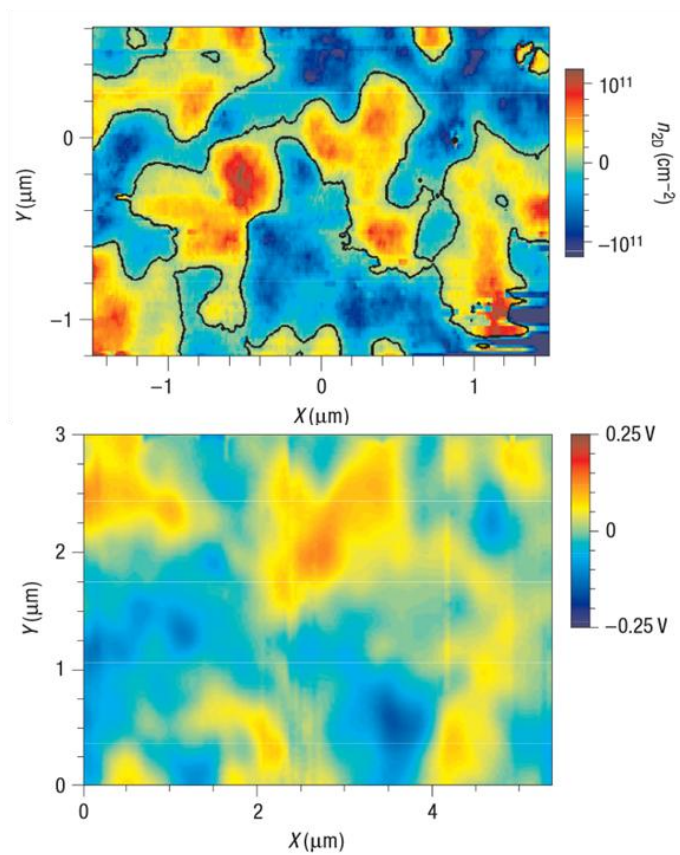


Figure 36: (a) Color map of surface density fluctuations in a monolayer graphene sheet on SiO_2 extracted from potential measurements with a scanning single electron transistor. Blue regions correspond to hole-rich regions while red regions correspond to electron-rich regions. (b) Potential fluctuations above the bare SiO_2 substrate. (from reference [44])

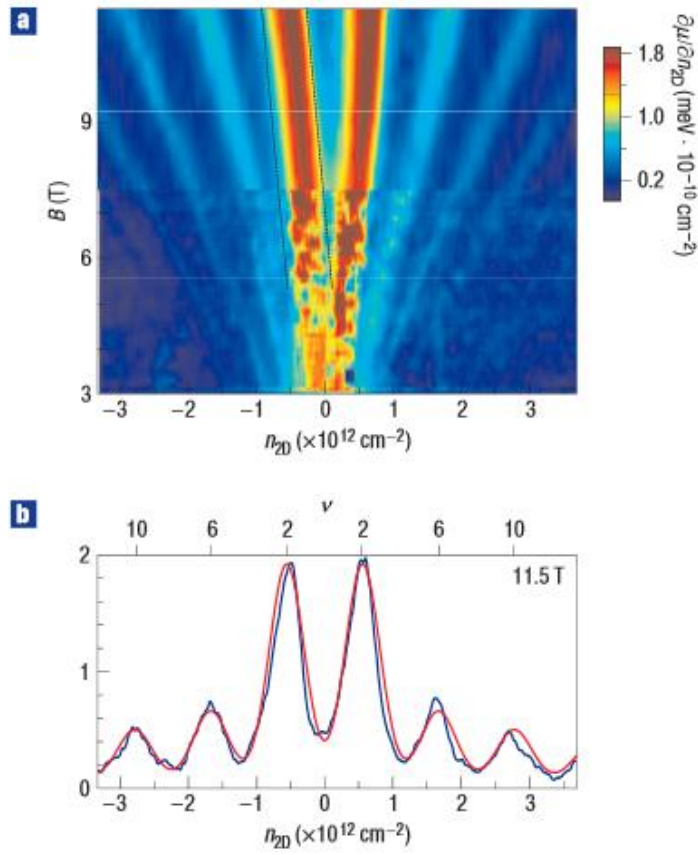


Figure 37: (a) Inverse compressibility as a function of the density and magnetic field. (b) A line scan from plot a at 11 T (blue) and fit to data with Gaussians of equal variance. (from [44])

Since the initial SET measurement, scanning tunneling microscopy (STM) and scanning tunneling spectroscopy (STS) experiments have been conducted by several groups [40–43]. These measurements offered improved spatial resolution over the SET measurements and simultaneously probed both the topographic landscape and electronic disorder in graphene. Yet, unlike the SET measurements, these measurements are limited to an exploration of graphene without direct consideration of the underlying substrate (which cannot be probed with STM since it is not conducting). Nonetheless the STM and STS experiments provide insight into the

importance of understanding the graphene-substrate interaction to account for the observations of graphene topography and potential.

Figure 38 shows topography and dI/dV mapping (proportional to variations in the electronic local density of states) for graphene on SiO_2 [40,43]. The topographic image Figure 38a has roughness $\sigma_{\text{rms}} \sim 1.5 \text{ \AA}$ [40]. It had been suggested that ‘intrinsic ripples’ or corrugation resulting from the underlying substrate in graphene may produce local variation in the electrochemical potential leading to electron and hole puddles [43,46]. The electron-hole puddles in graphene are shown in Figure 38b; these maps reveal that the electron hole puddles in graphene on SiO_2 have a characteristic length of $\sim 20 \text{ nm}$ and that the charge carrier fluctuations within the graphene are on the order of $n_{\text{rms}} \sim 4 \times 10^{11} \text{ cm}^{-2}$. Based on the measurements, both the groups concluded that the topographic roughness of the graphene sheet could not account for the observed electron-hole puddles within the graphene sheet; the simultaneous images showed no apparent correlation between the two features. Instead, random-charged impurities present on or beneath the graphene sheet are credited for the observed potential fluctuations. Table 1 shows the results for the charge carrier fluctuations determined from existing scanned probe measurements of graphene on SiO_2 and h-BN (discussed below). The values for substrate charged impurity density that would lead to these charge fluctuations are extracted using a self-consistent theory [38] and tabulated in the final column. Here, $n_{\text{rms}} = \sqrt{3}n^*$. Each experiment probed only a small area (a few correlation lengths) of the substrate, so the precision of these numbers should be assumed to be low. However, it is notable

that a comparable order of magnitude for n_{imp} in the SiO₂ is concluded from three independent measurements.

Table 1: Summary of the graphene charge fluctuations and extracted substrate impurity densities from scanned probe studies of graphene. The calculated n_{imp} values are extract using the self consistent theory presented in section 1.4.

Author (PI) and Reference		Substrate	Measured n_{rms} (1/cm ²)	Calculated n_{imp} (1/cm ²)
Yacoby, Ref. [44]	2007	SiO ₂	2.3×10^{11}	3.6×10^{11}
Crommie, Ref. [41]	2011	SiO ₂	8.2×10^{10}	9.9×10^{10}
LeRoy, Ref. [42]	2011	SiO ₂	2.64×10^{11}	4.3×10^{11}
Crommie, Ref. [41]	2011	h-BN	2.3×10^{10}	2.1×10^{10}
LeRoy, Ref. [42]	2011	h-BN	2.5×10^9	1.6×10^9

Further studies of graphene on h-BN substrates reveal improvements over SiO₂. h-BN is a wide-bandgap insulator (5.97 eV) with a 1.7% lattice mismatch with graphene and has the advantages of being atomically flat and more chemically inert than SiO₂. Again, STM and STS were employed to establish topographic images of graphene on h-BN along with electron hole puddles, shown in Figure 39. From the data analysis, graphene on h-BN is an order of magnitude smoother than SiO₂ (for h-BN $\sigma_{rms} \sim 0.1-0.3 \text{ \AA}$, for SiO₂ $\sigma_{rms} \sim 2 \text{ \AA}$) and exhibits electron-hole charge fluctuations in the graphene reduced 1-2 orders of magnitude from graphene/SiO₂ ($\Delta n_{h-BN} \sim 10^9 - 10^{10} \text{ cm}^{-2}$; see Table 1). These improvements are expected to account for the observed improvement in mobility for graphene/h-BN devices over graphene/SiO₂ devices.

However, the work from Yacoby's group discussed above represents the only attempt of which I am aware to characterize the charge disorder in graphene as well as the bare SiO₂ substrate and they concluded that charge variation in the substrate could not

account for that observed in the graphene [44]. Attempts to resolve the issue through transport experiments alone have been controversial, for instance measurements of the dependence of graphene's conductivity on the dielectric constant of the environment [29,31,32], and the ratio of the momentum scattering time to quantum scattering time [33,35] have produced conflicting results. The phenomenological observation of higher mobility for graphene suspended or on h-BN compared to SiO₂ is not conclusive since there could be a number of competing effects such as charged impurities in SiO₂, chemical hybridization of graphene with dangling bonds in SiO₂ which could lead to resonant scatterers [130], or corrugations of graphene on rough SiO₂ [66].

Motivated by these previous scanned probe experiments, by the link between charged impurities and graphene mobility [30] (discussed in chapter 1), and by the observed improvement in mobility for graphene on BN over graphene on SiO₂ [25] (also discussed in chapter 1), I undertook a Kelvin probe microscopy study of graphene substrates SiO₂ and h-BN.

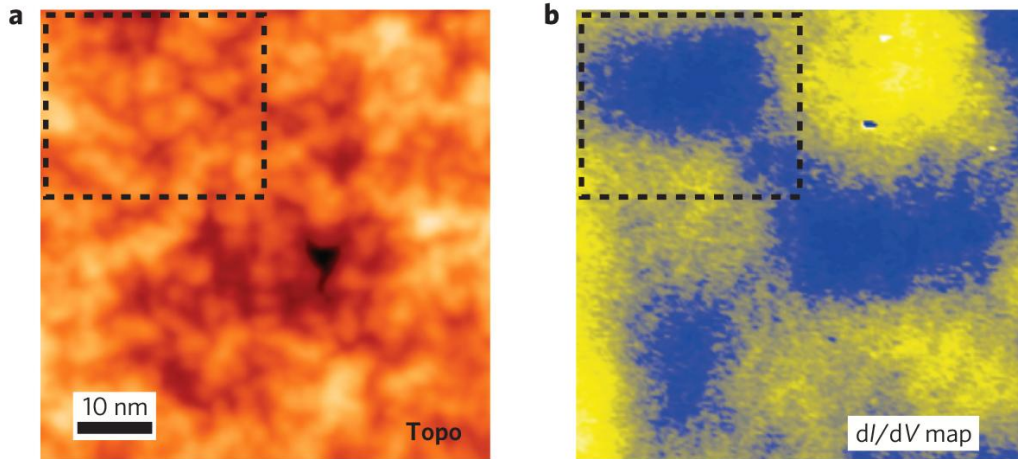


Figure 38: (a) 60x60nm STM image of graphene corrugation on SiO₂ and (b) dI/dV map obtained simultaneously displaying electron-hole puddles within the graphene sheet with characteristic length ~20nm (from Reference [40])

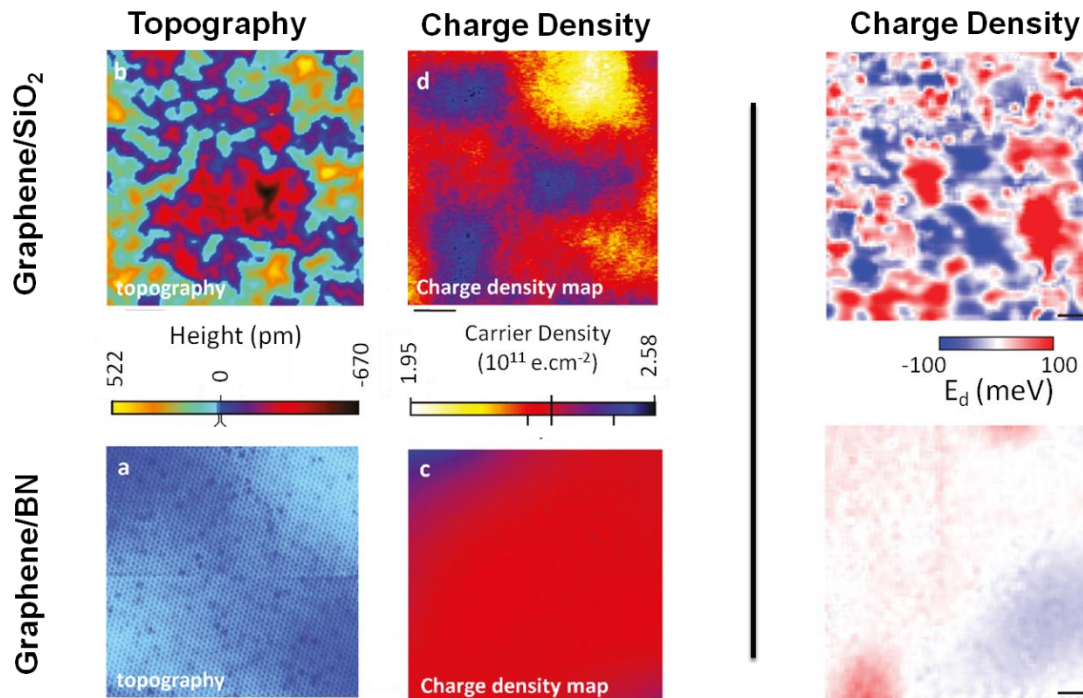


Figure 39: Topography and dI/dV mapping for graphene on SiO₂ and graphene on BN (adapted from References [41] and [42])

6.2 Kelvin Probe of Graphene Substrates

In this section, Kelvin probe force microscopy is used to directly measure the potential disorder in two common substrates used for graphene devices, amorphous SiO₂ and h-BN, to provide an insight into charge inhomogeneity in these substrates. I analyze the autocorrelation function of the local potential distribution for distinct SiO₂ samples and find it is well-described by a two-dimensional (2D) random distribution of charges at the surface, allowing us to determine the surface trapped charge density in a given sample to within a few percent. I find a significant variation of the magnitude of the trapped charge density between similarly prepared samples, with values ranging from 0.24 - 2.7 x 10¹¹ cm⁻², suggesting an uncontrolled environmental effect on the trapped charge density at the SiO₂ surface. Samples of h-BN on SiO₂ showed similar variation and were less well modeled by randomly distributed charges in a 2D plane. However h-BN on SiO₂ samples all showed significantly lower surface potential fluctuations than the cleanest SiO₂ samples supporting the hypothesis that lower surface potential fluctuations are related to the higher mobility in graphene on h-BN compared to SiO₂. In an attempt to understand the sample-to-sample variations in trapped charge density, the effect of device fabrication conditions is also addressed; in particular it is shown that even small electron beam dosing can produce large (~2 x 10¹¹ cm⁻²) metastable trapped charge densities on SiO₂, and smaller charge densities on h-BN, and that annealing can reverse the effect of electron beam exposure. I propose that the metastable trapped charge after electron beam exposure reveals the density of deep traps at the SiO₂

surface, and these traps are responsible for the low charge carrier mobility observed in graphene on SiO₂. It is expected that the technique and analysis methods will be useful to assess the quality of other candidate substrates for graphene and other self-assembled electronic materials.

The substrates used in this work were fabricated as follows. Amorphous SiO₂ (300 nm) was grown on Si by dry thermal oxidation. Samples from two sources were examined which are nominally identical to those used in Refs. [15] and [18]. Si/SiO₂ (300nm) samples were cleaved in ambient conditions and subsequently subjected to a moderate temperature chamber bake at 130°C in vacuum (10⁻¹⁰ Torr). In order to best match the sample fabrication conditions for much of the exfoliated graphene/SiO₂/Si transport literature (often mechanically exfoliated in ambient conditions) [131], [6], no additional cleaning was performed prior to imaging. h-BN was exfoliated from single crystals onto SiO₂ as described in Reference [25]. Simultaneous non-contact atomic force microscopy (NC-AFM) and Kelvin probe force microscopy (KPFM) were obtained as described in chapter 3. A Pt-coated Si cantilever with a nominal radius of curvature $r_{\text{tip}} = 30$ nm (nominal spring constant $k = 40$ N/m) was utilized. Scans are typically 1 μm^2 and 256 x 256 pixels and are taken at slow speeds (~2 hr/scan). Subsequent scans from the same location exhibit a high degree of consistency in the potential distribution and indicate minimal drift in the Kelvin signal, within the resolution limits of the instrument (on the order of 1-2 mV/hour).

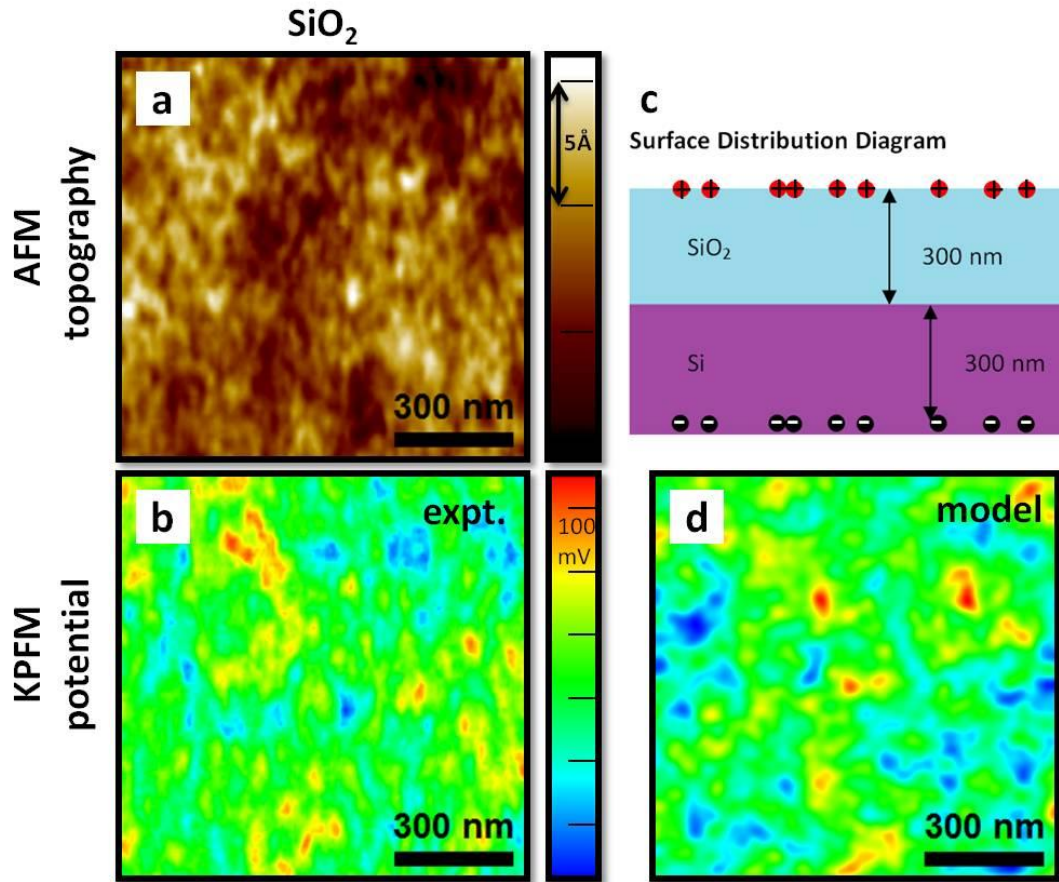


Figure 40: (a) Topography and (b) relative potential for the bare SiO₂/Si substrate. (c) Model of the expected charge distribution. (d) Potential for a simulated charge distribution (parameters are charge density $n_{\text{imp}} = 2.5 \times 10^{11} \text{ cm}^{-2}$, distance of tip to charges $d = 1 \text{ nm}$, oxide thickness $d_{\text{ox}} = 300 \text{ nm}$). Color scale in (d) is same as (b) with full range of 630mV.

Figure 40 shows the topography and surface potential of a typical SiO₂/Si substrate (frequency shift $\Delta f = -100 \text{ Hz}$, amplitude $A = 5.0 \text{ nm}$). The topographic variations (Figure 40a) are consistent with those reported elsewhere, though the spatial resolution of the metal-coated AFM tip is insufficient to resolve the finest features. [66] Figure 40b shows the surface potential of the same area in Figure 40a. The surface potential shows variations which are not explicitly correlated with the topography (Figure 40a). In order to explain the observed random potential variation, we develop a model for the surface potential as follows. I first assume that the

charges are primarily at the surface of the SiO₂ substrate, hence I use a two-dimensional random distribution of charges of density n_{imp} to model the expected potential distribution. I then assume that the tip measures the potential in a plane at a fixed distance d above the sample. Because of the presence of the highly-conducting silicon ground plane a distance $d_{\text{ox}} = 300$ nm below the SiO₂ surface, the potential of a given charge is the sum of its Coulomb potential and that of its image, located $2d_{\text{ox}} = 600$ nm below the charge. Figure 40c shows this schematically. I treat the charges as embedded in a uniform half-plane of effective dielectric constant $\epsilon_r = (1 + \epsilon_{\text{SiO}_2})/2 \approx 2.45$ where $\epsilon_{\text{SiO}_2} = 3.9$ is the dielectric constant of SiO₂; this gives an exact result for the potential in the plane of the charges at the interface of SiO₂ and vacuum, and is an excellent approximation for our geometry. Figure 40d shows the potential obtained from the model using $n_{\text{imp}} = 2.5 \times 10^{11} \text{ cm}^{-2}$ and $d = 1$ nm. The potential is convoluted with a Gaussian of FWHM $= r_{\text{tip}} = 30$ nm to account for broadening due to the finite tip size. Although a full understanding of Kelvin probe imaging of semi-conducting surfaces requires more complex models of the tip [132–135], this simple Gaussian convolution approach nonetheless provides a valuable qualitative result. The model potential shows very similar variation in magnitude and spatial dimension to the experimentally obtained potential map (Figure 40c). These images are shown with the same potential scale for ready comparison. While this simulation provides a useful qualitative comparison, a more detailed quantitative comparison of the statistical properties of the simulated and experimental potentials is made below.

Previous analysis of the surface potential of SiO₂ examined the variance of the potential. [44] However, because the potential of a Coulomb impurity diverges at small distances as $\frac{1}{r}$, the experimentally observed variance of the potential depends critically on the cut-off length scales in the experimental measurement (i.e. d and r_{tip} discussed above), which can remove the divergence of the impurity potential. In the previous scanning single electron transistor measurement [44], d and r_{tip} were not explicitly known, but they were estimated to exceed 100 nm (comparable to d_{ox}). In this experiment, I quantitatively analyze the full 2D autocorrelation function of the potential $C(r)$, which gives the similarity of potential measurements as a function of the spatial separation r , rather than only the variance (equal to the value of the autocorrelation function at $r = 0$, $C(0)$). I fit the full $C(r)$ to a model of random charges in a 2D plane, allowing us to estimate the charge density n_{imp} and tip-charge distance d . Furthermore, the higher spatial resolution in the measurement allows me to probe $C(r)$ at distances $d, r_{\text{tip}} \ll r \ll d_{\text{ox}}$ where $C(r)$ depends overwhelmingly on the density of charges n_{imp} and is insensitive to the magnitude of d, r_{tip} . This limit thus provides a reliable experimental methodology to estimate n_{imp} .

An analytical form of the $C(r)$ for an infinite, 2D random distribution of point charges has been utilized previously to describe disorder in graphene [39,136,137] and semiconductor heterojunctions [138,139]. For uncorrelated charges the multi-charge $C(r)$ will be simply the product of the single point charge autocorrelation function $C_p(r)$ and the total number of charges N_{imp} : $C(r) = N_{\text{imp}}C_p(r)$. To account for the finite size limitations and sampling resolution of the experimentally obtained data, I find

$C_p(r)$ numerically starting from a potential grid with same size and sampling resolution as the experimentally obtained images using the dipole potential of the charge and its image in the Si ground plane. Finally, to account for signal broadening due to the finite size of the tip, I convolve $C(r)$ with a Gaussian with a FWHM = $r_{\text{tip}} = 30$ nm. N_{imp} and d are extracted as fitting parameters from the least squares fit. Dividing N_{imp} by the image area gives the charged impurity density, n_{imp} .

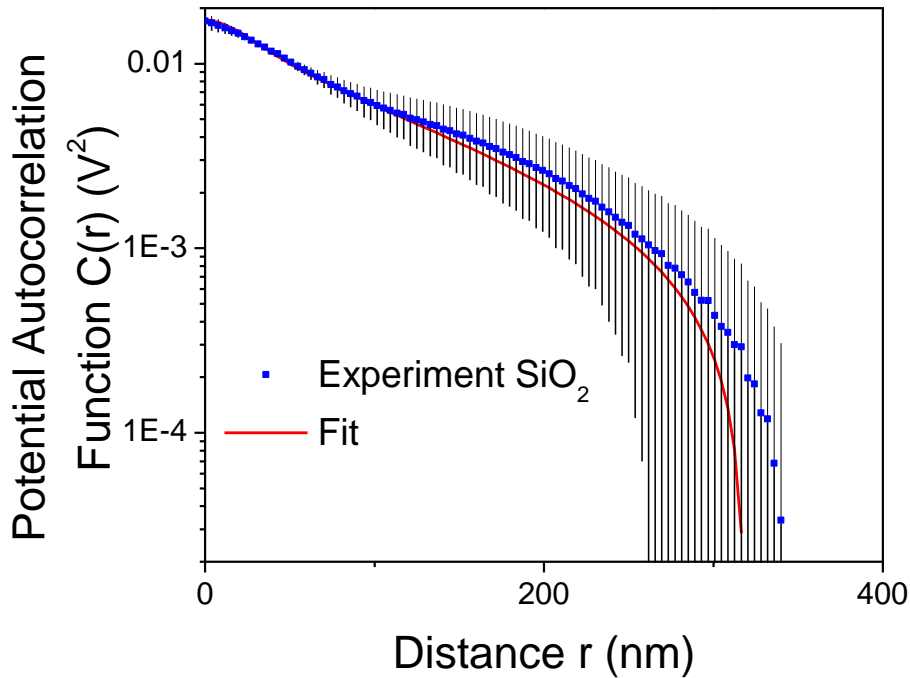


Figure 41: Autocorrelation function from experiment (blue squares, average from 3 images) and best theoretical fit ($n_{\text{imp}} = 2.7 \times 10^{11} \text{ cm}^{-2}$, $d = 1$ nm, $d_{\text{ox}} = 300$ nm). For the fit function, the autocorrelation function was convolved with a Gaussian of FWHM = 30nm to account for broadening due to the size of the tip.

Figure 41 shows the autocorrelation function of the potential $C(r)$ for SiO_2/Si sample shown in Figure 40a and b. The $C(r)$ data from three images at distinct locations on the same sample were averaged, with the error bars given by the standard deviation of

the averaging. The best fit of the model to the experimental $C(r)$ is also shown in Figure 41. The fit parameters are $n_{\text{imp}} = (2.7 \pm 0.1) \times 10^{11} \text{ cm}^{-2}$ and $d = 4.7 \text{ \AA}$, a reasonable tip-sample distance for an AFM measurement. Although the model does not explicitly account for the cantilever oscillation, the tip-sample distance d is best understood as corresponding to an approximate minimum tip-sample distance (e.g. at the bottom of the cantilever oscillation). The short range behavior of the autocorrelation function is determined by the tip-sample distance (d) and the tip-size broadening (r_{tip}), while the downturn at large r is determined by the finite system size (limited by the image size and explicitly accounted for by discrete, numerical approach used for the fitting described above). The fit for mid-ranged distances ($50 \text{ nm} < r < 200 \text{ nm}$) depends primarily on n_{imp} which sets the overall vertical scale of $C(r)$. Variation of d and r_{tip} by a factor of two changes $C(r)$ by 2% in this region, allowing a highly accurate determination of n_{imp} independent of possible uncertainty in d and r_{tip} . I find a robust fit in this region within the 1.5 standard deviations for the five SiO_2 samples studied, with n_{imp} values in the range $(0.24 \pm 0.01) \times 10^{11} \text{ cm}^{-2}$ to $(2.7 \pm 0.1) \times 10^{11} \text{ cm}^{-2}$. The range represents the variation from sample to sample; much smaller variations are seen for different regions of a given sample. It is not clear whether the sample-to-sample variations are the result of variations between wafers (samples were obtained from different wafers) or due to an as-yet unidentified difference in processing conditions.

My method also allows me to analyze the previously published data in Ref. [44].

Figure 42 shows the application of the autocorrelation function analysis to a digitized

version of the SiO₂ potential fluctuation data in Reference [44] (previously analyzed using only the variance). The analysis yields $n_{imp} = (0.7 \pm 0.1) \times 10^{11} \text{ cm}^{-2}$ with $d = 47 \text{ nm}$ for a tip radius of 100 nm (fixed, as quoted in paper). This result is both consistent with the range of charged impurities densities observed in the present study and yields a tip sample distance of the same order of magnitude as estimated in Reference [44] (~100 nm).

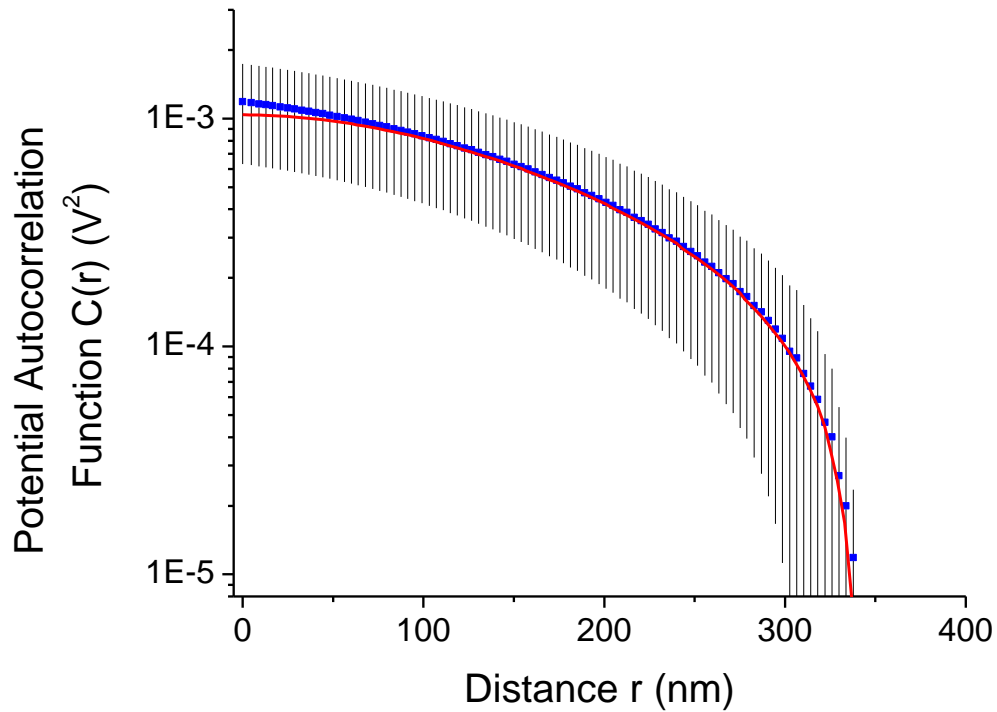


Figure 42: Autocorrelation function from experimental data presented in Ref. [44] (blue squares) and best theoretical fit ($n_{imp} = 0.7 \times 10^{11} \text{ cm}^{-2}$, $d = 47 \text{ nm}$, $d_{ox} = 300 \text{ nm}$). For the fit function, the autocorrelation function was convolved with a Gaussian of FWHM = 100 nm to account for broadening due to the size of the tip.

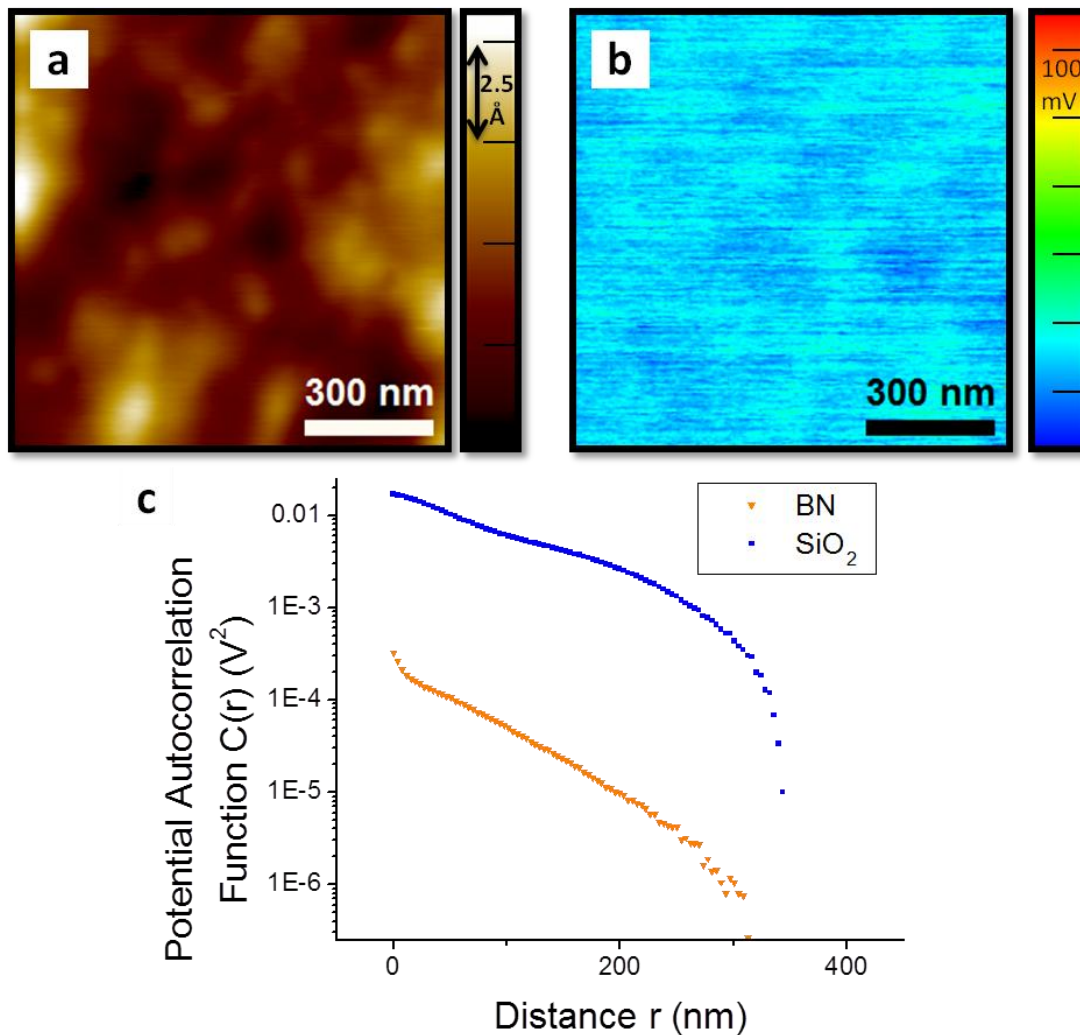


Figure 43: (a) Topographic and (b) potential images from a 40 nm h-BN flake exfoliated onto SiO₂. The same scales as used in Figure 40 is used for comparison (full range 630 mV) (c) The magnitude of the autocorrelation function for BN (orange triangles, average from 9 images) is reduced from that for the underlying SiO₂ (blue squares, same as Figure 41).

I now turn to the surface potential of exfoliated h-BN on SiO₂. Figure 43 shows the topography (Figure 43a) and surface potential (Figure 43b) for a 40 nm thick h-BN flake on SiO₂/Si (frequency shift $\Delta f = -70$ Hz, amplitude $A = 3.8$ nm). Comparison with the samples on bare SiO₂/Si (Figure 40b) shows significantly lower potential variations for h-BN (Figure 40b and Figure 43b utilize the same color scale). Similar

to the SiO₂ samples, the h-BN samples showed strong decay of $C(r)$ as r increases. Shown in Figure 43 is $C(r)$ computed for one of the h-BN samples by taking an average of 9 images from distinct areas. Comparing to the samples on SiO₂, $C(r)$ of the h-BN sample is almost two orders of magnitude lower. Although $C(r)$ in this particular h-BN sample is the lowest I measured, all other h-BN samples showed $C(r)$ lower than the cleanest samples on SiO₂. Of the three h-BN flakes measured, one showed $C(r)$ magnitude comparable to the one reported here and the other showed $C(r)$ magnitude $\sim 10\times$ greater than the one reported here (though still lower than the lowest $C(r)$ observed on SiO₂), though this third flake exhibited topographic features and region-to-region inconsistency in the potential distribution not observed in the other flakes, which may indicate that the data for this particular flake is an unreliable metric for understanding charged impurity density in h-BN substrates. I note that the curve shape of $C(r)$ of the h-BN samples is not explained by the simple 2D charge trap model presented above, for any d . However, the lower magnitude of $C(r)$ for h-BN compared to SiO₂, which indicates reduced potential fluctuations, suggests that reduced potential/density inhomogeneity is responsible for the increase in the maximum mobility limited by charged impurity scattering observed for graphene on h-BN compared to SiO₂.

Given that the h-BN is exfoliated on top of the SiO₂, the interaction between the h-BN and the SiO₂ should be considered for a more complete understanding the h-BN charged impurity landscape. As a “cleanest-case” scenario one may consider BN as a simple dielectric layer which passively screens the charges in the underlying SiO₂,

but provides no additional charged impurities of its own. Applying this simple model, I expect the results from the h-BN to be comparable to moving the charges further away by 40 nm (the thickness of the h-BN); a cartoon of this scenario is shown in Figure 44. However, I find that the h-BN exhibits lower charged inhomogeneity than this “cleanest case” scenario. Figure 45 shows a theoretical prediction for the “cleanest case” scenario potential autocorrelation in comparison with the actual experimental data for SiO₂ and h-BN. The model utilizes the parameters obtained from the fit for the SiO₂ $C(r)$, but sets $d = 40\text{nm}$ (the tip-sample distance – equal to the h-BN thickness). Notably, the actual experimental data is much cleaner than this model predicts. Furthermore, a comparison can be made between the experimental data for the h-BN substrate and experimental data from a scan lifted 40 nm above the SiO₂ sample, shown in Figure 46. The experimental data is distinct from the prediction from the model, pointing to the need for a more thorough model for the autocorrelation function for data far from the surface. The current model does not consider the dynamics of the AFM measurement nor the electrostatic interactions with the tip itself, both of which may be more important for measurements far from the surface (where the bulk character of the probe technique has a larger effect). However, the lifted scans above the SiO₂ also do not describe the observed cleanliness of the h-BN flake. This suggests that the h-BN is serving as more than a simple dielectric, perhaps passivating the h-BN/SiO₂ interface or actively screening the charged impurities. Further experiments and more detailed theoretical models are needed to tease apart the contribution of instrumental properties and materials properties in explaining the cleanliness of h-BN.

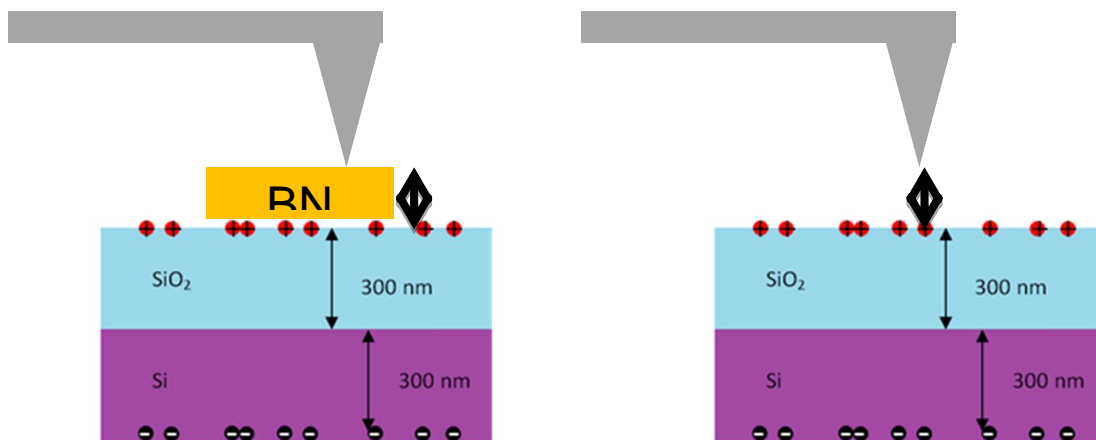


Figure 44: Cartoon for “cleanest case” scenario for charged inhomogeneity of h-BN. Here BN is treated as a simple dielectric (no active screening).

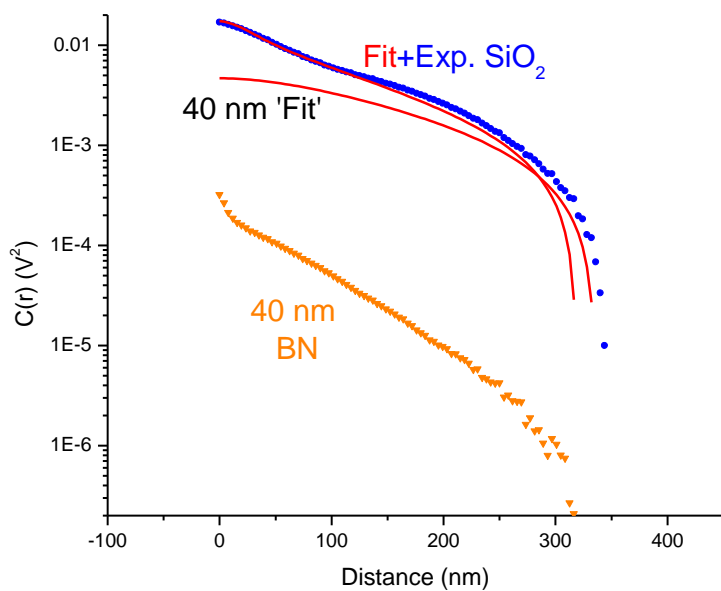


Figure 45: The “cleanest case” scenario model potential autocorrelation function for h-BN (red, 40 nm ‘Fit’) is shown along with the experimental data and fit for h-BN and SiO₂. Here the “cleanest case” scenario model ACF is developed using d=40nm (h-BN thickness) and the parameters extracted from fitting the SiO₂.

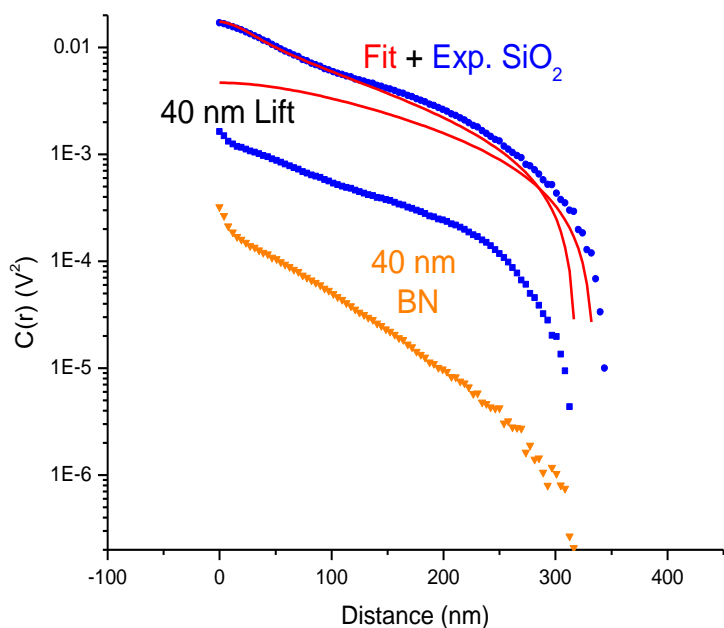


Figure 46: Experimental potential autocorrelation function for 40 nm lifted scan over SiO₂ (blue, 40 nm lift) shown in comparison to experimental data for substrates h-BN (orange) and SiO₂ (blue) and theoretical models (red line).

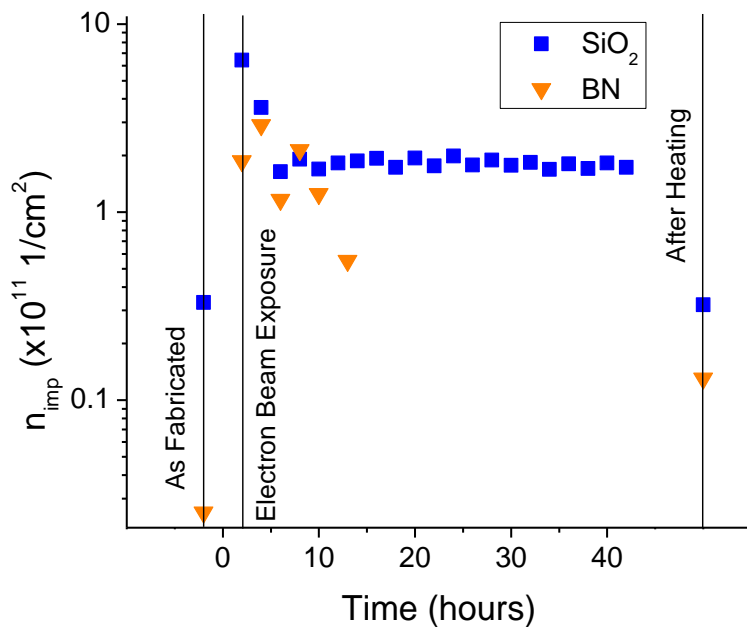


Figure 47: Effect of fabrication procedures (electron beam exposure and annealing) on graphene substrate charged impurity density. The surface charge densities before electron beam exposure, as a function of time after the 30s electron beam exposure, and after annealing at 250 °C are shown for SiO₂ (blue squares) and h-BN (orange triangle) substrates.

A more complete understanding of the link between charged impurities in the substrate and device mobility requires consideration of common graphene fabrication conditions. Here I address the effects of electron beam lithography and annealing by dosing as fabricated substrates *in situ* with an electron beam using a scanning electron microscope (SEM) for 30 seconds. Figure 47 shows the charge density as a function of time after SEM exposure for h-BN [initial $n_{\text{imp}} = 2.5 \times 10^9 \text{ 1/cm}^2$] and a clean SiO_2 sample [initial $n_{\text{imp}} = (0.24 \pm 0.01) \times 10^{11} \text{ 1/cm}^2$]. The n_{imp} values in Figure 47 were obtained from the value of $C(r)$ at $r = 50 \text{ nm}$. Based on beam parameters, image size, and dosing time I expect the total electron exposure is on the order of 10^{11} - 10^{12} cm^{-2} , consistent with the charge densities observed immediately after dosing. This dose is comparable to or lower than the minimum order expected during standard graphene device fabrication by electron beam lithography where I estimate that an electron dose of at least order 10^{12} cm^{-2} results from unintentional exposure while locating and aligning to existing patterns on the substrate; the dose in the intentionally-exposed contact areas is much higher, on order 10^{15} cm^{-2} . Thus the behavior observed in Figure 47 from my samples is indicative of realistic fabrication conditions. The SiO_2 appears to reach a metastable state 8 hours after electron-beam dosing with charged impurity density of $\sim 2 \times 10^{11} \text{ cm}^{-2}$ while the h-BN did not show evidence of metastable charge density greater than $5 \times 10^{10} \text{ cm}^{-2}$. Both SiO_2 and h-BN return to close to their initial state after 30 minutes of heating at ~ 250 - $300 \text{ }^\circ\text{C}$, though h-BN appears to be less reversible. Some research groups have adopted the practice of annealing graphene in a reducing environment post lithography in order to remove

resist residues [54]; the results suggest the possibility that annealing may have the additional benefit of removing metastable trapped charge induced by electron-beam processing though the annealing conditions in this study (UHV) are not typical.

I now discuss the implications of the results for understanding the disorder-limited charge carrier mobilities observed for graphene on SiO₂ and h-BN substrates. A previous study [30] used controlled adsorption of potassium (a charged impurity on graphene) to determine the relationship between charged impurity density n_{imp} and charge carrier mobility μ in graphene: $\mu = 5 \times 10^{15} \text{ V}^{-1}\text{s}^{-1}/n_{\text{imp}}$. The best measured mobilities for graphene on SiO₂ are $\sim 25,000 \text{ cm}^2/\text{Vs}$ [15,17,18] implying charge trap density $n_{\text{imp}} \sim 2 \times 10^{11} \text{ cm}^{-2}$ or more. Moreover, scanning probe studies from several groups show consistent results for the potential fluctuations in graphene on SiO₂ (electron and hole “puddles”) with *rms* charge variations of $2\text{-}4 \times 10^{11} \text{ cm}^{-2}$ implying n_{imp} of a few 10^{11} cm^{-2} (see Table 1). [40,43,44] Thus there is significant evidence that charge trap densities seen by graphene on SiO₂ are at least $\sim 2 \times 10^{11} \text{ cm}^{-2}$. The experimentally-determined $n_{\text{imp}} = 0.24 - 2.7 \times 10^{11} \text{ cm}^{-2}$ for SiO₂ samples encompasses the expected range inferred from these previous experiments. However, it is difficult to understand the cleanest samples (with $n_{\text{imp}} = 0.24 \times 10^{11} \text{ cm}^{-2}$), which are seemingly inconsistent with previous inferred substrate charge density results for graphene on SiO₂. I believe the solution to this conundrum is offered by the electron-beam dosing results. I find that long-lived charge densities of $\sim 2 \times 10^{11} \text{ cm}^{-2}$ can be induced in the cleanest SiO₂, implying that the density of deep trap states at the SiO₂ surface is at least this large. I hypothesize that the presence of conducting graphene

fills these deep trap states through tunneling and thus trapped charge densities of $\sim 2 \times 10^{11} \text{ cm}^{-2}$ are unavoidable at the $\text{SiO}_2/\text{graphene}$ interface. An additional possibility is that ambient species adsorbed between graphene and SiO_2 during deposition may act as charge traps. [40,44,140–142]

For h-BN I consistently observe lower potential fluctuations than for SiO_2 , and also lower metastable trapped charge densities. The results support the hypothesis that lower trapped charge densities in h-BN are responsible for the higher disorder-limited charge carrier mobility for graphene on h-BN compared to SiO_2 . The potential fluctuations on h-BN are often poorly fit by the model of random charges in a 2D plane. More work is needed to understand the details of the charge distribution, including its depth dependence and correlations.

6.3 Conclusions

In conclusion, I have used Kelvin probe force microscopy to map the surface potential of both SiO_2/Si and h-BN substrates. I analyze the experimental potential autocorrelation function of the substrates and compare to a numerical model of charges randomly distributed in a 2D plane. For SiO_2/Si I have observed charged impurity densities in individual samples of $n_{\text{imp}} = 0.24 - 2.7 \times 10^{11} \text{ cm}^{-2}$. h-BN substrates show improvement in potential inhomogeneity over SiO_2 , consistent with the observed improvement in mobility for graphene devices on h-BN. Electron beam dosing creates metastable charge trap populations of a few 10^{11} cm^{-2} which can be removed by annealing at $250 \text{ }^\circ\text{C}$. The observation of metastable charge trap

populations on the surface of SiO₂ with concentrations of a few 10¹¹ cm⁻² is strongly suggestive that such charge traps, filled by device processing or simply by contact with conducting graphene, are responsible for the scattering and charge-carrier inhomogeneity in graphene on SiO₂. I expect the technique and analysis methods presented here can be generally useful to assess the quality of new substrates for graphene or other self-assembled materials.

Chapter 7: Potential Steps at C₆₀-TiOPc-Ag(111) Interfaces: UHV - Noncontact Scanning Probe Metrology

Close-packed spheres lurk near

A honeycomb field invites

Boundary too sharp

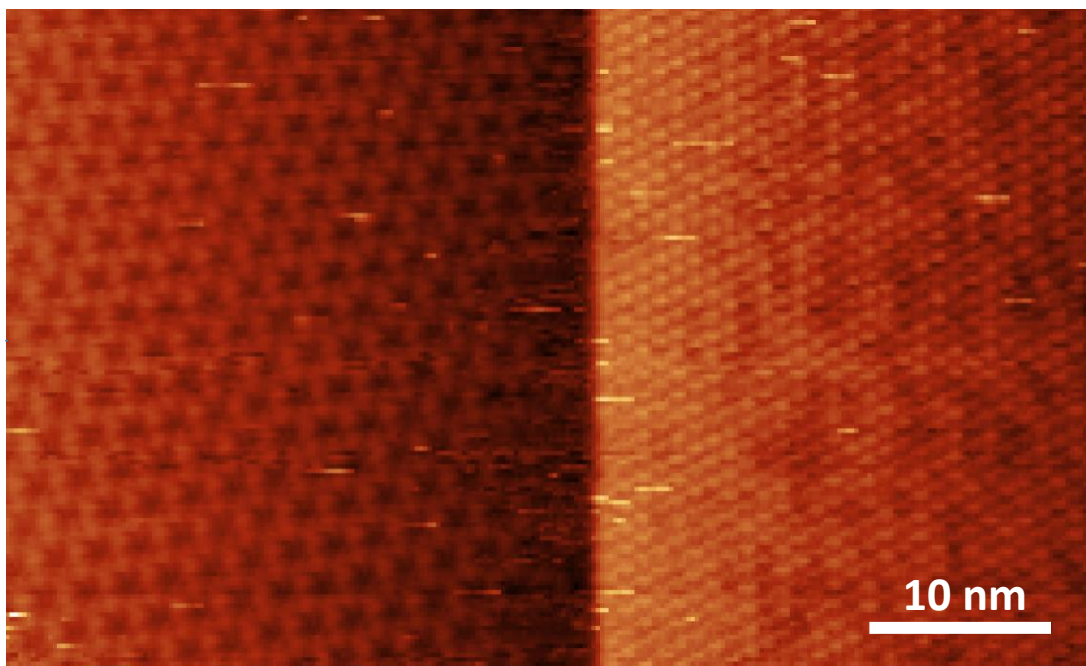


Figure 48: Interface between honeycomb phase TiOPc and close-packed C₆₀ viewed by STM (V = 1.594 V, I = 27.5 pA).

This chapter is largely based on the paper “Potential Steps at C₆₀-TiOPc-Ag(111) Interfaces: UHV - Noncontact Scanning Probe Metrology” [143]. The chapter presents UHV Kelvin probe force microscopy measurements of nanoscale structure–electric potential relations in films of the organic molecular semiconductors C₆₀ and titanyl phthalocyanine (TiOPc) on Ag(111). Images of domain structures and boundaries are obtained with molecular resolution, while simultaneously quantifying

the local surface electric potential difference across the boundaries. Sensitivity and spatial resolution for the local potential measurement are first established on Ag(111) through direct observation of the electrical dipole and potential step, $\varphi_{\text{step}} = 10 \pm 3$ mV, of monatomic crystallographic steps. A local surface potential increase of 27 ± 11 mV occurs upon crossing the boundary between the neat Ag(111) surface and C₆₀ islands. Potential steps in binary C₆₀-TiOPc films, nanophase-separated into crystalline C₆₀ and TiOPc domains, are then mapped quantitatively. The 207 ± 66 mV potential step across the C₆₀-to-TiOPc domain boundary exhibits a 3.6 nm width that reflects the spatial resolution for electric potential across a material interface. The absence of potential asymmetry across this lateral interface sets the upper bound for the C₆₀-TiOPc interface dipole moment per molecule as 0.012 e nm.

7.1 Introduction

Surface chemical modifications are widely used to tune the work function of a material to enhance thermionic and optoelectronic properties [144,145]. Spatially averaging methods, such as photoelectron spectroscopy and Kelvin probe capacitance, are extremely valuable for quantifying the surface potential of monolayer films and interface dipole formation with high potentiometric precision [146–148]. For nanostructured material interfaces, however, local variations in the electric potential are of considerable technological importance. Organic photovoltaic cells of the bulk heterostructure design, for example, utilize the electric potential offset at donor-acceptor interfaces to drive charge

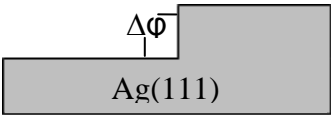
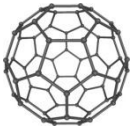
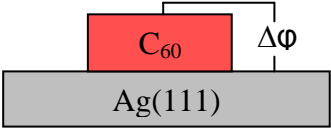
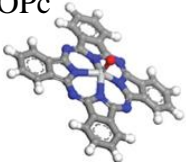
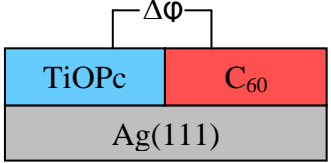
separation [149,150]. In solid oxide fuel cells, surface potential gradients at phase boundaries in the cathode control the kinetics of oxygen reduction in low-temperature devices [151,152]. Quantitative measurements of the local surface potential are needed to precisely determine the magnitude and gradient of potential steps at low dimensional material interfaces.

In this chapter non-contact scanning Kelvin probe force microscopy (NC-KPFM) and atomic force microscopy (NC-AFM) are used to make quantitative measurements of the electric potential steps at several low-dimensional material interfaces. Films of the molecular semiconductors titanyl phthalocyanine (TiOPc) and C_{60} , illustrated in Table 2, undergo nanophase separation on Ag(111), yielding abrupt molecular interfaces. The system is prepared *in situ* and characterized with ultrahigh vacuum (UHV) – scanning probe microscopy. The C_{60} -TiOPc-Ag system was chosen because TiOPc [153,154], and C_{60} [155,156] separately yield well characterized monolayer phases on Ag(111). Additionally, work functions for C_{60} monolayers [157–159] and TiOPc monolayers [160,161] have been studied with spatially averaging probes. Binary C_{60} -TiOPc films are known to undergo nanophase separation into domains with molecularly abrupt domain boundaries [162]. Finally, C_{60} -TiOPc has been used as an active layer in photovoltaic devices with reports of high power conversion efficiencies (PCE) [163]. Tsuzuki et al. have demonstrated that the PCEs of TiOPc based solar cells are improved by doping with C_{60} [164]. While the global photovoltaic properties have been observed [165,166], local potential measurements would reveal the key electronic features of the interface of these organic donor-

acceptor pairs [167]. For the work in this chapter, monatomic crystalline steps on the clean Ag(111) surface provide a convenient internal standard for this local potential determination, as the local charge redistribution about the crystallographic step produces a corresponding change in the surface potential [168–171].

As discussed in chapter 3, noncontact Kelvin Probe Force Microscopy (NC-KPFM) has emerged as a powerful tool to measure the local electric potential between a surface and proximal tip [167,172,173]. Here, KPFM resolution is discussed as related to the work in this chapter. Atomically resolved modulations in the electrostatic potential on a periodic Ge/Si structure, attributed to charge redistribution in dangling surface bonds, have been resolved by NC-KPFM under ultrahigh vacuum conditions [174]. This method has been further used to map the surface potential for diverse material systems that include charge-separating polymers under illumination [175], fullerene-polymer mixtures [176,177], and nanoparticle arrays [178]. As a quantitative probe, however, NC-KPFM is limited by the finite dimension of the tip and the roughness of the sample surface; in this local measurement, simultaneous variations in surface topography and surface potential are not clearly distinguished, introducing uncertainty in the electric potential determination [173,179]. In this chapter atomically flat surfaces with molecularly resolved domain boundaries are measured for unambiguous determination of electric potential steps at material interfaces. Nanoscale surface potential features are validated through measurements of a monatomic crystallographic step on Ag(111), which serves as a reference standard for a surface potential step.

Table 2: Local Work Function Values from NC-KPFM measurements

Adsorbate Coverage	Molecule Models	Boundary	Direct Kelvin Measurement (mV)	Local work function deduced (eV)
0.0 ML			10±3	$\Phi_{\text{Ag}(111)} = 4.48 \pm 0.03^{\text{a,b}}$
0.4 ML C ₆₀			27±11	$\Phi_{\text{C}_{60} \text{ island}}^{\text{local}} = 4.50 \pm 0.01$
1.0 ML C ₆₀ + TiOPc			207±66	$\Phi_{\text{TiOPc island}}^{\text{local}} = 4.27 \pm 0.07$

^aGiesen, K.; Hage, F.; Himpsel, F. J.; Riess, H. J.; Steinmann, W. *Physical Review Letters* **1985**, *55*, 300.

^bChelvayohan, M.; Mee, C. H. B. *J. Phys. C* **1982**, *15*, 2305.

7.2 Sample Preparation

This section expands upon the sample preparation techniques discussed in Section 3.2. Ag(111) surfaces were prepared by physical vapor deposition of Ag onto cleaved mica surfaces, followed by several cycles of Ar ion sputtering (1000 V, 30 min) and annealing by resistive heating (683 K, 20 min), as previously described in References [153,154]. Sequential physical vapor deposition of the organic molecules was performed onto the room temperature Ag(111) substrate. To enhance phase separation, the more cohesive species, C₆₀, was first deposited from a Knudsen cell

(source temperature 610 K) to produce submonolayer (0.3-0.4 ML) C₆₀ films with close-packed island structures. The TiOPc was then deposited from a separate Knudsen cell (source temperature 490 K) at low flux rate (0.1 ML/min) to complete the monolayer with TiOPc in the thermodynamically favored honeycomb phase. Film coverage and structure were determined through UHV-STM measurements [see Figure 48], performed immediately prior to the non-contact force measurements, and further monitored during the potentiometric measurement with NC-AFM.

All scanning probe force measurements were obtained in non-contact mode in a UHV-STM/AFM system (JEOL JSPM-4500A) using the simultaneous AFM/KPFM technique, as described in Chapter 3. Cantilevers used were Pt-coated Si with a nominal radius of curvature of 30 nm and a resonance frequency of ~300 kHz (nominal k = 40 N/m). Data sampling was typically taken every 0.1 nm in the raster direction, with 0.2 nm increments between line scans. Slow scan rates of ~5 nm/s were used in obtaining dual AFM topography and KPFM bias images to eliminate crosstalk between AFM and Kelvin feedback loops.

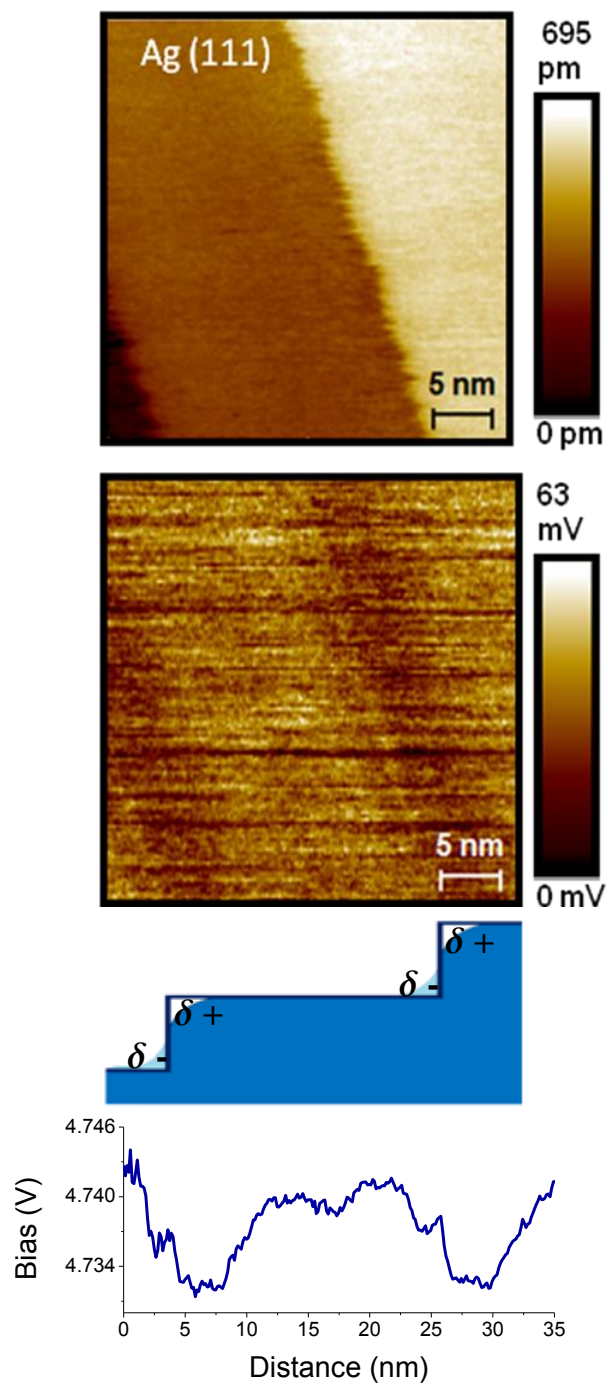


Figure 49: Local measurement of Ag(111) monatomic step-edge dipole: (a) AFM topographic image of surface topography ($A=1\text{nm}$, $\Delta f=-490\text{Hz}$) with two crystallographic steps (b) corresponding Kelvin Probe image (c) schematic of Ag(111) step-edge dipole due to Smoluchowski smoothing (d) surface potential measured perpendicular to steps (120 line average) (blue) . See Supplemental Information for related classical simulation.

7.3 Ag(111) Step Characterization

The sensitivity and spatial resolution of this NC-KPFM measurement are first established by mapping the local electrostatic potential for Ag(111) in the vicinity of monatomic crystallographic steps. Dual surface potential and topography images for Ag(111) steps are shown in Figure 49. Three monatomic steps appear in the topography image (a), with dark bands at the upper step edge in the corresponding potential image (b). These potential bands are a local measure of the step-edge dipole that results from the classic electron smoothing effect put forth by Smoluchowski [168]. The step-edge dipole was first measured in work function measurements on high index (stepped) surfaces [169] and later sensed locally on Au(111) with scanning tunneling spectroscopy [180]. Electrocapacitance measurements on macroscopic crystals have quantified the Ag(111) step-edge dipole moments, determining $1.38 \times 10^{-3} \text{ e nm}$ for the most stable step-edge structure [181,182]. The KPFM permits a quantitative measure of the local step-edge dipole [164]. Herein, the DC bias correction is applied to the sample, and, regions of higher surface potential correspond to lower applied V_{bias} . The dark V_{bias} bands at the upper step edge thus indicate electron depletion due to Smoluchowski smoothing, whereby electrons flow from the upper step edge to the lower step edge thereby ‘smoothing’ the electron density (reducing the total $|\mathbf{k}|$ of the electrons). This effect is quantified in the average line profiles (Figure 49c). The low V_{bias} band is fit to a Gaussian peak, giving a magnitude of $10 \pm 3 \text{ mV}$. This local potential in the vicinity of the crystallographic step is simulated with a classical model consisting of a line of

step-edge dipoles. Based upon the step dipole value of $1.38 \times 10^{-3} \text{ e nm}$, the 10 mV potential dip is produced at a height 1.6 nm above the surface, a typical value for the tip-sample distance. A discussion of the model follows.

The model treats the step-edge dipole as lines of positive and negative charges separated by the height of an Ag(111) step, as per Figure 50a. The potential for each line of charge is given by

$$V = \frac{\lambda \ln(r)}{2\pi\epsilon_0} \quad (34)$$

where λ is the linear charge density along the step, r is the distance between the line charge and the point of interest, and ϵ_0 is the vacuum permittivity. The resulting potential is a superposition of potentials for the separated line charges,

$$V_+ + V_- = \frac{\lambda \ln\left(\frac{r_+}{r_-}\right)}{2\pi\epsilon_0} \quad (35)$$

where r_+ and r_- are the distance from the point of interest to the positive and negative line poles of the step-edge dipole.

The step-edge dipole for the thermodynamically favored monatomic steps on Ag(111) ("B" steps characterized by a [111] oriented step-riser), has been independently measured as $1.38 \times 10^{-3} \text{ e nm}$ [182]. Taking the 0.236 nm height of the Ag step edge as the dipole length, this corresponds to a linear charge density of $3.24 \times 10^{-12} \text{ C/m}$. The potentiometric profile across this dipole at a height 1.05 nm above the surface exhibits a 10 mV decrease, as shown in Figure 50b. This decrease matches the

KPFM –measured value at a height that is within the expected range of tip-sample separations in this non-contact AFM measurement. The ± 3 mV uncertainty in the measured value of the potential dip is reproduced with heights (i. e. tip-sample separations) that range from 0.8 nm (13 mV) to 1.6 nm (7 mV).

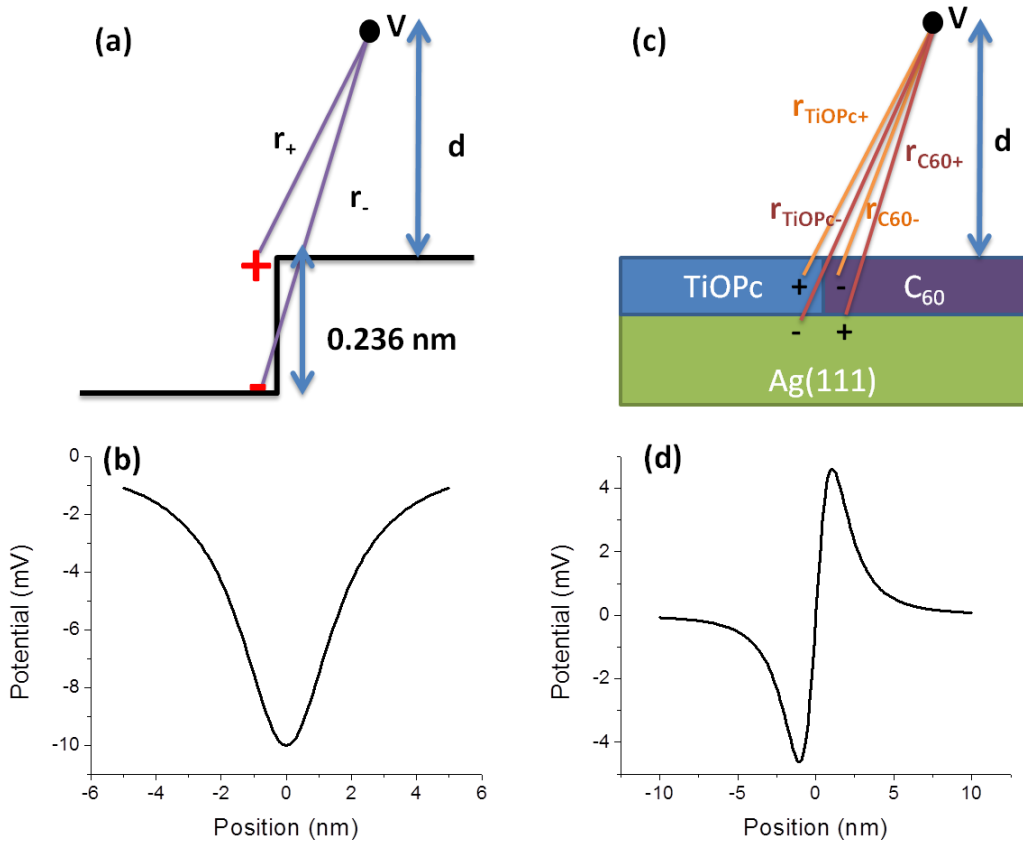


Figure 50: Electrostatic simulation of potential profiles for select interface dipoles: (a) Schematic illustration of the crystallographic step-edge dipole, shown in cross section; (b) Simulated potential profile from a 1.38×10^{-3} e nm step-edge dipole at a height 1.3nm above the surface. The 10 mV potentiometric decrease above the step reproduces the KPFM observation on Ag(111). (c) Schematic illustration of the interface dipole at the C_{60} - TiOPc domain boundary and corresponding image charge, shown in cross section (d) Potential profile from the molecular interface dipole arrangement of (c). The asymmetric profile is characteristic of this lateral dipole arrangement. A dipole value of 0.012 e nm per molecule was used to generate the 5 mV potential feature at a 1.6 nm height above the surface. The absence of this feature in the KPFM measurement sets an upper bound on the C_{60} – TiOPc interface dipole.

Simultaneously measured crystallographic and potential steps from Figure 49 have distinct widths. Topographic steps have a relatively narrow width of 1.8 nm determined from the full width at half maximum (FWHM) of the step width. This

width represents the effective spatial resolution for boundary structure in our force measurement. The corresponding potential steps (KPFM bands) are considerably broader, exhibiting a 7.5 nm FWHM. As will be demonstrated below for the C₆₀ – TiOPc interface, our spatial resolution for potential steps is a factor of two smaller than the broad Ag(111) KPFM bands. The Ag(111) potential band width is thus not limited by instrument resolution, but this width is comparable to the Fermi wavelength of the Ag(111) surface state, $\lambda_F = 7.6$ nm [183,184]. The KPFM band width for the Ag(111) step is thus taken as a direct measure of the screening length for the step-edge dipole.

7.4 C₆₀-Ag(111) Interface

Local variations in the surface electric potential due to C₆₀ adsorption are next examined. At partial monolayer coverage, C₆₀ molecules readily form hexagonal close-packed island structures [185]. Figure 51a shows a topographic image acquired for a 0.4 monolayer (ML) film of C₆₀, in which C₆₀ islands are bright and the bare surface appears dark. The C₆₀ molecular arrangements are clearly resolved and a packing model is provided in Figure 51c. In the corresponding potential image (Figure 51b), bright C₆₀ islands indicate an increased surface potential relative to the bare Ag(111) regions. To quantify this difference, a histogram of the surface potential profile (Figure 51c) was first fit to two Gaussians, representing the neat Ag(111) and C₆₀-covered regions. The work function difference was then determined from the potential difference between the peak centroids. This analysis

was performed for 18 images to obtain a statistically significant value for the work function difference of 37 ± 31 mV. This data set included two obvious outliers (greater than two standard deviations from the mean) that skew the value for the work function. Removing these from the data set as justified by application of Chauvenet's criterion [186,187], gives 27 ± 11 mV, where the C_{60} serves to increase the work function relative to the bare Ag(111).

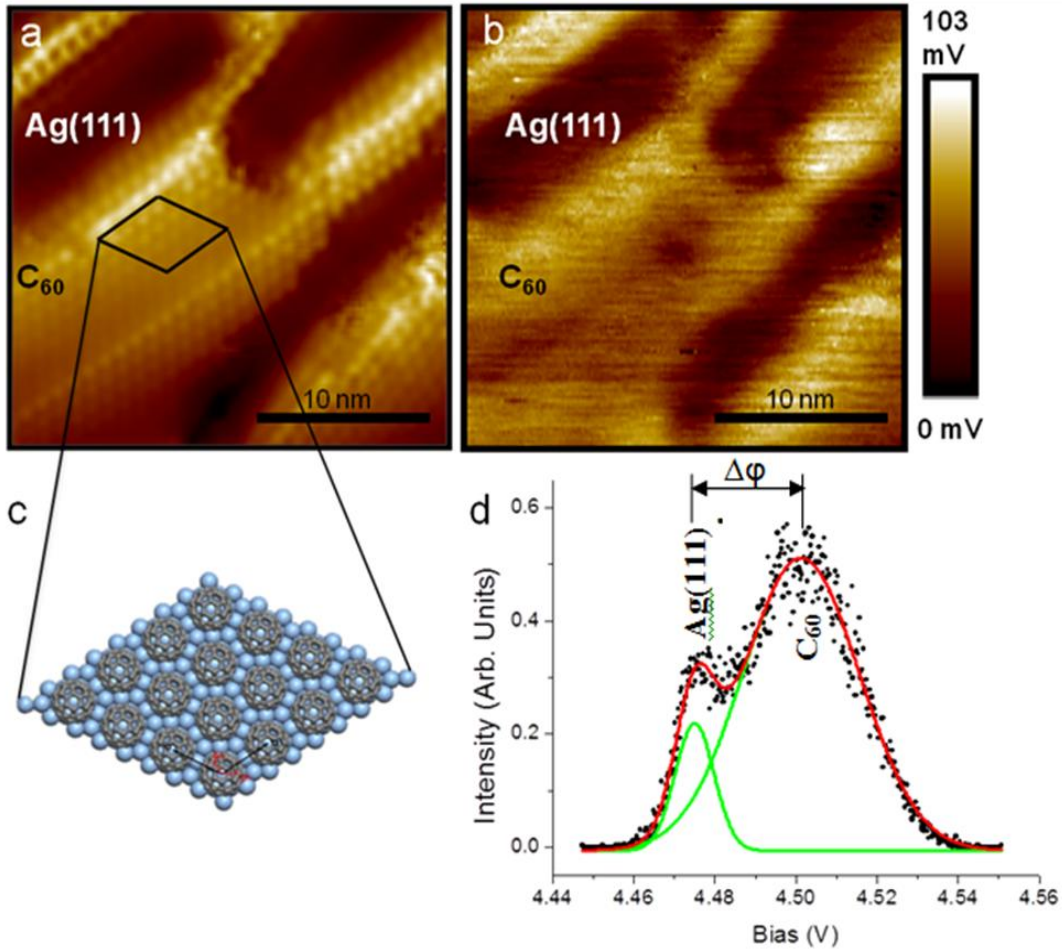


Figure 51: Local measurement of surface potential for submonolayer 0.4 ML C_{60} film on Ag(111): (a) AFM topographic image ($A = 1.85$ nm, $\Delta f = -856$ Hz) with molecularly resolved C_{60} islands (b) Kelvin probe image of region (a); (c) Model of C_{60} arrangement for outlined region in (a) (d) histogram of surface potential values from (b) and referenced to the known Ag(111) work function

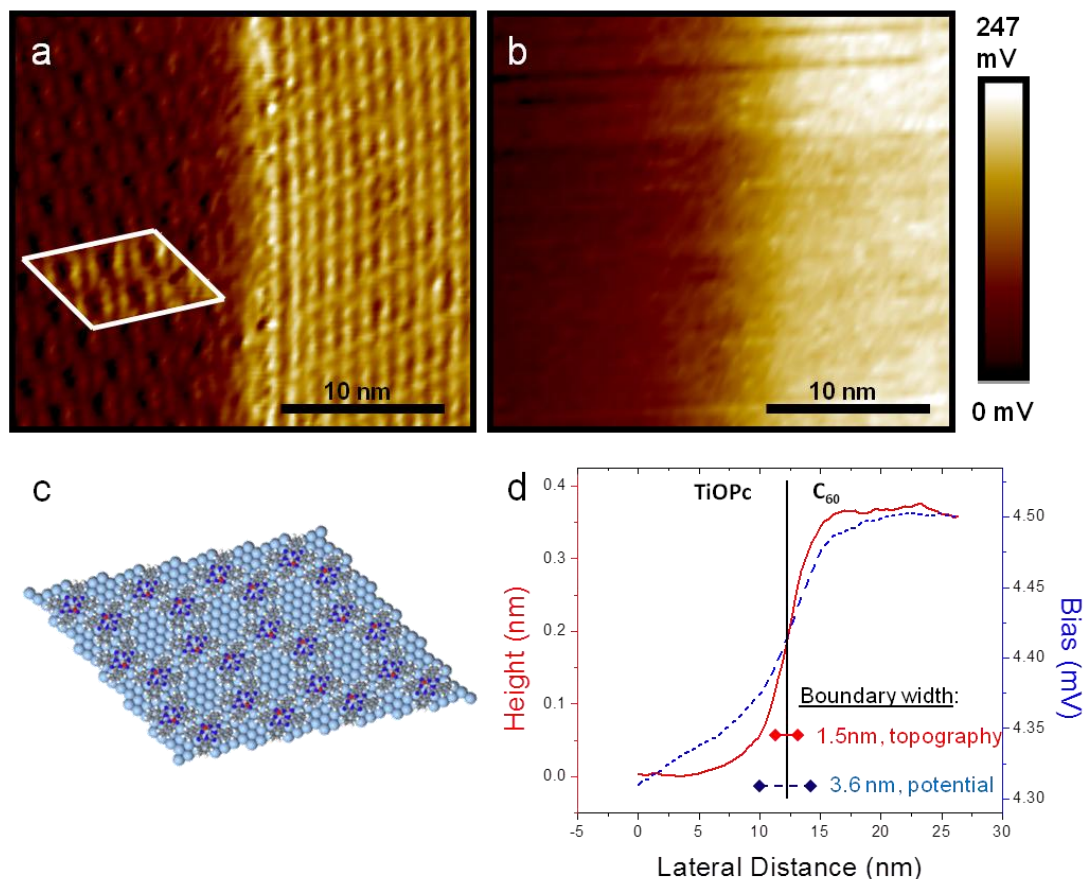


Figure 52: Local measurement of potential across C_{60} -TiOPc monolayer domain boundary: (a) NC-AFM topography ($A = 2\text{ nm}$, $\Delta f = -700\text{ Hz}$) shows molecular contours of TiOPc domain (left, honeycomb structure) and C_{60} domain (right, hexagonal structure). An outlined section of the TiOPc domain is raised to better view the periodicity. (b) Kelvin probe image of region (a); Model of TiOPc honeycomb arrangement (from Ref. 10) corresponding to the region in (a) For visual clarity, the pore-occupying TiOPc molecule is removed. (d) Line profiles of surface topography and surface potential measured perpendicular to grain boundary. Domain boundary widths are 1.5 nm in topography and 3.6 nm in potential (FWHM).

7.5 C_{60} -TiOPc-Ag(111)

We next examine nanophase-separated C_{60} -TiOPc monolayer films. Topographic images of this binary film (Figure 51a) show the organization of the TiOPc (left) and C_{60} (right) domains. Under further magnification, the TiOPc domain reveals the honeycomb pattern that is the most stable TiOPc monolayer structure on Ag(111), as previously reported [157,158]. According to the structural model [157](Figure 51c),

the honeycomb frame is comprised of pairs of TiOPc molecules arranged with opposing 40° tilt angles. Each honeycomb pore site is further occupied by a nearly planar TiOPc molecule, omitted here for visual clarity. Other phases of TiOPc were also observed in this work (Figure 53) [154], including a phase that, to my knowledge, was previously unreported which we now call the ‘flower’ phase (Figure 53c). However, observation of these other phases was more infrequent and are not included in the potential differences calculations for the chapter. As above (Figure 51c), the C_{60} domain consists of hexagonal-close-packed C_{60} molecules. These non-contact AFM measurements, performed concurrently with KPFM measurements, resolve individual C_{60} molecules and pairs of TiOPc molecules in these ordered structures. The observed 0.35 nm height difference between the C_{60} and TiOPc domains further corroborates the above structural models. The potential image corresponding to this film structure (Figure 52b) has bright C_{60} domains (high surface potential) relative to the dark TiOPc domains (low surface potential). The work function difference between the C_{60} and TiOPc domains is further quantified through potential histograms analysis. Histograms for the C_{60} regions and the TiOPc regions were calculated separately, (single peak) in order to exclude the immediate C_{60} -TiOPc boundary in the determination of the work function difference. A work function difference of 221 ± 83 mV between these domains was determined from 16 images. Applying Chauvenet’s criterion [186,187] to eliminate outliers gives a value of 207 ± 66 mV (15 images). Absolute work function values are obtained by reference to an average of two recent measurements of the Ag(111) work function [188,189], 4.48 ± 0.03 eV value for the Ag(111) work function: over close-

packed C_{60} domains, the local work function increases to a value of 4.50 ± 0.01 eV; over honeycomb TiOPc domains, the work function decreases to a value of 4.27 ± 0.07 eV.

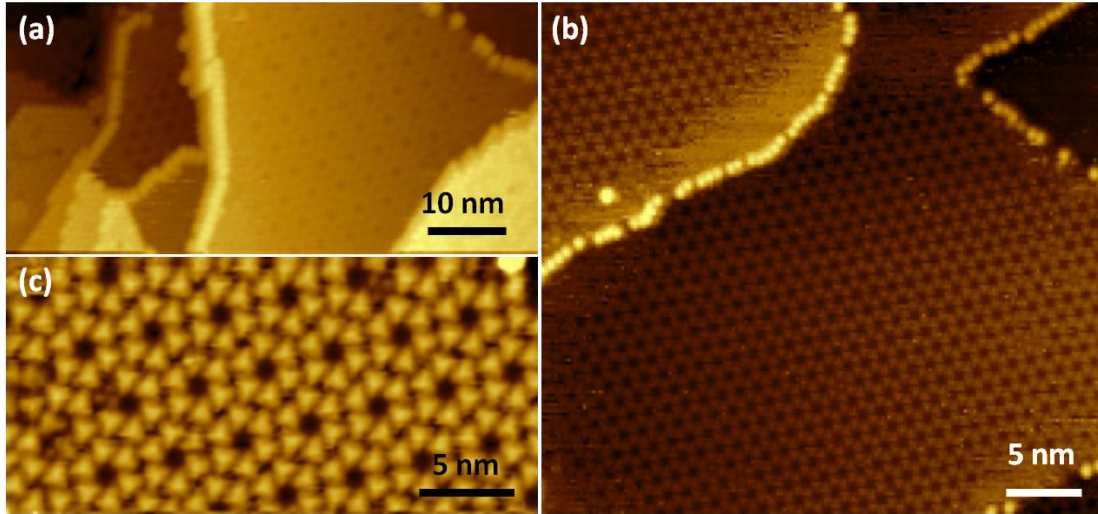


Figure 53: STM images showing several distinct phases of TiOPc on Ag(111): (a) Coexisting honeycomb and flower phase ($V_b = 1.594$ V, $I = 27.5$ pA), (b) two terraces of honeycomb phase TiOPc ($V_b = 1.526$ V, $I = 27.5$ pA), and (c) flower phase ($V_b = 1.205$, $I = 26.6$ pA)

Finally, the potential step at the immediate C_{60} -TiOPc domain boundary is examined. Topographic and potential steps, averaging over 120 line scans acquired perpendicular to the boundary, are shown in the line profiles (Figure 52c). These steps are separately fit to a convolution of a Gaussian and step function, giving FWHM values of 1.5 and 3.6 nm, respectively, for the topographic and electrostatic potential steps. The topographic resolution of this C_{60} -TiOPc boundary is within 0.3 nm of that observed for Ag(111) crystallographic steps, indicating a comparable tip shape for these structural measurements. The potential step width at the C_{60} -TiOPc boundary of 3.6 nm sets an upper limit for our spatial resolution of

potentiometric features. The symmetry of the potential step at the C₆₀ – TiOPc boundary is notable. The presence of a dipole at the C₆₀-TiOPc interface should introduce asymmetry in the local potential due to the parallel dipole orientation. The potentiometric profile at the molecular interfaces in nanophase-separated monolayer films may be calculated using the same approach as presented above in the analysis of the Ag(111) step dipole. In this case, the C₆₀ – TiOPc interface dipole is modeled as lines of positive and negative charges, separated by 1 nm to account for the finite molecular dimension and measured spacing. The screening by the Ag(111) substrate is described with image charges positioned 1nm below the silver surface plane, as shown in Figure 50c. Using the potential from Equation (34), the total potential for the lateral dipole distribution is

$$V_+ + V_- = \frac{\lambda \ln\left(\frac{r_{\text{TiOPc}+} r_{\text{C60}+}}{r_{\text{C60}-} r_{\text{TiOPc}-}}\right)}{2\pi\epsilon_0} \quad (36)$$

where $r_{\text{TiOPc}+}$, $r_{\text{TiOPc}-}$, $r_{\text{C60}-}$, $r_{\text{C60}+}$, and are the distances from the point of interest to the positive line charge in TiOPc, the image line charge for TiOPc, the negative line charge in C₆₀, and the image line charge for C₆₀ respectively.

This form yields the potentiometric profile shown in Figure 50(d). Within the 5 mV sensitivity limit of our KPFM measurement, no such asymmetric profile was detected. (The smooth potentiometric step that was observed experimentally results from the work function difference of the two different molecular domains). We determine the upper bound on the value for the C₆₀ – TiOPc interface dipole from the

sensitivity of the KPFM measurement. To generate a clearly observable peak in the potential at the measurement height, taken as 1.6 nm, a lateral dipole per molecule of just $0.012 e \text{ nm}$ is needed to add an asymmetric feature with sufficient magnitude (~ 5 mV) for convincing detection above our 3 mV noise floor. This corresponds to a TiOPc – C₆₀ charge transfer $< 0.012 e/\text{molecule}$. This negligible value is consistent with first-principles calculations of interface dipole formation in related molecular semiconductor interfaces (pentacene-C₆₀) [190]. A summary of values obtained for the local potential for the C₆₀–TiOPc–Ag(111) system is provided in Table 2.

Close-packed C₆₀ islands increase the local work function of Ag(111) by 27 ± 11 mV, comparable to the modest 60 mV [163] and 120 mV [161] increases observed by photoemission on macroscopic monolayer films. The error in photoemission-determined work function values is on the order of 60 mV, due to uncertainties in photon energies, the spectrometer electron transmission function, and the inevitable presence of crystallographic steps, which vary in density depending upon surface preparation. A small C₆₀-induced work function increase is further supported by layer-dependent work function measurements [191,192] extrapolated to the monolayer regime. A previous KPFM report of a larger 0.45 V local work function increase above C₆₀ islands [193] conflicts with the present results and falls well outside of the reported range for this system. Noting again the difficulty of separating topographic and potential variations in the KPFM method, this outlying value may reflect multiple edge dislocations and crystallographic steps within the local probe field of view.

Above honeycomb domains of TiOPc, the local work function of Ag(111) decreases by 173 ± 70 mV, comparable to the 280 mV shift observed for a monolayer of this dipolar molecule (in a different crystalline phase) on HOPG [161]. Neglecting the chemisorption contribution to the interface dipole, the work function difference across the TiOPc honeycomb domain can be related to the free-molecule dipole via the Topping model as $\Delta\phi = \frac{1}{\epsilon_0} P n_{dip} \left[1 + \frac{11\alpha}{4\pi} n_{dip}^{3/2} \right]^{-1}$. In this model of polarizable interacting dipoles P represents the vertical component of the molecular dipole, n_{dip} is the areal density of dipoles, ϵ_0 is the vacuum permittivity, and α is the polarizability of the TiOPc monolayer. The coefficient for α accounts for mutual screening and has a value of 11 for a triangular lattice. Taking the known value $n_{dip} = 1.2$ molecules nm^{-2} for the TiOPc film and $\alpha = 1 \times 10^{-27} \text{m}^3$ from the TiOPc monolayer on HOPG [161], we obtain the value $P = 0.017$ e·nm for the vertical component of the TiOPc dipole moment. This is in good agreement to the net 0.015 e·nm vertical moment resulting from the simple geometric projection of the free-molecule dipole, calculated as 0.062 e·nm, in the honeycomb arrangement [166]. As we have neglected charge distribution associated with chemisorption and assumed hexagonal-lattice screening for a TiOPc film structure with alternatively tilted molecules, such agreement is reasonable.

The local work function undergoes a smooth 207 ± 66 mV increase from TiOPc to C_{60} . For much thicker films, a C_{60} -TiOPc interface dipole has been suggested [165]. Through the local KPFM measurement, a C_{60} -TiOPc interface dipole would be

manifested as asymmetric banding at the interface. Based upon the C_{60} – TiOPc lateral arrangement (parallel dipole), the absence of such banding indicates that the dipole value must be less than 0.012 e nm per domain-boundary molecule.

The negligible dipole moment at the TiOPc - C_{60} domain boundary indicates minimal rehybridization between these donor-acceptor semiconductor molecules, at least when they are in direct contact with the silver substrate. The smooth potential step across this organic – organic interface is thus largely understood from the work function offsets of the separate C_{60} and TiOPc material domains. This potential boundary is thus predicted by the properties of the separate components, without significant shift by dipole formation. In organic solar cells, open circuit voltage is derived from the potential across the donor-acceptor interface, which, by extension, should be tunable through the electrostatic moments of molecular components. Efforts to control the open-circuit voltage through selective molecular insertion at material interfaces are already proving promising [194]. The charge separation dynamics at molecular interfaces will, of course, provide more stringent tests of the potential boundary.

7.6 Summary and Conclusion

In summary, we have utilized the KPFM method to perform quantitative measurements of the local surface potential across well-defined low-dimensional material interfaces. We have made the first local measurement of a step-edge dipole on a noble metal surface, providing a quantitative demonstration of classic

Smoluchowski smoothing. Molecularly-resolved topographic images in conjunction with potential measurements were performed on ultraflat films to isolate potential and topographic variations. Precise values for the local potentials in submonolayer C₆₀ films and nanophase-separated C₆₀-TiOPc films were obtained and supported by detailed comparison to macroscopic measurements. Symmetric potential steps across the C₆₀ – TiOPc boundary indicate negligible dipole formation along the donor-acceptor interface, with predictable potential steps that enable rational nanomaterial design.

Chapter 8: Summary and Conclusions

Five years. Eight chapters.

Much work done; much work to do.

Some concluding thoughts:

8.1 Summary

The field of graphene research has burgeoned during my time in graduate school. Substrates play a key role in determining graphene device mobilities and electronic properties. It is therefore important to understand the nature of the substrates being used and how the features of the substrate correlate with graphene device features and properties. Scanned probe techniques represent a powerful tool for determining the surface properties of graphene and graphene substrates and adequate resolution is critical to drawing meaningful conclusions from scanned probe studies. A key contribution of this thesis is high resolution characterization of both the topographic and potential landscape of common graphene substrates. From these high-resolution measurements, I find that the *substrate corrugation determines the graphene corrugation* (not intrinsic rippling) and that *charged impurities in the substrate limit carrier mobility in graphene devices*. I expect that the technique introduced to determine the charged impurity density, utilizing KPFM and an auto-correlation function analysis, will be generally useful in characterizing and improving substrates for graphene and other nano-electronics applications. Likewise the KPFM approach utilized to simultaneously characterize the electrostatic landscape and molecular

arrangement for C_{60} and TiOPc can be extended for the development of fundamental understanding of other organic heterojunction systems.

8.2 Future Outlook

There are several open research questions that I see as a natural extension of the work presented here:

1. **Graphene/h-BN:** *How does the thickness of h-BN influence graphene devices and how does the h-BN interact with the underlying SiO_2 substrate?*

h-BN with a thickness of only 40nm exhibits a significant improvement in charged impurity concentration of SiO_2 . In fact, the improvement seen from the work in Chapter 6 is greater than one might expect from simple dielectric screening of the charges in the SiO_2 substrate. Does the h-BN actively screen these impurities? Does it somehow ‘passivate’ the surface? Theoretical models for this system as well as detailed studies of the thickness dependent characteristics of h-BN may shed light on these questions.

2. **Graphene/ SiO_2 :** *What is the nature of the charged impurities on the SiO_2 substrates?*

The charged impurity concentration at the SiO_2 surface may be due to adsorbates, dangling bonds, or charge traps. Based on the evidence from the graphene corrugation work (Chapter 5), where annealing resulted in a lower Fourier amplitude (Figure 26c), adsorbates are likely present. The study of

the effect of fabrication conditions on the substrate charged impurity concentration (Chapter 6) showed a long-lived meta-stable charge density state, suggestive of charge traps at the SiO₂ surface. Surface chemistry experiments may be necessary to tease out the extent to which each of these factors contributes to the measured charged impurity concentration for SiO₂.

3. ***KPFM: Detailed models of Kelvin probe for semiconductor surfaces.***

The work with h-BN (Chapter 6) has pointed to the need for more thorough models of KPFM, which is relatively well understood for metal surfaces (the work function), but less well understood for semiconductor surfaces, especially when surfaces charges are introduced. There are several nice theoretical works considering Kelvin probe for insulating surfaces (for example [132–135]), but the application of these models to our particular experimental situations for the h-BN/SiO₂ system remains elusive. I suspect that a complete understanding of the nuances of the KPFM measurement as applied to the particular experimental system in Chapter 6 may also resolve the difficulty in the auto-correlation function analysis of the h-BN samples.

4. ***Organic Heterostructures: Characterization of thicker heterostructures with KPFM.***

The small molecule organic/substrate interaction contributed to the measurements in Chapter 7. It would be interesting to apply the KPFM characterization technique to thicker, but still well defined, organic

heterojunctions in order to disentangle the junction characteristics from the substrate influence.

In a broader sense, the future use of graphene depends on the development of large-scale processes for the production of high-quality graphene sheets with uniformly reproducible results. Additionally a robust, scalable approach to open a band gap in graphene must be established in order for graphene to find broader use as a nano-electronic material. These key questions are already being pursued [195–197] and their answers require the work of physicists, chemists, and engineers. While there is still some work to be done on the fundamental science of graphene, some of the greatest current challenges for graphene engineering oriented, and many members of the graphene research community are now turning their interests towards other two-dimensional materials, such as BN and the chalcogenides, both for characterization of materials properties and for engineering novel device structures.

Bibliography

- [1] P. R. Wallace, *Phys. Rev.* **71**, 622 (1947).
- [2] J. C. Slonczewski and P. R. Weiss, *Phys. Rev.* **109**, 272 (1958).
- [3] C. Schonberger, in (2000).
- [4] A. H. Castro Neto, F. Guinea, N. M. R. Peres, K. S. Novoselov, and A. K. Geim, *Rev. Mod. Phys.* **81**, 109 (2009).
- [5] M. R. Connolly and C. G. Smith, *Philosophical Transactions of the Royal Society A: Mathematical, Physical and Engineering Sciences* **368**, 5379 (2010).
- [6] K. S. Novoselov, D. Jiang, F. Schedin, T. J. Booth, V. V. Khotkevich, S. V. Morozov, and A. K. Geim, *PNAS* **102**, 10451 (2005).
- [7] K. S. Novoselov, A. K. Geim, S. V. Morozov, D. Jiang, Y. Zhang, S. V. Dubonos, I. V. Grigorieva, and A. A. Firsov, *Science* **306**, 666 (2004).
- [8] K. S. Novoselov, A. K. Geim, S. V. Morozov, D. Jiang, M. I. Katsnelson, I. V. Grigorieva, S. V. Dubonos, and A. A. Firsov, *Nature* **438**, 197 (2005).
- [9] A. Reina, X. Jia, J. Ho, D. Nezich, H. Son, V. Bulovic, M. S. Dresselhaus, and J. Kong, *Nano Lett.* **9**, 30 (2009).
- [10] X. Li, C. W. Magnuson, A. Venugopal, R. M. Tromp, J. B. Hannon, E. M. Vogel, L. Colombo, and R. S. Ruoff, *J. Am. Chem. Soc.* **133**, 2816 (2011).
- [11] X. Li, W. Cai, J. An, S. Kim, J. Nah, D. Yang, R. Piner, A. Velamakanni, I. Jung, E. Tutuc, S. K. Banerjee, L. Colombo, and R. S. Ruoff, *Science* **324**, 1312 (2009).
- [12] Y.-M. Lin, C. Dimitrakopoulos, K. A. Jenkins, D. B. Farmer, H.-Y. Chiu, A. Grill, and P. Avouris, *Science* **327**, 662 (2010).
- [13] C. Berger, Z. Song, T. Li, X. Li, A. Y. Ogbazghi, R. Feng, Z. Dai, A. N. Marchenkov, E. H. Conrad, P. N. First, and W. A. de Heer, *J. Phys. Chem. B* **108**, 19912 (2004).

- [14] P. W. Sutter, J.-I. Flege, and E. A. Sutter, *Nat Mater* **7**, 406 (2008).
- [15] Y.-W. Tan, Y. Zhang, K. Bolotin, Y. Zhao, S. Adam, E. H. Hwang, S. Das Sarma, H. L. Stormer, and P. Kim, *Phys. Rev. Lett.* **99**, 246803 (2007).
- [16] J.-H. Chen, C. Jang, S. Xiao, M. Ishigami, and M. S. Fuhrer, *Nat Nano* **3**, 206 (2008).
- [17] S. Cho and M. S. Fuhrer, *Phys. Rev. B* **77**, 081402 (2008).
- [18] J. Yan and M. S. Fuhrer, *Phys. Rev. Lett.* **107**, 206601 (2011).
- [19] X. Du, I. Skachko, A. Barker, and E. Y. Andrei, *Nature Nanotechnology* **3**, 491 (2008).
- [20] K. I. Bolotin, K. J. Sikes, J. Hone, H. L. Stormer, and P. Kim, *Phys. Rev. Lett.* **101**, 096802 (2008).
- [21] K. I. Bolotin, K. J. Sikes, Z. Jiang, M. Klima, G. Fudenberg, J. Hone, P. Kim, and H. L. Stormer, *Solid State Communications* **146**, 351 (2008).
- [22] E. V. Castro, H. Ochoa, M. I. Katsnelson, R. V. Gorbachev, D. C. Elias, K. S. Novoselov, A. K. Geim, and F. Guinea, *Phys. Rev. Lett.* **105**, 266601 (2010).
- [23] E. H. Hwang, S. Adam, and S. Das Sarma, *Phys. Rev. B* **76**, 195421 (2007).
- [24] F. Schedin, A. K. Geim, S. V. Morozov, E. W. Hill, P. Blake, M. I. Katsnelson, and K. S. Novoselov, *Nature Materials* **6**, 652 (2007).
- [25] C. R. Dean, A. F. Young, I. Meric, C. Lee, L. Wang, S. Sorgenfrei, K. Watanabe, T. Taniguchi, P. Kim, K. L. Shepard, and J. Hone, *Nature Nanotechnology* **5**, 722 (2010).
- [26] Y. Zhang, Z. Jiang, J. P. Small, M. S. Purewal, Y.-W. Tan, M. Fazlollahi, J. D. Chudow, J. A. Jaszczak, H. L. Stormer, and P. Kim, *Phys. Rev. Lett.* **96**, 136806 (2006).
- [27] A. S. Mayorov, R. V. Gorbachev, S. V. Morozov, L. Britnell, R. Jalil, L. A. Ponomarenko, P. Blake, K. S. Novoselov, K. Watanabe, T. Taniguchi, and A. K. Geim, *Nano Lett.* **11**, 2396 (2011).

- [28] W. Gannett, W. Regan, K. Watanabe, T. Taniguchi, M. F. Crommie, and A. Zettl, *Applied Physics Letters* **98**, 242105 (2011).
- [29] L. A. Ponomarenko, R. Yang, T. M. Mohiuddin, M. I. Katsnelson, K. S. Novoselov, S. V. Morozov, A. A. Zhukov, F. Schedin, E. W. Hill, and A. K. Geim, *Phys. Rev. Lett.* **102**, 206603 (2009).
- [30] J.-H. Chen, C. Jang, S. Adam, M. S. Fuhrer, E. D. Williams, and M. Ishigami, *Nat Phys* **4**, 377 (2008).
- [31] C. Jang, S. Adam, J.-H. Chen, E. D. Williams, S. Das Sarma, and M. S. Fuhrer, *Phys. Rev. Lett.* **101**, 146805 (2008).
- [32] A. K. M. Newaz, Y. S. Puzyrev, B. Wang, S. T. Pantelides, and K. I. Bolotin, *Nature Communications* **3**, 734 (2012).
- [33] M. Monteverde, C. Ojeda-Aristizabal, R. Weil, K. Bennaceur, M. Ferrier, S. Guéron, C. Glattli, H. Bouchiat, J. N. Fuchs, and D. L. Maslov, *Phys. Rev. Lett.* **104**, 126801 (2010).
- [34] Z. H. Ni, L. A. Ponomarenko, R. R. Nair, R. Yang, S. Anissimova, I. V. Grigorieva, F. Schedin, P. Blake, Z. X. Shen, E. H. Hill, K. S. Novoselov, and A. K. Geim, *Nano Lett.* **10**, 3868 (2010).
- [35] X. Hong, K. Zou, and J. Zhu, *Phys. Rev. B* **80**, 241415 (2009).
- [36] E. H. Hwang, S. Adam, and S. Das Sarma, *Phys. Rev. Lett.* **98**, 186806 (2007).
- [37] E. Rossi, S. Adam, and S. Das Sarma, *Phys. Rev. B* **79**, 245423 (2009).
- [38] S. Adam, E. H. Hwang, V. M. Galitski, and S. Das Sarma, *PNAS* **104**, 18392 (2007).
- [39] V. M. Galitski, S. Adam, and S. Das Sarma, *Phys. Rev. B* **76**, 245405 (2007).
- [40] Y. Zhang, V. W. Brar, C. Girit, A. Zettl, and M. F. Crommie, *Nat Phys* **5**, 722 (2009).
- [41] R. Decker, Y. Wang, V. W. Brar, W. Regan, H.-Z. Tsai, Q. Wu, W. Gannett, A. Zettl, and M. F. Crommie, *Nano Lett.* **11**, 2291 (2011).

- [42] J. Xue, J. Sanchez-Yamagishi, D. Bulmash, P. Jacquod, A. Deshpande, K. Watanabe, T. Taniguchi, P. Jarillo-Herrero, and B. J. LeRoy, *Nat Mater* **10**, 282 (2011).
- [43] A. Deshpande, W. Bao, F. Miao, C. N. Lau, and B. J. LeRoy, *Phys. Rev. B* **79**, 205411 (2009).
- [44] J. Martin, N. Akerman, G. Ulbricht, T. Lohmann, J. H. Smet, K. von Klitzing, and A. Yacoby, *Nature Physics* **4**, 144 (2007).
- [45] M. I. Katsnelson and A. K. Geim, *Phil. Trans. R. Soc. A* **366**, 195 (2008).
- [46] E.-A. Kim and A. H. Castro Neto, *EPL (Europhysics Letters)* **84**, 57007 (2008).
- [47] S. V. Morozov, K. S. Novoselov, M. I. Katsnelson, F. Schedin, L. A. Ponomarenko, D. Jiang, and A. K. Geim, *Phys. Rev. Lett.* **97**, 016801 (2006).
- [48] F. Guinea, M. I. Katsnelson, and A. K. Geim, *Nat Phys* **6**, 30 (2010).
- [49] V. M. Pereira and A. H. Castro Neto, *Phys. Rev. Lett.* **103**, 046801 (2009).
- [50] F. Guinea, B. Horovitz, and P. Le Doussal, *Phys. Rev. B* **77**, 205421 (2008).
- [51] N. Levy, S. A. Burke, K. L. Meaker, M. Panlasigui, A. Zettl, F. Guinea, A. H. C. Neto, and M. F. Crommie, *Science* **329**, 544 (2010).
- [52] D. C. Elias, R. R. Nair, T. M. G. Mohiuddin, S. V. Morozov, P. Blake, M. P. Halsall, A. C. Ferrari, D. W. Boukhvalov, M. I. Katsnelson, A. K. Geim, and K. S. Novoselov, *Science* **323**, 610 (2009).
- [53] E. Stolyarova, K. T. Rim, S. Ryu, J. Maultzsch, P. Kim, L. E. Brus, T. F. Heinz, M. S. Hybertsen, and G. W. Flynn, *PNAS* **104**, 9209 (2007).
- [54] M. Ishigami, J. H. Chen, W. G. Cullen, M. S. Fuhrer, and E. D. Williams, *Nano Lett.* **7**, 1643 (2007).
- [55] J. C. Meyer, A. K. Geim, M. I. Katsnelson, K. S. Novoselov, T. J. Booth, and S. Roth, *Nature* **446**, 60 (2007).
- [56] W. Bao, F. Miao, Z. Chen, H. Zhang, W. Jang, C. Dames, and C. N. Lau, *Nat Nano* **4**, 562 (2009).

- [57] R. C. Thompson-Flagg, M. J. B. Moura, and M. Marder, EPL **85**, 46002 (2009).
- [58] V. Geringer, M. Liebmann, T. Echtermeyer, S. Runte, M. Schmidt, R. Rückamp, M. C. Lemme, and M. Morgenstern, Phys. Rev. Lett. **102**, 076102 (2009).
- [59] C. H. Lui, L. Liu, K. F. Mak, G. W. Flynn, and T. F. Heinz, Nature **462**, 339 (2009).
- [60] A. Fasolino, J. H. Los, and M. I. Katsnelson, Nat Mater **6**, 858 (2007).
- [61] J. P. Robinson, H. Schomerus, L. Oroszlány, and V. I. Fal'ko, Phys. Rev. Lett. **101**, 196803 (2008).
- [62] K. Nomura and A. H. MacDonald, Phys. Rev. Lett. **96**, 256602 (2006).
- [63] T. Stauber, N. M. R. Peres, and F. Guinea, Phys. Rev. B **76**, 205423 (2007).
- [64] N. M. R. Peres, F. Guinea, and A. H. Castro Neto, Phys. Rev. B **73**, 125411 (2006).
- [65] J.-H. Chen, W. G. Cullen, C. Jang, M. S. Fuhrer, and E. D. Williams, Phys. Rev. Lett. **102**, 236805 (2009).
- [66] W. G. Cullen, M. Yamamoto, K. M. Burson, J. H. Chen, C. Jang, L. Li, M. S. Fuhrer, and E. D. Williams, Phys. Rev. Lett. **105**, 215504 (2010).
- [67] K. Burson, M. Yamamoto, and W. G. Cullen, Proceedings of the ASME 2011 International Design Engineering Technical Conferences & Computers and Information in Engineering Conference IDETC/CIE 2011. New York: ASME (2012).
- [68] K. M. Burson, M. Yamamoto, and W. G. Cullen, Beilstein Journal of Nanotechnology **3**, 230 (2012).
- [69] K. Burson, W. G. Cullen, C. Dean, S. Adam, K. Wantanabe, T. Taniguchi, P. Kim, and M. S. Fuhrer, In Preparation. (n.d.).
- [70] K. S. Novoselov, A. K. Geim, S. V. Morozov, D. Jiang, Y. Zhang, S. V. Dubonos, I. V. Grigorieva, and A. A. Firsov, Science **306**, 666 (2004).

- [71] C. Oshima and A. Nagashima, *J. Phys.: Condens. Matter* **9**, 1 (1997).
- [72] S. Bae, H. Kim, Y. Lee, X. Xu, J.-S. Park, Y. Zheng, J. Balakrishnan, T. Lei, H. Ri Kim, Y. I. Song, Y.-J. Kim, K. S. Kim, B. Özyilmaz, J.-H. Ahn, B. H. Hong, and S. Iijima, *Nat Nano* **5**, 574 (2010).
- [73] J. T. Robinson, S. W. Schmucker, C. B. Diaconescu, J. P. Long, J. C. Culbertson, T. Ohta, A. L. Friedman, and T. E. Beechem, *ACS Nano* **7**, 637 (2013).
- [74] M. Wang, S. K. Jang, W.-J. Jang, M. Kim, S.-Y. Park, S.-W. Kim, S.-J. Kahng, J.-Y. Choi, R. S. Ruoff, Y. J. Song, and S. Lee, *Advanced Materials* n/a (2013).
- [75] P. Blake, E. W. Hill, A. H. Castro Neto, K. S. Novoselov, D. Jiang, R. Yang, T. J. Booth, and A. K. Geim, *Applied Physics Letters* **91**, 063124 (2007).
- [76] Z. H. Ni, H. M. Wang, J. Kasim, H. M. Fan, T. Yu, Y. H. Wu, Y. P. Feng, and Z. X. Shen, *Nano Lett.* **7**, 2758 (2007).
- [77] A. C. Ferrari, J. C. Meyer, V. Scardaci, C. Casiraghi, M. Lazzeri, F. Mauri, S. Piscanec, D. Jiang, K. S. Novoselov, S. Roth, and A. K. Geim, *Phys. Rev. Lett.* **97**, 187401 (2006).
- [78] P. Fenter, F. Schreiber, L. Zhou, P. Eisenberger, and S. R. Forrest, *Phys. Rev. B* **56**, 3046 (1997).
- [79] S. M. Bayliss, S. Heutz, G. Rumbles, and T. S. Jones, *Physical Chemistry Chemical Physics* **1**, 3673 (1999).
- [80] G. Binnig, H. Rohrer, C. Gerber, and E. Weibel, *Phys. Rev. Lett.* **49**, 57 (1982).
- [81] H.-J. Güntherodt and R. Wiesendanger, *Scanning Tunneling Microscopy I: General Principles and Applications to Clean and Adsorbate-covered Surfaces* (Springer-Verlag, 1994).
- [82] (n.d.).
- [83] R. M. Feenstra, *Surface Science* **299–300**, 965 (1994).
- [84] J. Tersoff and D. R. Hamann, *Phys. Rev. Lett.* **50**, 1998 (1983).

- [85] G. Binnig, C. F. Quate, and C. Gerber, *Phys. Rev. Lett.* **56**, 930 (1986).
- [86] G. Binnig, U.S. Patent No. 4724318 (1986).
- [87] C. Leung, A. Bestembayeva, R. Thorogate, J. Stinson, A. Pyne, C. Marcovich, J. Yang, U. Drechsler, M. Despont, T. Jankowski, M. Tschöpe, and B. W. Hoogenboom, *Nano Lett.* **12**, 3846 (2012).
- [88] M. Grandbois, M. Beyer, M. Rief, H. Clausen-Schaumann, and H. E. Gaub, *Science* **283**, 1727 (1999).
- [89] Y. Sugimoto, P. Pou, M. Abe, P. Jelinek, R. Pérez, S. Morita, and Ó. Custance, *Nature* **446**, 64 (2007).
- [90] F. Mohn, J. Repp, L. Gross, G. Meyer, M. S. Dyer, and M. Persson, *Phys. Rev. Lett.* **105**, 266102 (2010).
- [91] L. Gross, F. Mohn, N. Moll, B. Schuler, A. Criado, E. Guitián, D. Peña, A. Gourdon, and G. Meyer, *Science* **337**, 1326 (2012).
- [92] L. Gross, F. Mohn, N. Moll, P. Liljeroth, and G. Meyer, *Science* **325**, 1110 (2009).
- [93] L. Gross, F. Mohn, N. Moll, G. Meyer, R. Ebel, W. M. Abdel-Mageed, and M. Jaspars, *Nat Chem* **2**, 821 (2010).
- [94] Una Bussola Per Le Reazioni Organiche (n.d.).
- [95] M. Nonnenmacher, M. P. O'Boyle, and H. K. Wickramasinghe, *Appl. Phys. Lett.* **58**, 2921 (1991).
- [96] S. Kitamura and M. Iwatsuki, *Applied Physics Letters* **72**, 3154 (1998).
- [97] S. Sadewasser and M. C. Lux-Steiner, *Phys. Rev. Lett.* **91**, 266101 (2003).
- [98] B. Luan and M. O. Robbins, *Phys. Rev. E* **74**, 026111 (2006).
- [99] B. Zappone, K. J. Rosenberg, and J. Israelachvili, *Tribology Letters* **26**, 191 (2007).
- [100] W. Raberg and K. Wandelt, *Appl Phys A* **66**, 1143 (1998).

- [101] W. Raberg, A. H. Ostadrahimi, T. Kayser, and K. Wandelt, *Journal of Non-Crystalline Solids* **351**, 1089 (2005).
- [102] F. J. Giessibl, *Rev. Mod. Phys.* **75**, 949 (2003).
- [103] M. A. Lantz, H. J. Hug, P. J. A. van Schendel, R. Hoffmann, S. Martin, A. Baratoff, A. Abdurixit, H.-J. Güntherodt, and C. Gerber, *Phys. Rev. Lett.* **84**, 2642 (2000).
- [104] T. Minobe, T. Uchihashi, T. Tsukamoto, Shigeki Orisaka, Y. Sugawara, and S. Morita, *Applied Surface Science* **140**, 298 (1999).
- [105] R. Pérez, I. Štich, M. C. Payne, and K. Terakura, *Phys. Rev. B* **58**, 10835 (1998).
- [106] H. Hölscher, W. Allers, U. D. Schwarz, A. Schwarz, and R. Wiesendanger, *Phys. Rev. B* **62**, 6967 (2000).
- [107] Z. H. Aitken and R. Huang, *Journal of Applied Physics* **107**, 123531 (2010).
- [108] J. N. Israelachvili, *Intermolecular and Surface Forces: Revised Third Edition* (Academic Press, 2011).
- [109] H. Hölscher, A. Schwarz, W. Allers, U. D. Schwarz, and R. Wiesendanger, *Phys. Rev. B* **61**, 12678 (2000).
- [110] M. A. Lantz, H. J. Hug, R. Hoffmann, P. J. A. van Schendel, P. Kappenberger, S. Martin, A. Baratoff, and H.-J. Güntherodt, *Science* **291**, 2580 (2001).
- [111] F. J. Giessibl, *Applied Physics Letters* **78**, 123 (2001).
- [112] Z. Sun, S. K. Hämäläinen, J. Sainio, J. Lahtinen, D. Vanmaekelbergh, and P. Liljeroth, *Phys. Rev. B* **83**, 081415 (2011).
- [113] D. R. Nelson and L. Peliti, *Journal de Physique* **48**, 1085 (1987).
- [114] T. Li and Z. Zhang, *J. Phys. D: Appl. Phys.* **43**, 075303 (2010).
- [115] O. Pierre-Louis, *Phys. Rev. E* **78**, 021603 (2008).

- [116] Veeco TESP-SS Uncoated Silicon cantilever, Veeco Probes, Inc. 3601 Calle Tecate, Suite C, Camarillo, CA 93012. (n.d.).
- [117] Olympus OMCL-AC160TS-W2 (n.d.).
- [118] Mikromasch Hi-Res-W (n.d.).
- [119] J. Y. Kim, H. K. Lee, and S. C. Kim, *Journal of Membrane Science* **163**, 159 (1999).
- [120] R. S. Ruoff, J. Tersoff, D. C. Lorents, S. Subramoney, and B. Chan, *Nature* **364**, 514 (1993).
- [121] T. Hertel, R. E. Walkup, and P. Avouris, *Phys. Rev. B* **58**, 13870 (1998).
- [122] J. S. Bunch, S. S. Verbridge, J. S. Alden, A. M. van der Zande, J. M. Parpia, H. G. Craighead, and P. L. McEuen, *Nano Lett.* **8**, 2458 (2008).
- [123] D. J. Henry, C. A. Lukey, E. Evans, and I. Yarovsky, *Molecular Simulation* **31**, 449 (2005).
- [124] D. H. Robertson, D. W. Brenner, and J. W. Mintmire, *Phys. Rev. B* **45**, 12592 (1992).
- [125] B. I. Yakobson, C. J. Brabec, and J. Bernholc, *Phys. Rev. Lett.* **76**, 2511 (1996).
- [126] A. Incze, A. Pasturel, and P. Peyla, *Phys. Rev. B* **70**, 212103 (2004).
- [127] G. Palasantzas and G. Backx, *Phys. Rev. B* **54**, 8213 (1996).
- [128] M. J. Yoo, T. A. Fulton, H. F. Hess, R. L. Willett, L. N. Dunkleberger, R. J. Chichester, L. N. Pfeiffer, and K. W. West, *Science* **276**, 579 (1997).
- [129] A. Yacoby, H. . Hess, T. . Fulton, L. . Pfeiffer, and K. . West, *Solid State Communications* **111**, 1 (1999).
- [130] Y.-J. Kang, J. Kang, and K. J. Chang, *Phys. Rev. B* **78**, 115404 (2008).
- [131] A. K. Geim and K. S. Novoselov, *Nat Mater* **6**, 183 (2007).

- [132] A. Sadeghi, A. Baratoff, S. A. Ghasemi, S. Goedecker, T. Glatzel, S. Kawai, and E. Meyer, *Phys. Rev. B* **86**, 075407 (2012).
- [133] Y. Rosenwaks, R. Shikler, T. Glatzel, and S. Sadewasser, *Phys. Rev. B* **70**, 085320 (2004).
- [134] S. Hudlet, M. Saint Jean, B. Roulet, J. Berger, and C. Guthmann, *Journal of Applied Physics* **77**, 3308 (1995).
- [135] R. Ludeke and E. Cartier, *Microelectronic Engineering* **59**, 259 (2001).
- [136] S. Adam, S. Jung, N. N. Klimov, N. B. Zhitenev, J. A. Stroscio, and M. D. Stiles, *Phys. Rev. B* **84**, 235421 (2011).
- [137] S. Das Sarma, S. Adam, E. H. Hwang, and E. Rossi, *Rev. Mod. Phys.* **83**, 407 (2011).
- [138] T. Ando, A. B. Fowler, and F. Stern, *Rev. Mod. Phys.* **54**, 437 (1982).
- [139] A. L. Efros, F. G. Pikus, and V. G. Burnett, *Phys. Rev. B* **47**, 2233 (1993).
- [140] K. Xu, P. Cao, and J. R. Heath, *Science* **329**, 1188 (2010).
- [141] O. Leenaerts, B. Partoens, and F. M. Peeters, *Phys. Rev. B* **77**, 125416 (2008).
- [142] J. Zhao, A. Buldum, J. Han, and J. P. Lu, *Nanotechnology* **13**, 195 (2002).
- [143] K. M. Burson, Y. Wei, W. G. Cullen, M. S. Fuhrer, and J. E. Reutt-Robey, *Nano Lett.* **12**, 2859 (2012).
- [144] G. Heimel, L. Romaner, E. Zojer, and J.-L. Bredas, *Acc. Chem. Res.* **41**, 721 (2008).
- [145] A. Natan, L. Kronik, H. Haick, and R. T. Tung, *Advanced Materials* **19**, 4103 (2007).
- [146] H. Ishii, K. Sugiyama, E. Ito, and K. Seki, *Advanced Materials* **11**, 605 (1999).
- [147] L. Kong, F. Chesneau, Z. Zhang, F. Staier, A. Terfort, P. A. Dowben, and M. Zharnikov, *J. Phys. Chem. C* **115**, 22422 (2011).

- [148] D. Cahen and A. Kahn, *Advanced Materials* **15**, 271 (2003).
- [149] B. A. Gregg, *J. Phys. Chem. B* **107**, 4688 (2003).
- [150] S. E. Gledhill, B. Scott, and B. A. Gregg, *Journal of Materials Research* **20**, 3167 (2005).
- [151] E. D. Wachsman and E. N. Armstrong, *ECS Trans.* **35**, 1955 (2011).
- [152] M. Backhaus-Ricoult, K. Adib, T. St. Clair, B. Luerssen, L. Gregoratti, A. Barinov, and P. Dudin, *Ceramic Engineering and Science Proceedings* **28**, 141 (2008).
- [153] Y. Wei and J. E. Reutt-Robey, *J. Am. Chem. Soc.* **133**, 15232 (2011).
- [154] Y. Wei, S. W. Robey, and J. E. Reutt-Robey, *The Journal of Physical Chemistry C* **112**, 18537 (2008).
- [155] E. I. Altman and R. J. Colton, *Phys. Rev. B* **48**, 18244 (1993).
- [156] H. I. Li, K. Pussi, K. J. Hanna, L.-L. Wang, D. D. Johnson, H.-P. Cheng, H. Shin, S. Curtarolo, W. Moritz, J. A. Smerdon, R. McGrath, and R. D. Diehl, *Phys. Rev. Lett.* **103**, 056101 (2009).
- [157] H.-N. Li, X.-X. Wang, S.-L. He, K. Ibrahim, H.-J. Qian, R. Su, J. Zhong, M. I. Abbas, and C.-H. Hong, *Surface Science* **586**, 65 (2005).
- [158] W. L. Yang, V. Brouet, X. J. Zhou, H. J. Choi, S. G. Louie, M. L. Cohen, S. A. Kellar, P. V. Bogdanov, A. Lanzara, A. Goldoni, F. Parmigiani, Z. Hussain, and Z.-X. Shen, *Science* **300**, 303 (2003).
- [159] G. J. Dutton, D. B. Dougherty, W. Jin, J. E. Reutt-Robey, and S. W. Robey, *Phys. Rev. B* **84**, 195435 (2011).
- [160] H. Fukagawa, S. Hosoumi, H. Yamane, S. Kera, and N. Ueno, *Phys. Rev. B* **83**, 085304 (2011).
- [161] H. Fukagawa, H. Yamane, S. Kera, K. K. Okudaira, and N. Ueno, *Phys. Rev. B* **73**, 041302 (2006).
- [162] Y. Wei, (2010).

- [163] C.-F. Lin, M. Zhang, S.-W. Liu, T.-L. Chiu, and J.-H. Lee, *IJMS* **12**, 476 (2011).
- [164] T. Tsuzuki, Y. Shirota, J. Rostalski, and D. Meissner, *Solar Energy Materials and Solar Cells* **61**, 1 (2000).
- [165] M. Brumbach, D. Placencia, and N. R. Armstrong, *The Journal of Physical Chemistry C* **112**, 3142 (2008).
- [166] D. Placencia, W. Wang, R. C. Shallcross, K. W. Nebesny, M. Brumbach, and N. R. Armstrong, *Advanced Functional Materials* **19**, 1913 (2009).
- [167] V. Palermo, M. Palma, and P. Samorì, *Adv. Mater.* **18**, 145 (2006).
- [168] R. Smoluchowski, *Physical Review* **60**, (1941).
- [169] K. Besocke, B. Krahl-Urban, and H. Wagner, *Surface Science* **68**, 39 (1977).
- [170] G. M. S. Jeong Young Park, *Physical Review Letters* **95**, 136802 (2005).
- [171] G. L. Beltramo, H. Ibach, U. Linke, and M. Giesen, *Electrochimica Acta* **53**, 6818 (2008).
- [172] L. Chen, R. Ludeke, X. Cui, A. G. Schrott, C. R. Kagan, and L. E. Brus, *J. Phys. Chem. B* **109**, 1834 (2005).
- [173] A. Liscio, V. Palermo, D. Gentilini, F. Nolde, K. Müllen, and P. Samorì, *Advanced Functional Materials* **16**, 1407 (2006).
- [174] T. Eguchi, Y. Fujikawa, K. Akiyama, T. An, M. Ono, T. Hashimoto, Y. Morikawa, K. Terakura, T. Sakurai, M. G. Lagally, and Y. Hasegawa, *Phys. Rev. Lett.* **93**, 266102 (2004).
- [175] O. G. Reid, G. E. Rayermann, D. C. Coffey, and D. S. Ginger, *J. Phys. Chem. C* **114**, 20672 (2010).
- [176] H. Hoppe, T. Glatzel, M. Niggemann, A. Hinsch, M. C. Lux-Steiner, and N. S. Sariciftci, *Nano Lett.* **5**, 269 (2005).
- [177] K. Maturová, M. Kemerink, M. M. Wienk, D. S. H. Charrier, and R. A. J. Janssen, *Advanced Functional Materials* **19**, 1379 (2009).

- [178] M. Schnippering, M. Carrara, A. Foelske, R. Kötz, and D. J. Fermín, *Phys. Chem. Chem. Phys.* **9**, 725 (2007).
- [179] D. S. H. Charrier, M. Kemerink, B. E. Smalbrugge, T. de Vries, and R. A. J. Janssen, *ACS Nano* **2**, 622 (2008).
- [180] Y. Hasegawa and P. Avouris, *Phys. Rev. Lett.* **71**, 1071 (1993).
- [181] A. Hamelin, L. Stoicoviciu, L. Doubova, and S. Trasatti, *Surface Science* **201**, L498 (1988).
- [182] G. L. Beltramo, H. Ibach, and M. Giesen, *Surface Science* **601**, 1876 (2007).
- [183] O. Jeandupeux, L. Bürgi, A. Hirstein, H. Brune, and K. Kern, *Phys. Rev. B* **59**, 15926 (1999).
- [184] S. D. Kevan and R. H. Gaylord, *Phys. Rev. B* **36**, 5809 (1987).
- [185] T. Sakurai, X. D. Wang, T. Hashizume, V. Yurov, H. Shinohara, and H. W. Pickering, *Applied Surface Science* **87–88**, 405 (1995).
- [186] W. Chauvenet, *A Manual of Spherical and Practical Astronomy*, 5th ed. (Dover, Dover, N.Y., 1863).
- [187] J. R. Taylor, *An Introduction to Error Analysis: The Study of Uncertainties in Physical Measurements*, 2nd ed. (University Science Books, 1996).
- [188] K. Giesen, F. Hage, F. J. Himpsel, H. J. Riess, and W. Steinmann, *Phys. Rev. Lett.* **55**, 300 (1985).
- [189] M. Chelvayohan and C. H. B. Mee, *J. Phys. C: Solid State Phys.* **15**, 2305 (1982).
- [190] M. Linares, D. Beljonne, J. Cornil, K. Lancaster, J.-L. Brédas, S. Verlaak, A. Mityashin, P. Heremans, A. Fuchs, C. Lennartz, J. Idé, R. Méreau, P. Aurel, L. Ducasse, and F. Castet, *J. Phys. Chem. C* **114**, 3215 (2010).
- [191] L.-L. Wang and H.-P. Cheng, *Phys. Rev. B* **69**, 165417 (2004).
- [192] N. Hayashi, H. Ishii, Y. Ouchi, and K. Seki, *J. Appl. Phys.* **92**, 3784 (2002).

- [193] U. Zerweck, C. Loppacher, T. Otto, S. Grafström, and L. M. Eng, *Nanotechnology* **18**, 084006 (2007).
- [194] A. Tada, Y. Geng, Q. Wei, K. Hashimoto, and K. Tajima, *Nat Mater* **10**, 450 (2011).
- [195] M. Groce, *Organic Molecular Thin Films on Device-Relevant Substrates*, University of Maryland, 2013.
- [196] Y. Zhang, T.-T. Tang, C. Girit, Z. Hao, M. C. Martin, A. Zettl, M. F. Crommie, Y. R. Shen, and F. Wang, *Nature* **459**, 820 (2009).
- [197] G. Cocco, E. Cadelano, and L. Colombo, *Phys. Rev. B* **81**, 241412 (2010).